

Clemson University

**TigerPrints**

---

All Dissertations

Dissertations

---

5-2019

## Evaporator Modeling and an Optimal Control Strategy Development of an Organic Rankine Cycle Waste Heat Recovery System for a Heavy Duty Diesel Engine Application

Dhruvang Rathod

*Clemson University*, [dhruvang.r26@gmail.com](mailto:dhruvang.r26@gmail.com)

Follow this and additional works at: [https://tigerprints.clemson.edu/all\\_dissertations](https://tigerprints.clemson.edu/all_dissertations)



Part of the [Automotive Engineering Commons](#)

---

### Recommended Citation

Rathod, Dhruvang, "Evaporator Modeling and an Optimal Control Strategy Development of an Organic Rankine Cycle Waste Heat Recovery System for a Heavy Duty Diesel Engine Application" (2019). *All Dissertations*. 2704.

[https://tigerprints.clemson.edu/all\\_dissertations/2704](https://tigerprints.clemson.edu/all_dissertations/2704)

This Dissertation is brought to you for free and open access by the Dissertations at TigerPrints. It has been accepted for inclusion in All Dissertations by an authorized administrator of TigerPrints. For more information, please contact [kokeefe@clemson.edu](mailto:kokeefe@clemson.edu).

**EVAPORATOR MODELING AND AN OPTIMAL CONTROL STRATEGY  
DEVELOPMENT OF AN ORGANIC RANKINE CYCLE WASTE  
HEAT RECOVERY SYSTEM FOR A HEAVY DUTY  
DIESEL ENGINE APPLICATION**

---

A Dissertation  
Presented to  
the Graduate School of  
Clemson University

---

In Partial Fulfillment  
of the Requirements for the Degree  
Doctor of Philosophy  
Automotive Engineering

---

by  
Dhruvang Rathod  
May 2019

---

Accepted by:  
Dr. Zoran Filipi, Committee Chair  
Dr. Mark Hoffman  
Dr. Ardalan Vahidi  
Dr. Robert Prucka

## **ABSTRACT**

The Organic Rankine Cycle (ORC) has proven to be a promising technology for Waste Heat Recovery (WHR) systems in heavy duty diesel engine applications. However, due to the highly transient heat source, controlling the working fluid flow through the ORC system and maximizing the heat recovery is a challenge for real time application. To that end, this research resulted in the following main developments.

The first new development is in the area of heat exchanger modeling. The heat exchanger is a key component within the WHR system and it governs the dynamics of the complete ORC system. The heat exchanger model is extended using a thermal image data to improve its phase length prediction capability. It's shown that the new identified empirical equations help improve the phase length estimation by 43% over a set of transient experiments. As a result, the model can be used to develop an improved control oriented moving boundary model and to provide insights into evaporator design.

The second new development is the advancement of the control design of an ORC system. With advanced knowledge of the heat source dynamics, there is potential to enhance power optimization from the WHR system through predictive optimal control. The proposed approach in this this dissertation is a look-ahead control strategy where, the future vehicle speed is predicted utilizing road topography and V2V connectivity. The forecasted vehicle speed is utilized to predict the engine speed and torque, which facilitates estimation of the engine exhaust conditions used in the ORC control model. In the simulation study, a reference tracking controller is designed based on the Model Predictive Control (MPC) methodology. Two variants of Non-linear MPC (NMPC) are evaluated: an

NMPC with look-ahead exhaust conditions and a baseline NMPC without the knowledge of future exhaust conditions. Simulation results show no particular improvement to working fluid superheat tracking at the evaporator outlet via the look-ahead strategy for a drive cycle. However, the look-ahead control strategy does provide a substantial reduction in system control effort via dampening the heavily transient working fluid pump actuation, enhancing pump longevity, health, and reducing pump power consumption. This reduction in pump actuation helps the NMPC with preview to maintain the superheat lower than the NMPC without this feature for certain frequency of the exhaust conditions. Overall, NMPC with preview feature can help reduce parasitic losses, like pump power and improve power generation.

The third development addresses the modeling errors and measurement inaccuracies for NMPC implementation. NMPC is inherently a state feedback system and for that reason an Extended Kalman Filter (EKF) is used to estimate unmeasurable states inside the ORC evaporators based on exhaust gas and working fluid temperatures. Since it is not realistic to expect that the system model will perfectly describe the behavior of the evaporator dynamics in all operating conditions, the estimator is therefore augmented with a disturbance model for offset free MPC tracking. Simulation study shows that the augmented system is perfectly capable of discarding the model errors and rejecting the measurement inaccuracies. Moreover, experimental validation confirms that no steady state error is observed during online implementation of the augmented EKF.

Finally, experimental validation of the designed NMPC control strategy was conducted. The performance of the NMPC was evaluated on a heavily transient drive cycle,



as well as on a sinusoidal generated heat signals. Both experimental and simulated sinusoidal exhaust condition shows that evaporator under consideration inherently helps attenuate the fluctuating exhaust conditions due to its thermal inertia especially for heat signals of shorter time periods. However for slow changing exhaust conditions, a slower rate of change of working fluid flow helps in inhibiting temperature overshoot at the evaporator outlet.

## ACKNOWLEDGEMENT

This dissertation is a result of a team effort. First and for most, I would like to thank Dr. Mark Hoffman for welcoming me to Clemson University and giving me this opportunity to pursue my research goal. I am highly grateful towards the invaluable discussions we had exploring the unknowns and the exceptional mentorship I received during my time at ICAR. Those were some **good times!**

I am also highly thankful to my advisor Dr. Zoran Filipi for his willingness and extraordinary abilities to explain any engineering issues. His unparalleled experience and expertise were a great help in bringing this thesis to completion. I would also like to thank Dr. Ardalan Vahidi for explaining all the controls concepts both in class and its application in my thesis. I was very pleased towards his receptiveness for any questions and issues I faced during controls implementation.

I am grateful to my colleague Dr. Bin Xu for the many inspiring discussions and collaboration during last four years. I would also like to appreciate the efforts and technical support put forward by Jeremy Barnes in helping me and other students in the test lab.

I would like to acknowledge Paul Anshel, Xiaobin (Shawn) Liu from BorgWarner Inc. for their technical support and financial assistance during this project.

Lastly, I would like to express my immense gratitude towards my family (my father- Bipinchandra Rathod, my mother- Nirmala Rathod and my brother- Jayendra Rathod) for all their love and encouragement during these four years. They are the backbone of my professional and educational growth. Without their support I wouldn't be standing where I am today. I cordially thank them for inspiring me every day in all aspects of life!

# TABLE OF CONTENTS

TITLE.....	i
ABSTRACT.....	ii
ACKNOWLEDGEMENT .....	v
TABLE OF CONTENTS.....	vi
LIST OF TABLES .....	ix
LIST OF FIGURES .....	x
NOMENCLATURE .....	xv
CHAPTER 1. INTRODUCTION .....	1
1.1 Organic Rankine cycle .....	2
1.2 Open Loop Experimental analysis.....	5
1.2.1 Step Change in Uncontrollable Input – Engine Conditions.....	6
1.2.2 Step Change in Controllable Input – Working Fluid Pump speed .....	8
1.3 Problem statement .....	10
1.3 Objectives.....	12
1.4 Dissertation Outline.....	12
CHAPTER 2. EVAPORATOR MODELING .....	14
2.1 Introduction .....	14
2.2 Background .....	14
2.2.1 Heat Exchanger Modeling.....	14
2.2.2 Importance of Phase length estimation.....	15
2.2.3 Sensitivity of ORC-WHR Energy Recovery to Working Fluid Phase Length.....	16
2.3 System Configuration.....	18
2.4 Thermal Image Processing .....	20

2.4.1 Still Image Processing .....	20
2.4.2 Video Processing .....	21
2.4.3 Phase Change Detection .....	25
2.5 Evaporator Modeling.....	26
2.5.1 Heat Transfer Coefficients .....	29
2.6 Sensitivity Analysis: FVM Discretization.....	31
2.7 Enhancing FVM Phase Prediction Accuracy .....	34
2.7.1 Manual Parameter Tuning .....	35
2.7.2 Particle Swarm Optimization Parameter Identification.....	41
2.8 Results .....	46
2.8.1 Transient Test Sequence #1 .....	46
2.8.2 Transient Test Sequence #2.....	52
2.9 Conclusions .....	54
 CHAPTER 3. DYNAMIC CHARACTERIZATION OF EVAPORATOR.....	 56
3.1 Introduction .....	56
3.2 Background .....	56
3.3 Evaporator Thermal Inertia .....	57
3.4 Working fluid properties .....	61
3.5 ORC System dynamics evaluation .....	62
3.5.1 Uncontrollable Inputs: Exhaust Conditions.....	64
3.5.2 Controllable Inputs: Working fluid mass flow .....	66
3.6 Conclusion.....	68
 CHAPTER 4. CONTROL DESIGN.....	 69
4.1 Introduction .....	69
4.2 Background .....	69
4.2.1 Look-ahead ORC control .....	70
4.2.2 Opportunity and Uniqueness of the current work.....	71
4.3 Moving Boundary Control Model.....	72
4.4 NMPC Problem Formulation .....	76
4.5.1 ACADO Implementation.....	77
4.6 Disturbance Model and Observer Design.....	78

4.7 Simulation Results.....	79
4.7.1 NMPC Cost function formulation .....	80
4.7.2 Disturbance Rejection .....	84
4.7.3 Look-ahead NMPC.....	88
4.8 Conclusions .....	100
CHAPTER 5. NMPC EXPERIMENTAL VALIDATION .....	102
5.1 Introduction .....	102
5.2 Background .....	102
5.3 Experimental Set-up .....	104
5.4 Online Model Calibration.....	105
5.4.1 EKF state estimation error.....	107
5.5 Ramp-up and Ramp-down Events.....	110
5.6 Drive cycle .....	112
5.7 Sinusoidal Inputs .....	114
5.7.1 Time period of 20 s.....	115
5.7.2 Time period of 60 s.....	116
5.7.3 Time period of 120 s.....	118
5.8 Conclusions .....	120
Chapter 6. Conclusion, Contributions and Future Work .....	122
6.1 Conclusions and Contributions.....	122
6.2 Future Work .....	125
APPENDIX.....	127
REFERENCES .....	128
PUBLICATIONS.....	136

## LIST OF TABLES

Table 2. 1. Steady state experimental conditions for evaluating FVM discretization. ....	31
Table 2. 2. Error summary for different levels of discretization of the FVM model.....	33
Table 2. 3. Analysis the effects of additional multipliers on phase lengths for test conditions in Table 1. [Negative error means under-estimation and positive error is over-estimation] .....	36
Table 2. 4. Summary of Sensitivity analysis of different PSO targets. Negative error in the above Table indicates under-estimation whereas positive error corresponds to over-estimation. ....	43
Table 2. 5. PSO identified variables for Case #5 in Table 2.4.....	44
Table 2. 6. Comparison of the phase length estimation between baseline FVM model and calibrated FVM model. ....	49
Table 3. 1. Summary of the control objective of the ORC-WHR system. ....	64
Table 3. 2. Exhaust conditions for sensitivity analysis on the uncontrollable inputs .....	64
Table 4. 1. Quantified NMPC temperature error comparison with and without preview capability for the drive cycle in Figure 4.9. ....	92
Table 4. 2. NMPC temperature error for different preview times of Figure 4.10. ....	94
Table 4. 3. NMPC temperature error comparison for different time periods of the sinusoidal input of Figure 4.11.....	97
Table 4. 4. Percentage reduction in control input amplitude for the look-ahead NMPC ('with preview') for different time periods of the sinusoidal input in Figure 4.11.....	98
Table 5. 1. NMPC superheat tracking error for different time period sinusoidal heat signal. .....	120

## LIST OF FIGURES

Figure 1. 1. Performance indicators of each waste heat recovery technology for an automotive application (5 being the best) [8] .....	2
Figure 1. 2. Schematic of ORC-WHR system coupled with Engine. (x – Vapor fraction) 3	
Figure 1. 3. T-S diagram for Rankine cycle.....	4
Figure 1. 4. (a) Engine condition for a step change in torque and (b) Exhaust condition and working fluid temperature response at the evaporator outlet for a step change in engine torque .....	7
Figure 1. 5. Working fluid evaporator outlet temperature response to the step-change in pump-actuator position. ....	9
Figure 2. 1. Vapor phase length control diagram.....	16
Figure 2. 2. Organic Rankine cycle waste heat recovery system power comparison between two working fluid boundary layer estimation accuracies: (a) vapor phase length over the total boiler length as a percentage, and (b) normalized turbine power and normalized cumulative energy. In the legends, 7% model error means the results from a simulation subject to a vapor phase length estimation error of 7% prior to the feedback control. In contrast, 2% model error means the results from a simulation with a 2% vapor phase length estimation error prior to the feedback control.....	18
Figure 2. 3. Evaporator design schematic. ....	19
Figure 2. 4. An example of the Thermal Image from FLIR A300 camera utilizing an 18mm lens displaying the line chosen for detailed temperature analysis from the thermal images. In consideration of the sponsor’s intellectual property rights, some features of the evaporator have been intentionally blurred.....	19
Figure 2. 5. Comparison of RGB intensities on each point on the temperature detection line.....	22
Figure 2. 6. Temperature comparison data between FLIR tools and Matlab code operating on the same still thermal image. ....	24

Figure 2. 7. Extracted temperatures along the top surface of the evaporator (along the defined line of interest shown in Figure 2.4) with respect to normalized working fluid tube length in the evaporator. Also shown are the three regions of interest (A-C), corresponding to the different working fluid phases. ....	24
Figure 2. 8. Schematic representation of Finite Volume Method used for evaporator modeling. ....	28
Figure 2. 9. Working Fluid temperature across the length of evaporator tube for different FVM discretization. ....	32
Figure 2. 10. Comparison of simulated working fluid temperature from FVM model 500 cells discretization and corresponding thermal image. ....	33
Figure 2. 11. Effects of varying $U_{vap}$ values on phase lengths and outlet temperature.....	37
Figure 2. 12. Effects of varying $U_{liq}$ values on phase lengths and outlet temperature.....	38
Figure 2. 13. Effects of varying $U_{mix,1}$ and $U_{mix,2}$ values on phase lengths and outlet temperature. ....	39
Figure 2. 14. Effects of varying $U_{mix,1}$ and $U_{mix,2}$ values on heat transfer coefficient. ....	40
Figure 2. 15. Comparison of working fluid heat transfer coefficient from the FVM baseline model and the FVM with PSO identified values. ....	44
Figure 2. 16. Comparison of working fluid temperature along the length of the evaporator from the FVM baseline model and the FVM with PSO identified values.....	46
Figure 2. 17. Exhaust and Working Fluid conditions for Test 1.....	47
Figure 2. 18. Baseline FVM simulation results for the evaporator outlet temperatures for Test 1.....	48
Figure 2. 19. Phase length comparison between the baseline FVM model and experimental thermal video for Test sequence #1. ....	48
Figure 2. 20. Phase length comparison between the enhanced FVM and the experimental thermal video for Test #1.....	50
Figure 2. 21. Phase length error comparison for the baseline and enhanced FVMs relative to the thermal imaging results during transient Test 1.....	51



Figure 2. 22. Simulated working fluid and exhaust gas outlet temperature results from the enhanced FVM plotted relative to the experimental values for transient Test #1. ....	52
Figure 2. 23. Exhaust and Working Fluid conditions for Test 2.....	53
Figure 2. 24. Phase lengths comparison between the enhanced FVM model and the thermal videos for Transient Test #2. ....	53
Figure 2. 25. Simulated working fluid and exhaust outlet temperatures using the enhanced FVM plotted relative to the experimental values during transient Test #2.....	54
Figure 3. 1. Typical TP and EGR exhaust conditions.....	57
Figure 3. 2. Evaporator size comparison .....	58
Figure 3. 3. Thermal response of TP and EGR evaporators to sinusoidal exhaust conditions with varying time period, T .....	59
Figure 3. 4. Summary of thermal response of TP and EGR evaporator. ....	60
Figure 3. 5. (a) ORC system pressure as a linear function of Working fluid mass flow (b) Saturation temperature vs system pressure correlation for ethanol as working fluid .....	61
Figure 3. 6. Open loop plant model with inputs, outputs and control objective. ....	63
Figure 3. 7. Open loop simulation to characterize ORC system time constant for step changes in exhaust mass flow and temperature. ....	65
Figure 3. 8. Open loop simulation to characterize ORC system time constant for step changes in working fluid flow. ....	67
Figure 4. 1. Schematic representation of Moving Boundary Model used for evaporator control-oriented modeling (counter flow).....	73
Figure 4. 2. Generated sinusoidal exhaust mass flow with varying time periods to test the NMPC controller.....	80
Figure 4. 3. Power maximization MPC performance for the exhaust condition shown in Figure 4.2. Plot (a) shows the response of the working fluid temperature at the evaporator outlet to different sinusoidal inputs with the superheat plot shown in the bottom graph. Plot	

(b) shows the controller generated control input and corresponding response of the saturation pressure. ....	82
Figure 4. 4. Plot (a) Superheat tracking MPC performance for the exhaust condition shown in Figure 4.2. Plot (b) shows the controller generated control input and corresponding response of the saturation pressure. ....	84
Figure 4. 5. Step sequence of the exhaust test conditions for plant and control model mismatch comparison .....	85
Figure 4. 6. NMPC performance comparison with and without the augmented disturbance model during a period of mismatch between the plant and control models. ....	86
Figure 4. 7. Disturbance augmented NMPC performance comparison for various constant temperature offsets between plant and control model. ....	88
Figure 4. 8. Proposed control law for the ORC-WHR system.....	89
Figure 4. 9. HDDE Drive Cycle exhaust test conditions for NMPC analysis .....	90
Figure 4. 10. Look-ahead NMPC performance ('with preview') compared to the baseline NMPC ('without preview') during a drive cycle.....	91
Figure 4. 11. Look-ahead NMPC performance comparison with different preview window sizes (total preview time). ....	93
Figure 4. 12. Sinusoidal exhaust test conditions for comparison of the look ahead and baseline NMPC. ....	95
Figure 4. 13. Performance comparison for the look-ahead NMPC ('with preveiw') and the baseline NMPC ('without preview') while subjected to the sinusoidal heat source. $H_p=60$ s. SH Reference = $20^{\circ}\text{C}$ .....	96
Figure 4. 14. Performance comparison for the look-ahead NMPC ('with preveiw') and the baseline NMPC ('without preview') while subjected to the sinusoidal heat source. $H_p=60$ s. SH Reference = $20^{\circ}\text{C}$ .....	99
Figure 5. 1. Experimental set-up showing the Engine, after-treatment system and the ORC rig in a transient capable heavy duty engine dynamometer at Clemson University's Automotive research facility.....	104
Figure 5. 2. (a) AVL's PUMA and INCA data collection interface (b) DSPACE MicroAutoBox for implementing the NMPC algorithm.....	105

Figure 5. 3. System aging characterization for the same engine conditions with data set 1 being the green ORC system and data set 2 representing the aged ORC system. ....	106
Figure 5. 4. Online tuning of heat transfer coefficients for MBM of TP evaporator resulted in stable state estimation by the EKF .....	108
Figure 5. 5. Proposed control law (Figure 4.8) incorporated with system aging adaptation variable, $\varepsilon(t)$ .....	109
Figure 5. 6. Tuned NMPC performance for a 30s ramp in engine conditions.....	110
Figure 5. 7. Tuned NMPC performance for a ramp input of rise time 5 sec .....	111
Figure 5. 8. (a) Engine conditions for the constant speed drive cycle (b) Tuned NMPC superheat tracking performance and generated working fluid flow rate .....	113
Figure 5. 9. NMPC Computation time for the constant speed drive cycle .....	114
Figure 5. 10. (a) Engine conditions for the sinusoidal cycle with time period of 20s (b) Tuned NMPC superheat tracking performance and generated working fluid flow rate, $Wdu=10$ .....	116
Figure 5. 11. (a) Engine conditions for the sinusoidal cycle with time period of 60s (b) Tuned NMPC superheat tracking performance and generated working fluid flow rate, $Wdu=10$ .....	117
Figure 5. 12. (a) Engine conditions for the sinusoidal cycle with time period of 120s (b) Tuned NMPC superheat tracking performance comparison with weights, $Wdu=10$ and $Wdu=60$ with generated working fluid flow rate .....	119

## NOMENCLATURE

$a$	transverse pitch ratio
$A$	area [m <sup>2</sup> ]
$b$	longitudinal pitch ratio
$B$	Blue
$c_p$	heat capacity [J/kg·K]
$C$	constant of two-phase multiplier correlation
$d$	diameter [m]
$f$	friction factor
$F$	force [N]
$G$	Green
$h$	enthalpy [J/kg]
$H$	height [m]
$\dot{H}$	enthalpy flowrate [J/s]
$k$	Thermal conductivity
$l, L$	length [m]
$m$	mass [kg]
$\dot{m}$	mass flow rate [kg/s]
$p$	pressure [Pa]
$t$	time [s]
$T$	temperature [K]
$u$	velocity [m/s], internal energy [J/kg]
$U$	heat transfer coefficient [J/kg·K]
$v_f$	flow velocity [m/s]
$\nu_k$	kinematic viscosity [m <sup>2</sup> /s]
$v$	volume [m <sup>3</sup> ]
$x$	vapor quality
$z$	space coordinate [m]
$\psi$	void fraction
$R$	Red
$Re$	Reynolds number
$Pr$	Prandtl number
$Nu$	Nusselt number
$\gamma$	specific heat ratio
$\rho$	density [kg/m <sup>3</sup> ]
$\partial$	partial derivative operator
$\xi$	friction factor

### ***Abbreviations***

ORC	organic Rankine cycle
DOE	Department of Energy (USA)

WHR waste heat recovery  
 HDD heavy duty diesel  
 MBM moving boundary method  
 FVM finite volume method  
 TP tail pipe  
 EGR exhaust gas recirculation  
 HTC heat transfer coefficient  
 FLIR Forward looking Infrared

***Subscripts and superscripts***

*f* working fluid  
*w* wall  
*e* exhaust gas  
*v* vapor  
*l* liquid  
*i*  $i^{\text{th}}$  discretized cell  
*in* inlet/ upstream  
*out* outlet  
 $\eta$  efficiency  
*M,m* mix point  
*V* vapor point  
*p* pressure  
*fr* friction  
*g* gravitation  
*vap* saturated vapor  
*sat* saturated liquid  
*tp* two phase  
*s* single phase  
*U* heat transfer coefficient  
*sim* simulation  
*exp* experimental  
*TP* tail pipe  
*EGR* exhaust gas recirculation  
*cross* cross or sectional surface

## **CHAPTER 1. INTRODUCTION**

The trucking industry is the lifeblood of the US (United States) economy. In a survey conducted by University of Michigan and in cooperation by ATRI (American Transportation Research Institute), with a total of 31 million commercial registered trucks, the total fuel consumed in 2015 was 54 billion gallons [1]. Heavy duty trucks which are powered by diesel fuel, accounted for 75% of this fuel consumption and represents the 2<sup>nd</sup> highest expense of total operating costs. The other side-effect of fuel consumption is the diesel exhaust emissions which are detrimental to both environment and human health. With the growing economy and consumer demand these numbers are projected to increase every year. Therefore, in response to a Presidential Memorandum, EPA in coordination with NHTSA issued greenhouse gas emissions and fuel economy standards for heavy duty trucks [2]. The ultimate goal of this proposed policy was to demonstrate 55% or greater brake thermal efficiency engine in the SuperTruck II program funded by Department of Energy (DOE).

Since the United States DOE super truck program commenced in 2010, companies and research institutions have continually explored a wide array of cutting-edge technologies to improve HDD (Heavy Duty Diesel) engine efficiency. Waste heat recovery (WHR) has proven to be a crucial technique in improving the fuel economy [3-4]. Since exhaust heat energy comprises nearly 45% of the total fuel energy [7], WHR techniques have become top contenders for reducing fuel consumption and CO<sub>2</sub> emissions. Some research studies produced fuel economy improvements of 4-8% when utilizing exhaust energy recovery [5-6]. One proven WHR technique is the utilization of an Organic Rankine Cycle (ORC).

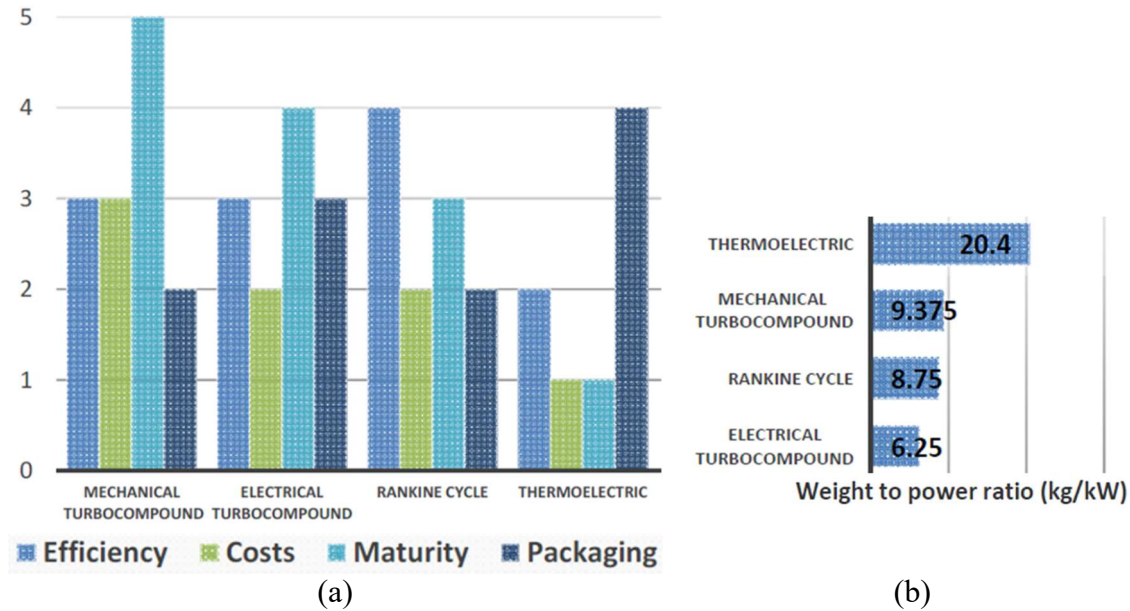


Figure 1.1. Performance indicators of each waste heat recovery technology for an automotive application (5 being the best) [8]

Figure 1.1 shows that turbo-compounding and Rankine cycle are most profitable WHR systems to be most likely feasible in an automotive application. Although the weight to power ratio of turbo-compounding system is favorable, the higher back pressure reduces the overall engine + WHR system efficiency. Utilizing one or more heat sources for Rankine cycle [5, 9-10] will help improve weight to power ratio. Other research works also demonstrates high thermal efficiency of Rankine cycle in comparison with other waste heat recovery techniques [11-12]. These results are encouraging and provide impetus towards increasing research efforts in investigating feasible control strategies towards ORC implementation.

### 1.1 Organic Rankine cycle

ORC operation is similar to the stationary Rankine cycles used in power plants, except that the working fluid in ORC is an organic fluid rather than water. Organic working fluids typically have low boiling points, making them suitable for low-grade (a low temperature source) waste heat recovery. ORC-WHR is adaptable to the multiple heat sources available from engines, namely: the

tailpipe (TP) exhaust gas, the exhaust gas recirculation (EGR) circuit, the charge air cooler (CAC) and the engine coolant [9-10, 16].

The main components of a typical ORC system are an evaporator, condenser, pump, expansion tank and an expander. Figure 1.2 shows an ORC-WHR example implemented on a HDD engine using TP gas as heat source.

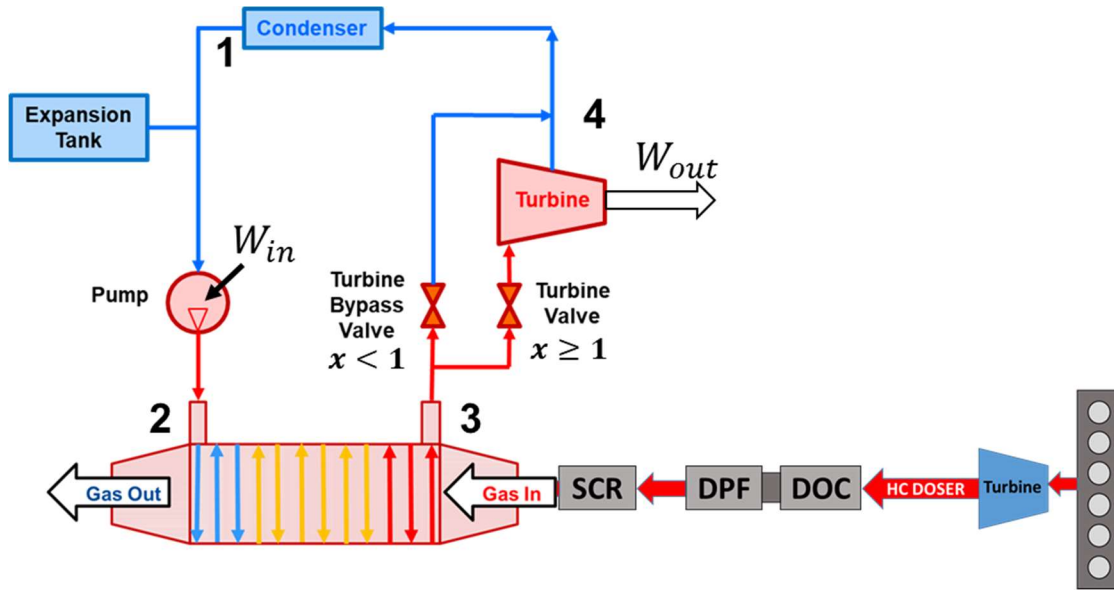


Figure 1. 2. Schematic of ORC-WHR system coupled with Engine. ( $x$  – Vapor fraction)

As shown in Figure 1.2, the high pressure pump continuously circulates working fluid through the WHR circuit. The process 1-2 represents the work consumed by the pump,  $W_{in}$ . The working fluid undergoes a phase change inside the evaporator (process 2-3) and exits in vapor phase (at point 3) after extracting heat from the exhaust gases. The high pressure working fluid vapor then expands inside the turbine (process 3-4), where the heat energy is converted to electrical energy to be utilized as needed,  $W_{out}$ . Finally, the working fluid flows from the turbine to a condenser where it changes back to liquid phase (process 4-1). This cycle is then repeated for continuous operation. Utilization of a turbine bypass valve ensures safe turbine operation by re-directing liquid working



fluid straight to the condenser. From T-S diagram of the process 1-4 as described above, it can be concluded that work input into the cycle,  $W_{in}$  is always less than work output,  $W_{out}$  generating a positive net work across the cycle, an important characteristic of Rankine cycle.

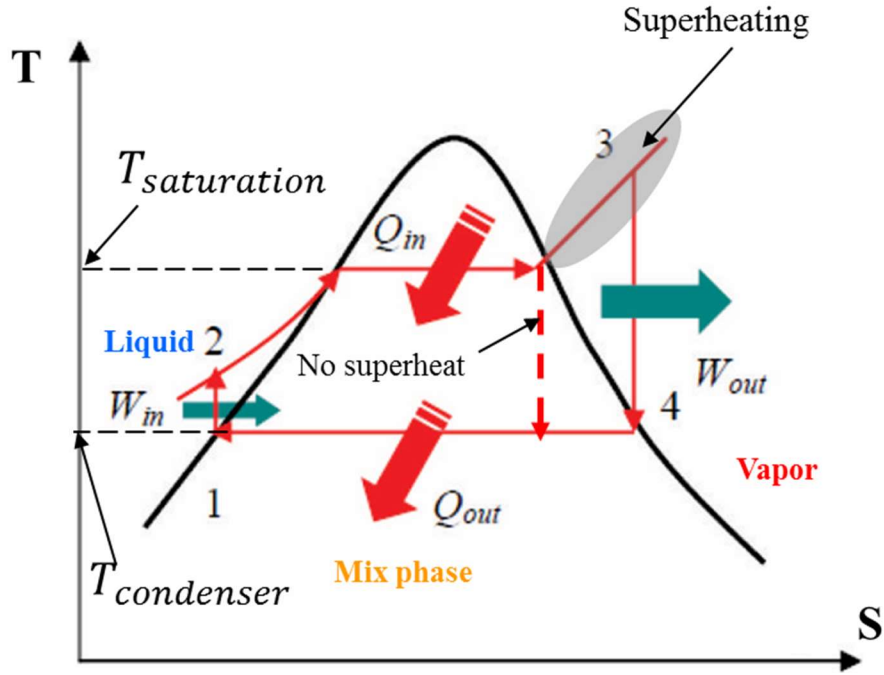


Figure 1. 3. T-S diagram for Rankine cycle

There are some conditions and requirements associated with the operation of the ORC system as stated. 1) Superheating is required for safe turbine operation and thus dictates minimum temperature requirement for the cycle. 2) The working fluid in a Rankine cycle follows a closed loop and is reused constantly, so it's important to maintain its integrity and thermal capacity for as long as possible. 3) It should be noted that the working fluid deteriorates at high temperature and therefore dictates maximum temperature limit for the ORC.

ORC systems have been explored as early as 1970's mostly for the small scale applications with overall system efficiency less than 10% [13-15]. Since then ORC systems have been applied to multiple stationary applications such as biomass heat and power recovery, geo-thermal heat recovery, solar-energy collector and waste heat recovery from industrial processes. While the

Rankine cycle has a long history in stationary applications, its implementation in the automotive field has additional barriers to adaptation. The transient nature of heat sources, tight packaging constraints, system weight, safety and environmental issues, limited (and varying) cooling capacity, and the cost-conscious nature of the HDD industry has created challenges for ORC-WHR implementation. Advanced control design is a technology enabler for efficient and safe ORC system operation in an automotive application.

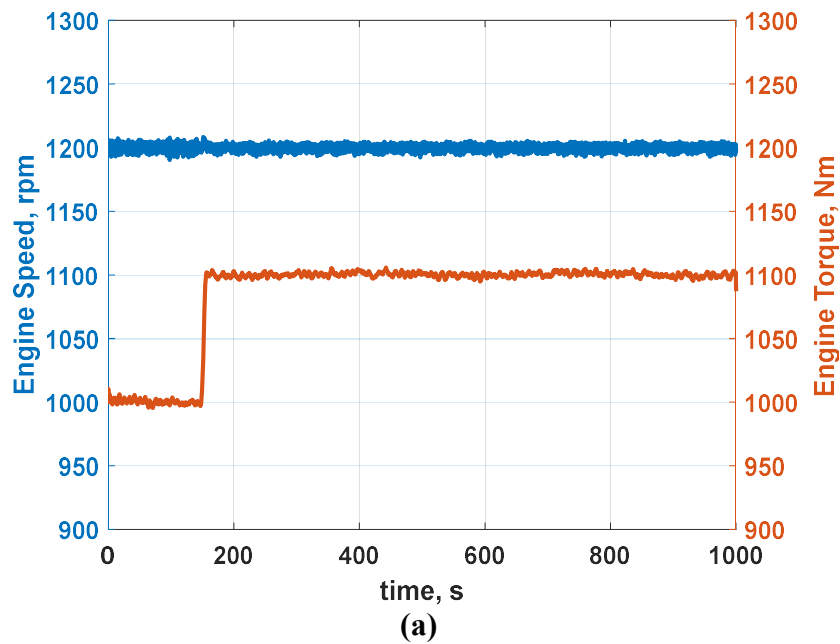
One of the biggest challenges of HDD engine ORC system implementation is the transient nature of the various heat sources. As the engine encounters different speed/load transients during real-world operation, there are abrupt yet disparate mass flow rate and temperature changes in both the TP and EGR gas streams. This transient behavior exposes many control challenges, which are difficult to address with traditional feedback control while simultaneously attempting to minimize system expense and component complexity. Most advanced control strategies require component and system models, emphasizing the importance of accurate ORC component modeling.

## **1.2 Open Loop Experimental analysis**

It is important to understand the open loop system dynamics before designing a control solution. An open loop experimental evaluation is performed in this section to understand the different time constants involved for the ORC system in consideration. For an ORC-WHR system, the engine exhaust gas mass flow rate and temperature are uncontrollable inputs whereas pump speed is the controllable input that maintains the working fluid flow through the ORC system. The effects of step changes to controllable and uncontrollable inputs on working fluid temperature are analyzed herein to elucidate the critical system dynamics. The experiments are conducted on a 13 L Heavy Duty Diesel engine in AVL's engine dynamometer. AVL's PUMA software is used to

record temperature and mass flow data of the ORC system and of engine exhaust conditions. The experimental setup is shown in Figure 1.2. For more information refer to section 5.3. The TP evaporator is placed downstream of the after-treatment system for two reasons; 1) to capitalize on thermal energy from the reactions within the after-treatment system, and 2) to avoid interfering with the after-treatment system functionality. Thermocouples and pressure transducer are placed at each of the locations 1, 2, 3 and 4 as shown in Figure 1.2. Coriolis mass flow meters are located at junction 2 and are used to measure the working fluid flow going into the evaporator.

### *1.2.1 Step Change in Uncontrollable Input – Engine Conditions*



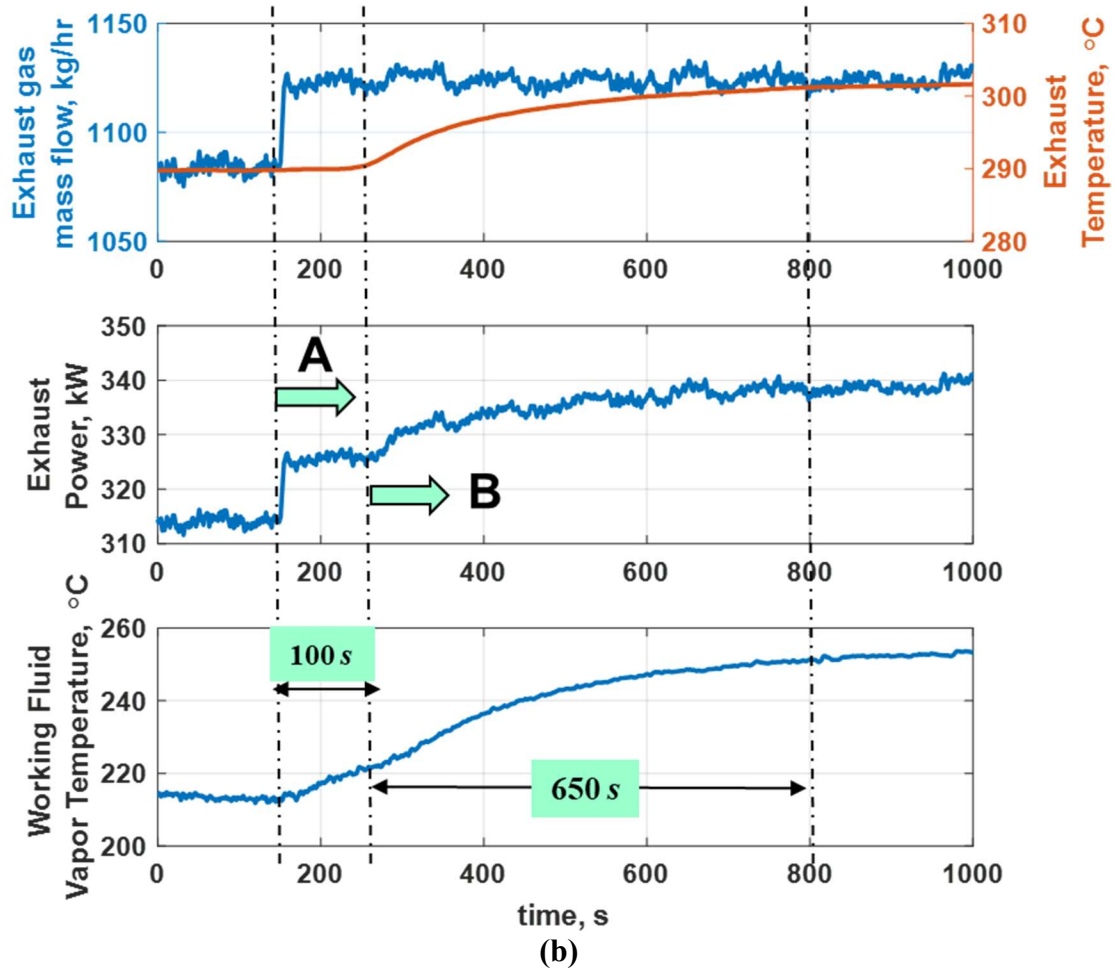


Figure 1. 4. (a) Engine condition for a step change in torque and (b) corresponding exhaust conditions at the evaporator inlet exhaust power at the evaporator inlet, and working fluid temperature response at the evaporator outlet.

In this test, a step change in engine torque is evaluated at constant engine speed. Figure 1.4(a) shows the engine conditions and the top plot of Figure 1.4(b) shows the corresponding exhaust conditions. As seen from the Figure 1.4, the change in engine exhaust gas mass flow occurs rapidly whereas the exhaust temperature change is temporally delayed due to the thermal inertia of the after-treatment system located between the engine and the evaporator. After every change in engine conditions, the thermal inertia of the after-treatment system takes a finite amount of time to arrive at steady state.

The bottom graph of Figure 1.4 (b) shows the corresponding change in working fluid temperature at the evaporator outlet with a settling time of 650 sec. This slow settling time of the working fluid temperature at evaporator outlet is a function of the after-treatment systems thermal inertia. Exhaust power is a function of exhaust flow and temperature. At 150 s, when the step change in engine torque is initiated, the exhaust power at the evaporator inlet changes instantaneously due to the fast dynamics of the exhaust mass flow rate, represented by region A in figure 1.4 (b). The change in exhaust gas mass flow rate shows up as a linear trend in the working fluid outlet temperature during this region. Region A persists for 100 s after which the evaporator inlet exhaust temperature begins to rise, increasing the exhaust power in region B. Correspondingly, the rate of working fluid temperature rise increases.

The heat flow in the evaporator is a two-step process, first the heat source transfers energy to the tube wall and then, from the tube wall, the heat is transferred to the working fluid. In the first step of the heat transfer process, thermal inertia, i.e. the wall thickness, evaporator design and selected wall material, along with the exhaust conditions affects the rate of heat transfer process. For a given evaporator design, this rate will change based on the engine operating condition. The heat transfer rate in the second heat transfer step, from the wall to the working fluid, is dictated by the working fluid type, mass flow rate, and phase. Figure 1.4 (b) shows that the working fluid temperature dynamics are a function of both after-treatment thermal inertia and the evaporator thermal inertia. The rate of heat transfer in the evaporator can be manipulated by adjusting the pump speed as shown in the following section.

### *1.2.2 Step Change in Controllable Input – Working Fluid Pump speed*

In this test, engine conditions were kept constant while the working fluid pump actuator position was subjected to step changes as seen from Figure 1.5. For each 3% step change in

actuator position, the pump speed change by 100 rpm, directly altering the working fluid mass flow rate. During this experiment, the turbine bypass valve is completely closed and turbine valve is completely opened. These fixed valve position allowed the evaporation pressure to change with the working fluid mass flow rate.

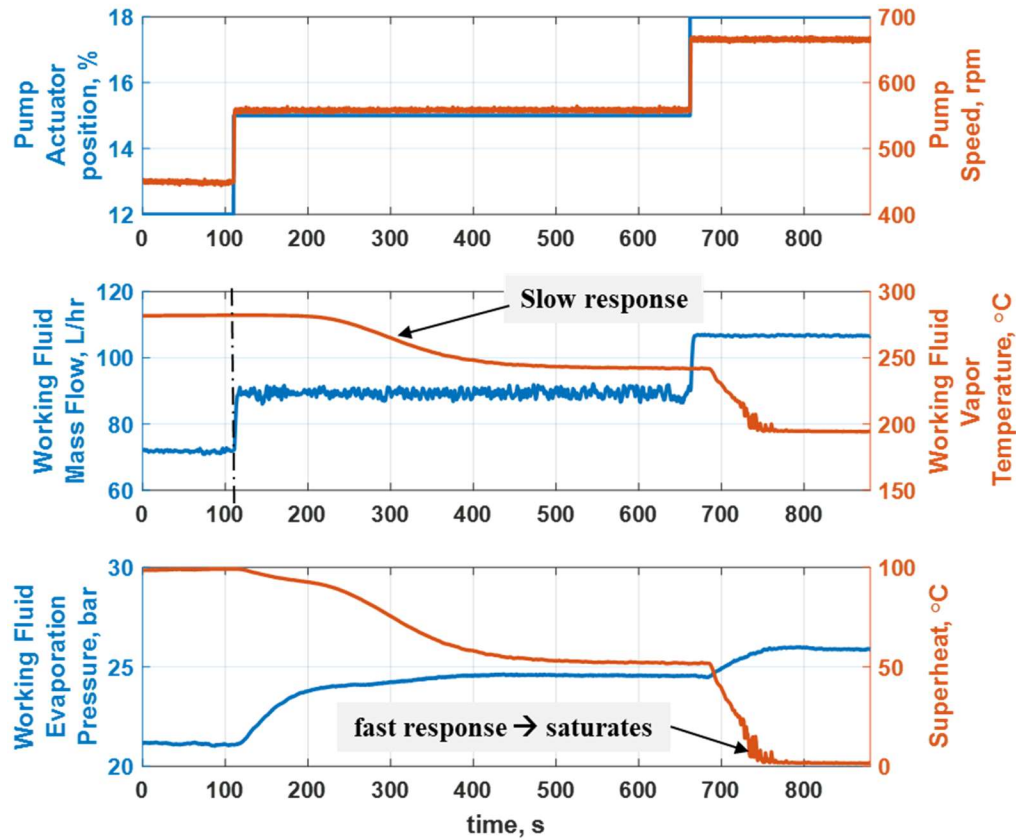


Figure 1. 5. Working fluid evaporator outlet temperature response to the step-change in pump-actuator position.

The initial working fluid step change at 100s stimulated a slow working fluid temperature response, steady state at around 400 s as shown in Figure 1.5. The second 3% high speed pump step change created a faster working fluid temperature response, eventually resulting in working fluid saturation. The fixed valve position operation sets in motion a chain of events, which causes this disparate response. The evaporation pressure varies proportionally with the working fluid mass flow which in turn alters the evaporation temperature proportionally. These compounding effects

create the disparate severity in response to the two working fluid mass flow changes. Thus to avoid saturation, control systems must take care in defining both the operating region and the rate of control input change. This behavior also illustrates the non-linear nature of the ORC system, as the system response varies with operating condition and the working fluid state.

From Figure 1.4 and 1.5, it can be also concluded that the input dynamics (pump speed/working fluid flow and evaporation pressure) are faster than the output dynamics (working fluid temperature).

### 1.3 Problem statement

Rankine cycles are very well established and in use for numerous stationary application where there are little concerns of any transients interrupting the WHR system operation. However, for any WHR-ORC system in an automotive application, the heat source is highly dynamic and therefore the control of the ORC system should be carefully structured. The control strategy should not only be able to deal with the highly dynamic heat source but should also consider the actuator physical constraints and working fluid temperature constraints without inhibiting turbine operation. Finally, the overarching goal is to maximize the power output, i.e. waste heat recovery, over a typical drive cycle. The aforementioned controls requirement clearly falls within the scope of Model Predictive Control. In comparison to classical PID strategy, utilizing an MPC strategy has following advantages:

- 1) It can save significant calibration and tuning resources especially if one or more evaporator are utilized in the ORC system. In such cases, MPC needs minor updates to objective function and constraints.
- 2) It is perfectly capable of handling multivariable problems
- 3) It explicitly considers constraints in the optimization process

- 4) It is also capable of rejecting disturbance or modeling error by utilizing state feedback at each step.
- 5) Lastly, the preview feature of MPC takes into account the future inputs and optimize the control sequence for the entire prediction horizon.

Many studies have compared the classical PID controller which is the state of the art in the automotive industry and MPC, an advanced model based control technique [17-22]. In all these studies, it was shown that MPC outperforms PID controller in maintaining the vapor state at the evaporator outlet in a transient driving conditions. An opportunity for further improvement is anticipated in the context of vehicle connectivity and look-ahead strategies that rely on a known horizon. Thus improving the ORC systems power generation capability.

The development of MPC can be found as early as 1970s. Since then multiple MPC techniques have being developed that uses a model based approach to predict the future control inputs. Some authors have exploited EPSAC [17-18] as an MPC technique to improvise the power production from an ORC system. The advantage of using EPSAC is that it allows the use of input-output models in form of transfer function thus avoiding the need of state estimators. This also limits the usage of that transfer function within the identified range of the model. While others [19, 23] have used linear MPC where the non-linear evaporator model is linearized over a predefine set of points. The drawbacks of linear MPC is that it requires a different linear model for different operating conditions. Tuning, each linearized MPC would be additional challenges for smooth switching between multiple models. However, very few studies have used nonlinear MPC with state estimators.

In summary, the main goal of this research is to investigate a Non-linear MPC (NMPC) with augmented EKF (Extended Kalman Filter) as state estimator. The scope of the sub-tasks is derived



from the main objective, i.e. the additional chapters will address development of enabling modeling capabilities, error analysis based on model/measurement inaccuracies, as well as experimental validation of the proposed control approach. The EKF is augmented with a disturbance model to reject both modeling and measurement errors. Since MPC is model based approach, first an enhanced finite volume modeling methodology is presented that enhances phase length estimation inside the evaporator. This model can be then used to calibrate and tune control oriented model.

### 1.3 Objectives

The main objectives of this dissertation are to develop:

1. Enhanced evaporator model for estimating phase lengths - A methodology is described and validated to predict phase lengths inside the evaporator. (Chapter 2)
2. Augmented EKF model - The estimator is augmented with disturbance rejection model to take into account modeling errors and instrumentation inaccuracies (Chapter 4). The performance of which is experimentally validated in Chapter 5.
3. MPC with preview - The benefits of MPC with preview capability is explored where future exhaust conditions are known. MPC with preview showed benefits in reducing the control effort and in some instances better superheat tracking ability. (Chapter 4)

### 1.4 Dissertation Outline

Chapter 2, explains the evaporator modeling and introduces methodology to enhance the phase length estimation undergoing beneath the surface of the evaporator. This methodology uses PSO (Particle Swarm Optimization) technique for identification of additional multipliers to improve the heat transfer coefficient. The identified multipliers and methodology is validated using transient thermal image data.

In Chapter 3, following the experimental open loop study, efforts have been made to understand the open loop characteristics of the actuators, inputs-output correlation and the thermal inertia affecting the evaporator dynamics in a simulation environment.

In Chapter 4, MPC control strategy is explained with the problem formulation. For model based controls approach, it's very crucial to model the system as accurate as possible. Sometimes it's extremely hard to model the actual system and in such cases, a disturbance model can be incorporated in an MPC controls strategy. This is also explored and explained in Chapter 4. One other important aspect which has not being investigated in literature for a WHR-ORC is its preview capability. With known future inputs MPC can provide much better results from an optimization stand-point.

Chapter 5, experimentally validates the developed MPC strategy for a TP evaporator. Step inputs and drive cycles are used to tune and evaluate the performance of the MPC strategy. Sinusoidal drive cycle with varying time period suggest that the thermal inertia plays a vital role in buffering some of the high frequency exhaust conditions. Finally, the thesis ends with conclusions, and future work in Chapter 6.

## CHAPTER 2. EVAPORATOR MODELING

### 2.1 Introduction

This Chapter presents the modeling and validation of a counter-crossflow heat exchanger used to extract thermal energy from Heavy-Duty Diesel (HDD) engine exhaust. The finite volume evaporator modeling methodology is enhanced for both accurate working fluid temperature and phase length estimation, facilitating improved offline waste heat recovery simulation and accurate control-oriented model development.

Transient model calibration and validation experiments were performed on a stand-alone flow bench. Heated gas was passed through the evaporator, replicating different engine exhaust gas conditions. In contrast to other studies, thermal imaging data served to identify the working fluid liquid, mixed and vapor phase lengths within the evaporator. The FVM modeling methodology was enhanced based on the thermal imaging data to accurately predict the working fluid phase lengths. Once calibrated, working fluid phase lengths predicted by the proposed model were validated against thermal imaging from additional transient experimental flow bench data sets.

### 2.2 Background

#### 2.2.1 Heat Exchanger Modeling

Literature studies reveal two approaches for heat exchanger modelling, 1) a Finite Volume Model (FVM) and 2) a Moving Boundary Model (MBM). The FVM is a discretized model, dividing the evaporator into multiple uniform cells and solving the energy balance equations in each cell. Such an approach yields high accuracy at the expense of computation speed [24-26]. FVM discretization depends on the amount of accuracy and computation time required for a given application. Numerous published studies [20, 25-27] have utilized FVM for both stationary and on-road applications.

MBM are generally implemented for control purposes because of their low computation cost [28-30]. Unlike an FVM, the MBM solves the energy balance equations in only three cells, one for each working fluid phase: pure liquid, mixed phase (liquid and vapor) and pure vapor. The size of each computational cell is free to vary with the lengths of each working fluid phase during transients. Unfortunately, MBM calibration currently relies on only sensible parameters, such as the entry and exit temperatures of both the working fluid and the heat source, because no studies have examined the physical working fluid phase lengths. The utilization of tuned empirical correlations describing the heat transfer in each phase presents a case where the MBM could experience substantial deviation in the relative working fluid phase lengths and still arrive at the correct working fluid exit temperature. While this inaccuracy can be acceptable in some instances, this flaw becomes problematic when MBM are utilized for control, as the phase lengths are often the states of interest during implementation [28, 31].

### *2.2.2 Importance of Phase length estimation*

ORC WHR control strategies often critically rely on working fluid evaporator outlet temperature prediction [20, 28-30], which is especially important when utilizing a turbine expansion device. Due to the high rotational speeds of turbine expanders (10,000-120,000 rpm), induction of working fluid droplets damages the turbine blades. Thus, during normal operation of the turbine expander working fluid must be in vapor condition only. This constraint challenges modern ORC WHR control strategies to accurately predict and control the evaporator working fluid exit conditions during vehicle transients to avoid bypassing multi-phase working fluid around the turbine, sacrificing power generation.

Redeveloping predictive ORC-WHR control strategies to also consider the working fluid phase boundary locations within the evaporator provides an avenue for enhanced ORC-WHR power

generation during real-world operation. Knowledge of the mixed-phase to vapor boundary location within the evaporator can provide an estimate of the real-time vapor ‘buffer’ before working fluid evaporator exit conditions reach saturation. When utilized in conjunction with working fluid mass flow and models of the compressible pipe volumes, an enhanced predictive control could alter ORC system operation well in advance of detrimental working fluid saturation at the evaporator outlet. Unfortunately, no validated physics-based models exist for prediction of the working fluid phase change location. Error in the phase boundary estimation could lead to saturated exit conditions during highly transient engine operation, which reduces the expander machine power production duration, leading to Rankine cycle efficiency reduction. These considerations create the motivation for research in this chapter.

### 2.2.3 Sensitivity of ORC-WHR Energy Recovery to Working Fluid Phase Length

To illustrate the importance of phase boundary layer estimation accuracy, a feedback plus feedforward control is designed to regulate the vapor phase length as shown in Fig. 2.1. The heat exchanger model utilized is a FVM and exhaust conditions are collected offline from a 1-D GT-POWER engine model developed in [32]. The controller outputs the working fluid pump speed, which is inversely related to working fluid vapor phase length.

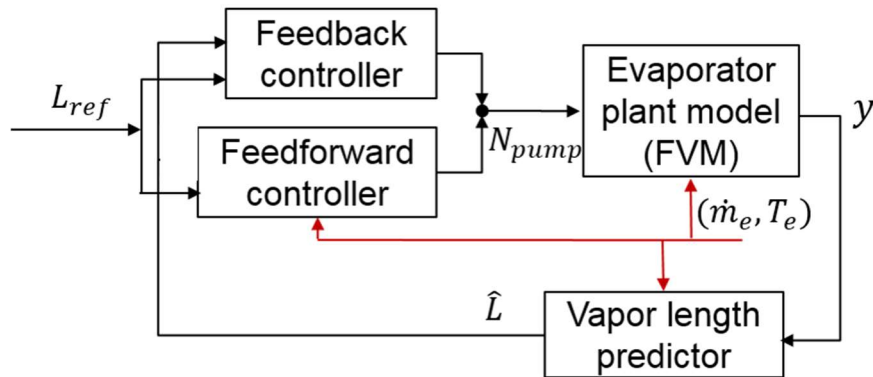


Figure 2. 1. Vapor phase length control diagram.

The target vapor phase length is held constant at 10% of the total evaporator length. Hypothetical vapor phase length estimation model errors of 7% and 2% (both overestimating the vapor phase length within the evaporator) are then simulated during a step down in engine speed and torque. In the example, a simultaneous step down of engine speed and torque is considered (namely, from 1500rpm, 1250Nm to 1400rpm, 1000Nm). Fig 2.2 shows the results of vapor phase length, turbine power, and accumulative energy from a waste heat recovery system with the aforementioned errors in phase length prediction. In Fig 2.2(a), the simulation with insertion of the 7% phase length estimation error undergoes a period of saturation (i.e. vapor phase length falls to zero), whereas the simulation with 2% phase length estimation error maintains vapor phase along the entire 1000s test case. Based on the results at 200s in Fig 2.2(a), we can deduce that if the vapor phase length within the evaporator can be predicted within 6%, the saturation period could be avoided during this transient. In the Fig 2.2(b), when the phase estimation error is 7%, the turbine is bypassed for the duration of the saturation period, resulting in a 9 % reduction in cumulative energy collected over the transient. Minimizing the phase length prediction error can maintain turbine power production without interruption and improve the effectiveness of waste heat recovery.

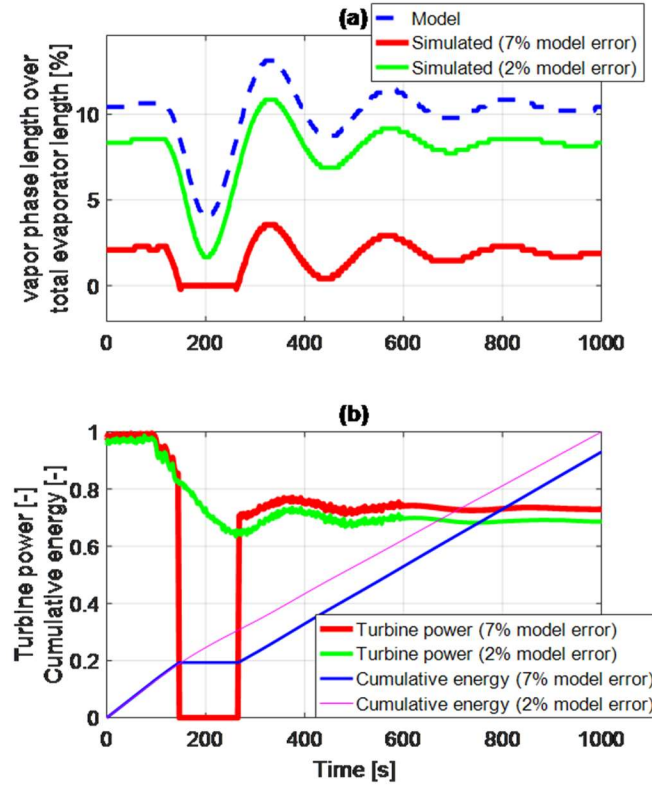


Figure 2. Organic Rankine cycle waste heat recovery system power comparison between two working fluid boundary layer estimation accuracies: (a) vapor phase length over the total boiler length as a percentage, and (b) normalized turbine power and normalized cumulative energy. In the legends, 7% model error means the results from a simulation subject to a vapor phase length estimation error of 7% prior to the feedback control. In contrast, 2% model error means the results from a simulation with a 2% vapor phase length estimation error prior to the feedback control.

### 2.3 System Configuration

Figure 2.3 illustrates the evaporator design utilized in this study. The Figure schematically represents a simplified version of the actual evaporator, due to intellectual property constraints surrounding the novel evaporator design. The exhaust gas enters on the right and leaves the evaporator on the left. Ethanol, the working fluid selected for this study, enters the evaporator core on left top and splits into vertical tubes, which are arranged in counter-cross flow direction with respect to exhaust gas.

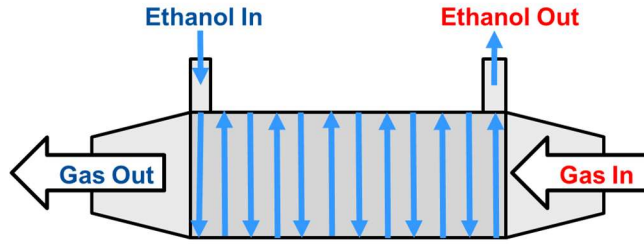


Figure 2. 3. Evaporator design schematic.

The evaporator is connected to a flow bench, which is supplied with hot exhaust from a gas burner. A FLIR A300 thermal camera is utilized to capture temperature changes along the evaporator's skin. An example of captured thermal image is shown in Figure 2.4.

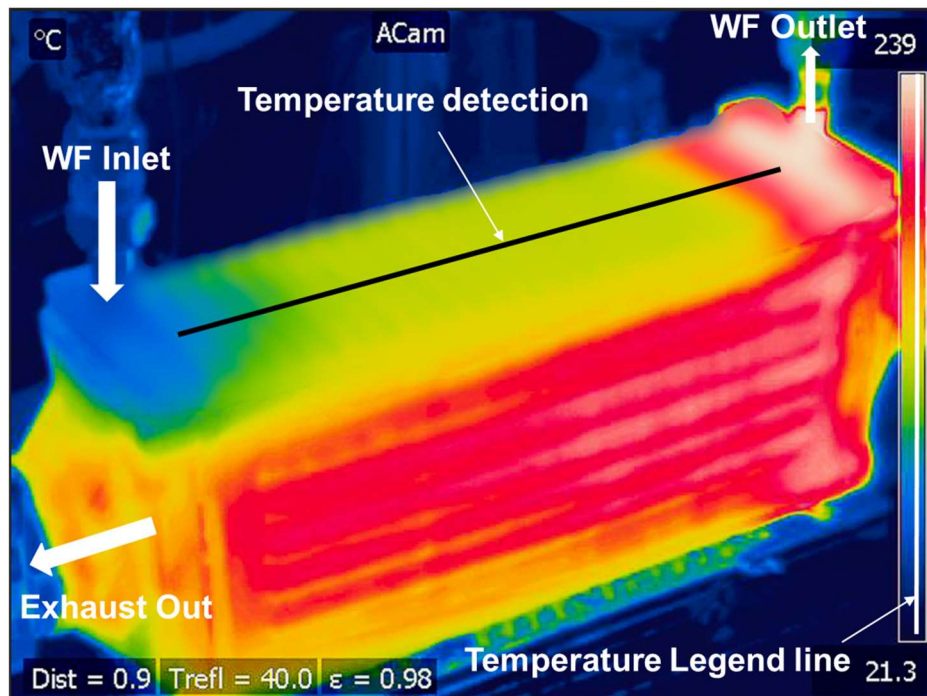


Figure 2. 4. An example of the Thermal Image from FLIR A300 camera utilizing an 18mm lens displaying the line chosen for detailed temperature analysis from the thermal images. In consideration of the sponsor's intellectual property rights, some features of the evaporator have been intentionally blurred.

Figure 2.4 is purposely blurred to hide proprietary design features of this evaporator. However, the reader can still distinguish the color stratification across the top of the evaporator, which indicates the working fluid temperature variation during transitions from liquid (blue) to mixed-



phase (green-yellow) and then to vapor (red). Thermal video is captured during transient flow-bench tests. With the availability of this thermal data at different conditions, the next task is to process the images and extract the working fluid phase lengths along the evaporator core.

## 2.4 Thermal Image Processing

This section overviews the methodology for extracting thermal image temperature information at each point along a line spanning the length of the evaporator between the working fluid inlet and outlet, as shown in Figure 2.4.

### 2.4.1 Still Image Processing

The in-house thermal image processing methodology includes three aspects:

1. Converting pixel to pixel distances along the isometrically-oriented evaporator images to a physical distance;
2. Extracting quantified temperature information along the line of interest from the images;
3. Detecting the working fluid phases from the extracted temperature information.

The Forward Looking Infrared (FLIR) thermal imaging camera used for capturing the thermal images and videos provided an isometric view of the boiler as shown in the Figure 2.4. Projection of a 3D object to a 2D plane implies the loss of information about the depth of the object. Consequently, to accurately determine the distance to each point on the boiler from a given reference point a quadratic fit was used based on the measured physical distance between the two different points from the reference. This function converted the distance in terms of pixels to a physical distance.

FLIR Tools software determined the temperature at each pixel of the thermal images. The location for each point along the line was converted to pixel coordinates. The temperature at each

point was then determined using the temperature data from FLIR tools by matching the pixel coordinates.

#### *2.4.2 Video Processing*

The transient FLIR videos, on the other hand, lacked the metadata required for FLIR Tools to provide any temperature information. The data obtained from the project industrial sponsor had undergone post-processing to reduce the file size. As such, an in-house processing methodology was developed to extract the temperature information.

The key strategy for extracting temperature information from the videos was to match the color of each of point on the line of interest to the video's legend. The colors on the legend remain constant for the duration of each transient test. However, based on the actual temperatures achieved in each transient test case, the upper and lower limit of the temperature scale changed between videos. Since the highest and lowest temperature for each video was known, a simple linear fit was created between these two temperatures. Initial attempts sought the translation of each video still frame to grayscale for temperature identification. However, this approach led to ambiguous results due to the identical grayscale intensities for two or more different colors from the legend, and it was thus abandoned.

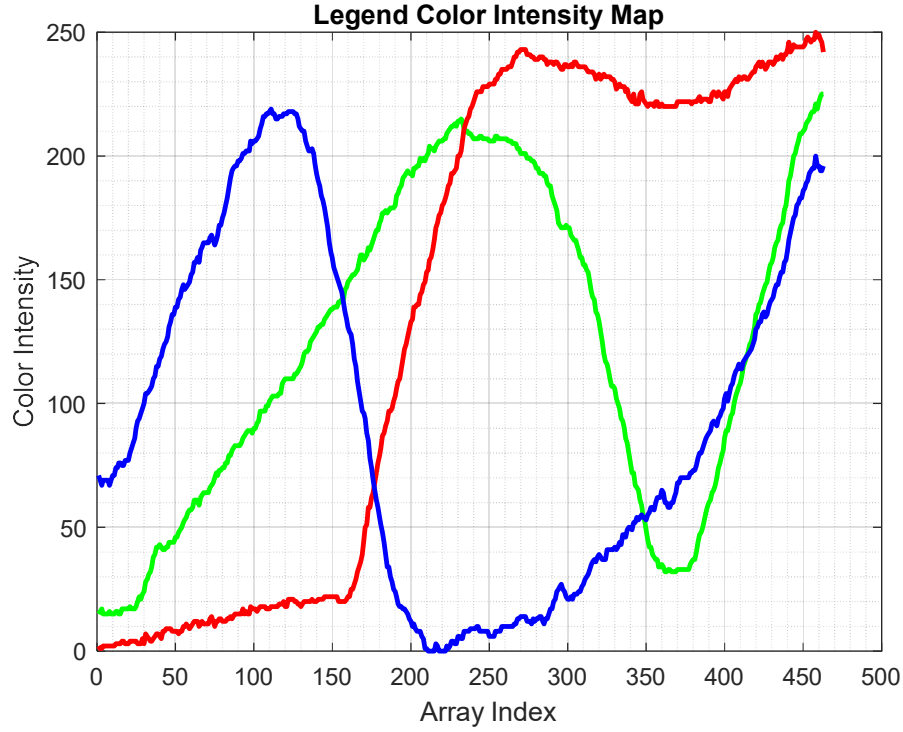


*Figure 2. 5. Comparison of RGB intensities on each point on the temperature detection line.*

The procedure for analyzing the color videos as follows: the red, green and blue intensities must be compared at each point from the line of interest to the image's color scale legend. The color intensities from each point of the temperature legend were plotted, as shown in Figure 2.5. The red intensity component was then utilized to split the temperature identification space into three zones with the array index increasing in the direction of increasing temperature. Until an index of 150, the red component intensity increases linearly at an approximately constant rate. Between 150 and 220, the red intensity continues to be linear, but at a much faster rate of increase. The linear trend is lost only beyond an array index of 220. These three ranges were then utilized within the in-house software to narrow the search space when identifying the temperature of any pixel from the image. Once the search space was narrowed, the difference in color between the point along the line of interest and legend entries in that sector was then found by the following equation:

$$\Delta = (R_{legend} - R_{line})^2 + (G_{legend} - G_{line})^2 + (B_{legend} - B_{line})^2$$

The legend array index that yielded the minimum difference relative to the point of interest was then fed into the linear function to convert the pixel location to a temperature value. For validation, this procedure was applied to still images where full temperature discretization was available via the FLIR Tools. The trend in temperatures for any still image was preserved, providing confidence for identification of the working fluid phase change locations during the transient tests. The offset noted in Figure 2.6 could be due to the line of interest not referring to the exact same locations in the video and the image used.

Once the temperature data is extracted from any still image, the pixels along the line of interest must be properly assigned to a physical length along the evaporator herein referred to as working fluid ‘tube distance’. A sample result of the temperature mapping and subsequent length assignment is provided in Figure 2.7.

Since temperature data was extracted only from the top surface of the evaporator, the length assignment process has a length scale discretization corresponding to twice the evaporator height, owing to the evaporator design illustrated in Figure 2.3.

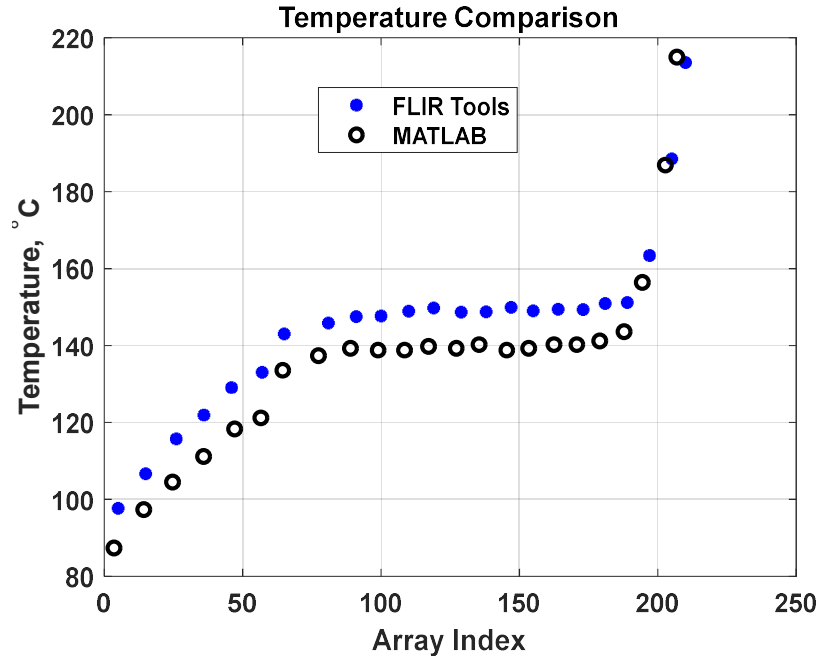


Figure 2. 6. Temperature comparison data between FLIR tools and Matlab code operating on the same still thermal image.

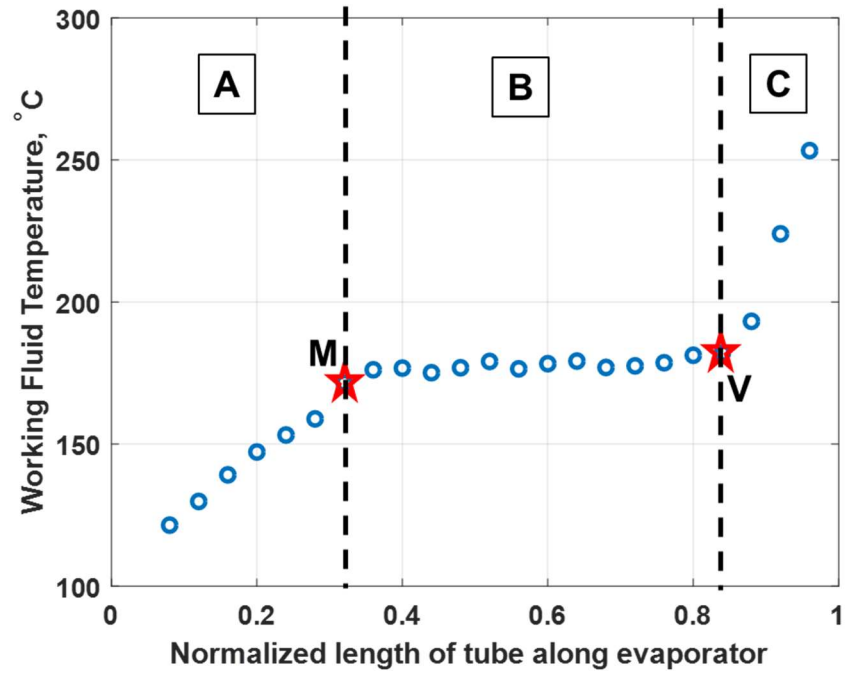


Figure 2. 7. Extracted temperatures along the top surface of the evaporator (along the defined line of interest shown in Figure 2.4) with respect to normalized working fluid tube length in the evaporator. Also shown are the three regions of interest (A-C), corresponding to the different working fluid phases.

### *2.4.3 Phase Change Detection*

As shown in Figure 8, there are three possible regions of interest inside the evaporator, corresponding to the three phase regions of the working fluid: (i) Region A is the pure liquid phase; (ii) Region B represents the mixed-phase region (saturation) where both liquid and vapor working fluid exist; and (iii) Region C represents the pure vapor phase. In region A, where the working fluid temperature is below the saturation temperature, heat transfer is initially single phase convection. As the temperature rises through the subcooled region towards point the ‘mix point’, ‘M’, vapor begins appearing from nucleation sites. This mechanism of heat transfer is termed as subcooled nucleate boiling [33].

The transition between regions A and B, is shown as point ‘M’ where the subcooled nucleate boiling heat transfer is converted to saturated nucleate boiling. Heat transfer in region B is characterized by the working fluid quality. Temperature variation is noted in region B due to local differences in pressure and vapor formation. As the quality of the vapor increases through region B, nucleation is suppressed and heat transfer is a result of two-phase forced convection. This two-phase region is characterized by very high heat transfer coefficients, which will be discussed later in this paper.

At point the vapor transition point, ‘V’, of Figure 2.7, the working fluid quality reaches unity. Heat transfer in the vapor region is due to convection within the vapor film. To determine points ‘M’ and ‘V’ from the thermal image results, saturation temperature is calculated based on the evaporator pressure for each test. Point M is assigned as the first point along the evaporator length where observed fluid temperature reaches the saturation temperature. The first instance where observed temperature surpasses the saturation temperature is then identified as point ‘V’.

The aforementioned length scale discretization due to the use of thermal data from only the top evaporator surface plays an important role in detection of the working fluid phase change locations. The thermal images only provide temperature data at the end or the beginning of each vertical tube within the evaporator. Thus, the actual phase change location could be at any point along the vertical tube length between adjacent top surface locations. The actual mix point can be between point M and the immediately following top surface temperature point whereas the actual vapor point can be between point V and the immediate preceding point. Thus, the certainty of experimentally determined working fluid phase changes is limited by twice the evaporator height.

## 2.5 Evaporator Modeling

In an ORC-WHR system, there are two types of heat exchangers: evaporators which accept thermal energy from heat sources, and condensers which reject thermal energy from the ORC loop. ORC system efficiency depends critically on evaporator design and performance. As such, the accuracy ORC system models heavily relies on the evaporator model. Two assumptions are made for evaporator modeling described herein: (i) axial heat conduction (along the working fluid tube length) in working fluid, wall and exhaust gas are neglected, and (ii) the wall temperature is uniform across the tube wall thickness. In addition, experimental results have shown minimal pressure drop across the evaporator, and hence pressure drop is neglected in this modeling work. Mass balance, energy balance and momentum balance principles are all considered in evaporator modeling. The modeling work contained herein is adopted from Bin Xu et al. [32, 34]. Transference of the main modeling methodology is first confirmed by applying said methodology to the current evaporator, which is a substantially different physical design from the previously published work. Subsequent sections will then enhance the modeling methodology to obtain additional phase length prediction accuracy. Only the relevant equations of the underlying FVM

methodology are outlined in this work. For a complete overview of the modelling methodology, readers are guided to prior works [32, 34].

The working fluid mass balance is presented in Eq. (2.1).

$$\frac{\partial A_{f,cross} \rho_f}{\partial t} + \frac{\partial \dot{m}_f}{\partial z} = 0 \quad (2.1)$$

where subscript  $f$  denotes fluid,  $A_{cross}$  is the cross-sectional area,  $\rho$  is density,  $\dot{m}$  is mass flow rate, and  $z$  is axial position along the evaporator tube length.

The energy balance for both the working fluid and the exhaust gas share the same general form, which is presented in Eq. (2.2)

$$\frac{\partial (A_{cross} \rho h - A_{cross} p)}{\partial t} + \frac{\partial \dot{m} h}{\partial z} = \pi d U \Delta T \quad (2.2)$$

where  $p$  is pressure,  $h$  is enthalpy,  $d$  is the effective flow path diameter for either the working fluid or exhaust gas,  $U$  is the heat transfer coefficient, and  $\Delta T$  is the temperature difference between the fluid (working fluid or exhaust gas) and the wall.

The tube wall energy balance is shown in Eq. (2.3)

$$A_{w,cross} c_{p,w} \rho_w L_w \frac{dT_w}{dt} = A_{f,w} U_{f,w} \Delta T_{f,w} + \eta_m A_{e,w} U_{e,w} \Delta T_{e,w} \quad (2.3)$$

where subscript  $w$  denotes wall,  $c_p$  is heat capacity,  $L$  is the length in axial direction,  $A_{f,w}$  represents the heat transfer area between working fluid and wall,  $U_{f,w}$  is the heat transfer coefficient between working fluid and wall,  $\eta_m$  is the heat exchanger efficiency multiplier that accounts for heat loss to the environment,  $A_{e,w}$  is the heat transfer area between exhaust gas and wall, and  $U_{e,w}$  is the heat transfer coefficient between exhaust gas and wall.

Ordinary differential equations of Eqs. 2.1 and 2.2 are represented as follows:

$$\frac{d\dot{m}_f}{dt} = \dot{m}_{f,in} - \dot{m}_{f,out} \quad (2.4)$$

$$\frac{d(\dot{m} h - v p)}{dt} = \dot{m}_{in} h_{in} - \dot{m}_{out} h_{out} + A U \Delta T \quad (2.5)$$



where subscripts *in* and *out* denote spatial context in the axial direction, and *v* is the working fluid volume in one discretized cell.

Eqs. 2.3–2.5 can be solved by utilizing 1D Euler differentiation as shown by Eqs. 2.6-2.8:

$$T_{w,t(k+1)} = T_{w,t(k)} + \eta_m \frac{A_{f,w} U_{f,w} \Delta T_{f,w} + A_{e,w} U_{e,w} \Delta T_{e,w}}{A_{w,cross} c_{p,w} \rho_w L_w} \Delta t \quad (2.6)$$

$$m_{f,t(k+1)} = m_{f,t(k)} + (\dot{m}_{f,in} - \dot{m}_{f,out}) \Delta t \quad (2.7)$$

$$(mh)_{t(k+1)} = (mh)_{t(k)} + \frac{d(vp)}{dt} + (\dot{m}_{in} h_{in} - \dot{m}_{out} h_{out} + AU \Delta T) \Delta t \quad (2.8)$$

where  $\eta_m$  is again the efficiency multiplier that accounts for the heat losses from exhaust gases to environment, *k* is the time step indices, and  $\Delta t$  is the time step length.

Figure 2.8 illustrates the finite volume modeling methodology. The heat exchanger is theorized to be a long, straight tube which is divided into *N* cells. Within each cell, heat flows from the exhaust to the wall and finally to the working fluid. Exhaust gas flows from the right to the left and temperature gradually decreases, whereas working fluid flows from left to right and temperature gradually increases. Meanwhile, the working fluid enters as liquid phase and exits as vapor phase. For each discretized cell, the FVM solves Eqs. 2.6, 2.7 and 2.8 simultaneously.

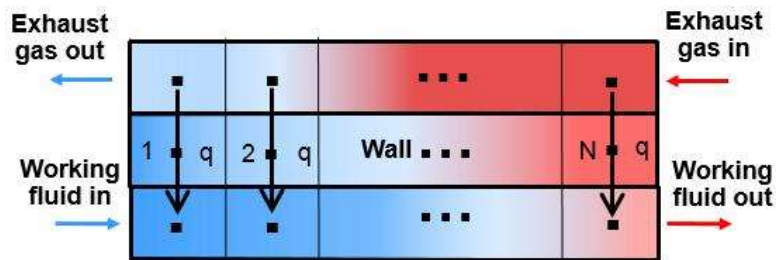


Figure 2. 8. Schematic representation of Finite Volume Method used for evaporator modeling.

### 2.5.1 Heat Transfer Coefficients

The evaporator in [32, 34] utilized a helical coil type tube structure whereas the evaporator tubes in the current device are arranged vertically. Hence a new set of equations for the respective heat transfer coefficients are described in this section. In an evaporator, heat is transferred from high temperature, high flow exhaust gases to the working fluid. The heat transfer coefficient for each working fluid phase is calculated utilizing the average Nusselt number for that phase and the evaporator tube geometry. The average Nusselt number,  $Nu$  is calculated as follows,

$$Nu = \frac{\alpha * d_h}{\lambda} \quad (2.9)$$

where  $\alpha$  is the heat transfer coefficient,  $d_h$  is the hydraulic diameter, and  $\lambda$  is thermal conductivity.

Flow is defined to be a turbulent or laminar depending on the Reynold's number, which is calculated using Eq. (2.10) where  $\nu_k$  is defined as kinematic viscosity and  $\nu_f$  is defined as flow velocity and is calculated using Eq 2.11.

$$Re = \frac{\nu_k * d_h}{\nu} \quad (2.10)$$

$$\nu_f = \frac{\dot{m}}{\rho * A_{flow}} \quad (2.11)$$

Since exhaust gas dynamics are fast relative to changes in working fluid enthalpy, a single value of heat transfer coefficient between the exhaust gas and the tube wall is utilized for the entire evaporator. As the exhaust gas traverses through the evaporator, the gas velocity gradually decreases. Hence, an average Nusselt number is used for the exhaust gas to tube wall heat transfer calculation. The heat transfer coefficient between exhaust gases and the wall is given as:

$$U_{e,w} = m_U \frac{Nu_e k_e}{d_e} \quad (2.12)$$

where  $d_e$  is the stream length of a single tube, and  $m_U$  is the heat transfer coefficient multiplier that accounts for differences between the actual evaporator construction compared to the vertical

tube type structure.  $Nu_e$  is the average exhaust gas Nusselt number based on the evaporator geometry given by the expressions (2.13 – 2.16) [33]:

$$Nu_e = 0.3 + (Nu_{e,laminar}^2 + Nu_{e,turbulent}^2)^{0.5} \quad (2.13)$$

$$Nu_{e,laminar} = 0.664 * \sqrt{Re_{\psi,l}} * Pr_e^{1/3} \quad (2.14)$$

$$Nu_{e,turbulent} = \frac{0.037 * Re_{\psi,l}^{0.8} * Pr_e^{\frac{2}{3}}}{1 + 2.443 * Re_{\psi,l}^{-0.1} * (Pr_e^{\frac{2}{3}} - 1)} \quad (2.15)$$

$$Re_{\psi,l} = \frac{w d_e}{\psi v_f} \quad (2.16)$$

where  $d_e = (\pi/2)d_o$  is the streamed length of a single tube (i.e., the length of the flow path traversed over a single tube) with inner diameter  $d_o$ . Void fraction,  $\psi = 1 - \pi/4ab$ , where the transverse pitch ratio is expressed as  $a = s_1/d_o$  and the longitudinal pitch ratio is calculated as  $b = s_2/d_o$ . For these expressions,  $s_1$  and  $s_2$  are the lateral and longitudinal spacing between tubes, respectively.

The exhaust gas thermal conductivity,  $k_{e,TP}$ , required in Eq 2.12, is expressed as:

$$k_e = 1.07 + \frac{900}{Re_e} - \frac{0.63}{(1+10P_e)} \quad (2.17)$$

For the working fluid, individual heat transfer coefficients are assigned based on the fluid phase. The vertical orientation of the working fluid tubes and the presence of a fully turbulent working fluid flow (as calculated via the Reynolds number) results in utilization of the Gnielinski correlations corresponding to flow in vertical tubes [33]. The pure liquid and pure vapor phase heat transfer coefficients are generated with equations (2.18) and (2.19)

$$U_{f,i} = \frac{\left(\frac{\xi_{f,TP,i}}{8}\right) Re_{f,i} Pr_{f,i}}{1 + 12.7 \sqrt{\frac{\xi_{f,TP,i}}{8}} (Pr_{f,i}^{0.667} - 1)} (1 + (d/l)^{0.667}) \frac{k_{f,i}}{d_{f,i}} \quad (2.18)$$

$$\xi_{e,i} = (1.8 \log_{10}(Re_e^*) - 1.5)^{-2} \quad (2.19)$$

where  $i$  represents the chosen phase (i.e. either fluid or vapor).

For two phase working fluid flow, the heat transfer coefficient between the fluid and the tube wall is also based on empirical correlations for flow through a vertical pipe [33] and is expressed as follows,

$$U_{f,mix} = U_{f,sat} \left\{ (1-x)^{0.01} \left[ (1-x)^{1.5} + 1.9x^{0.6} \left( \frac{\rho_{f,sat}}{\rho_{f,vap}} \right)^{0.35} \right]^{-2.2} + x^{0.01} \left[ \frac{U_{f,vap}}{U_{f,sat}} \left( 1 + 8(1-x)^{0.7} \left( \frac{\rho_{f,sat}}{\rho_{f,vap}} \right)^{0.67} \right) \right] \right\}^{-0.5} \quad (2.20)$$

In the Eq. (2.20),  $U_{f,sat}$  and  $U_{f,vap}$  are calculated using Eq. (2.18). The terms  $(1-x)^{0.01}$  and  $x^{0.01}$  ensure a value of unity for  $x = 0$  and a value of  $\frac{U_{f,vap}}{U_{f,sat}}$  for  $x = 1$ . Further discussion on this implementation will follow in section 2.7.

## 2.6 Sensitivity Analysis: FVM Discretization

To solve the governing equations (2.1-2.3), a finite volume modelling method is used. The FVM discretizes the heat exchanger uniformly and solves the governing equations in each cell. To access the accuracy and viability of the discretized evaporator model, a sensitivity analysis is performed discern the impact of discretization on model accuracy.

Figure 2.9 illustrates the impact of model discretization on the working fluid exit temperature and the phase change location predictions within the evaporator. Figure 2.9 is evaluated at the steady state condition stated in Table 2.1.

Gas flow [kg/h]	358.9
Gas inlet temperature [°C]	328.3
Gas outlet temperature [°C]	188.7
Ethanol flow [kg/h]	39.7
Ethanol inlet temperature [°C]	77.4
Ethanol inlet pressure [bar]	19.9
Ethanol outlet temperature [°C]	282.4

Table 2. 1. Steady state experimental conditions for evaluating FVM discretization.

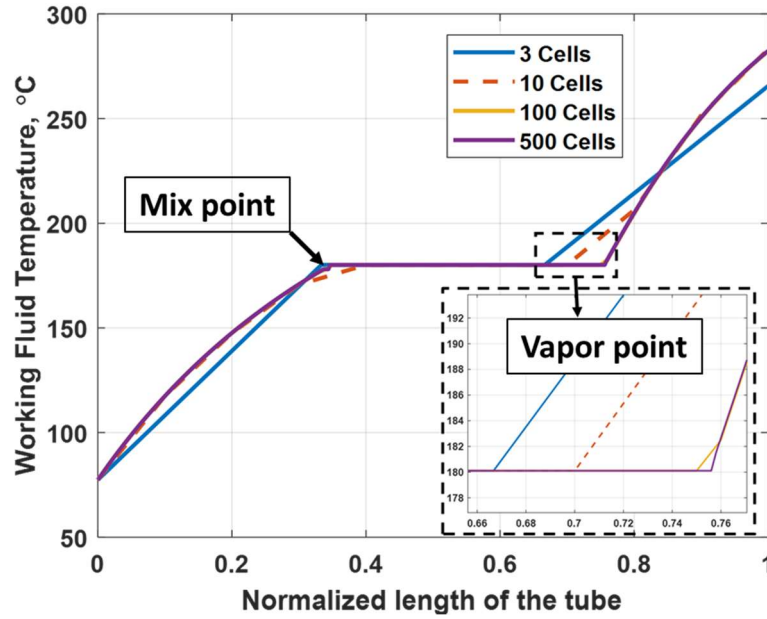


Figure 2. 9. Working Fluid temperature across the length of evaporator tube for different FVM discretization.

Table 2.2 provides a quantitative error summary at the different FVM discretizations represented in Figure 2.9. In Table 2.2, temperature error is calculated as the difference between simulated and experimental outlet temperatures. Phase length errors are calculated as a difference between the model prediction and the post processed thermal image data. Overall, while the model provides adequate working fluid and exhaust gas outlet temperature predictions with FVM discretizations as low as 10 cells, the trend in the phase length prediction error forces further FVM discretization.

	Evaporator outlet temperature error		Phase Length error	
Cells	Working Fluid	Exhaust gas	Mix point	Vapor point
	%	%	%	%
3	5.94	3.58	4.23	20.63
10	0.26	0.32	14.94	16.67
100	0.06	0.04	0.57	10.71
500	0.00	0.07	0.57	10.00

Table 2. 2. Error summary for different levels of discretization of the FVM model.

Figure 2.10 compares working fluid temperature predictions from the 500 cell FVM with the experimental thermal image data. With the 500 cell discretization, the FVM predicts the liquid transition to two-phase (mixing point) location with 0.57 % error, while the vapor point prediction is still subject to a 10% error. The vapor phase location error does not decrease substantially with further FVM discretization. Thus, there is room for FVM phase length prediction improvement, which will be discussed in detail in section 2.7.

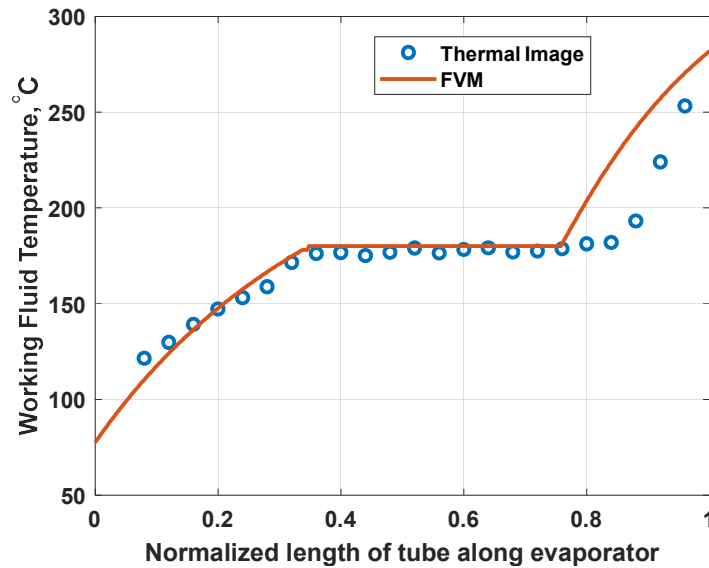


Figure 2. 10. Comparison of simulated working fluid temperature from FVM model 500 cells discretization and corresponding thermal image.

The FVM is utilized as a plant model for offline simulation and hence these models are not limited by their computation time. Since accuracy is prioritized in this study over computation time, the 500 cell FVM is utilized for the remainder of this work.

## 2.7 Enhancing FVM Phase Prediction Accuracy

Utilization of empirical correlations from literature with multipliers reflecting the loss of heat from the exhaust gases to the ambient within a FVM resulted in a best case 10% vapor phase length prediction error, regardless of further discretization. The empirical heat transfer coefficients in Eq. (2.18) and (2.20) may not directly apply to the heat exchanger geometry utilized herein, leading to inaccuracy of the correlations for specific scenarios. Thus, this section outlines additional calibration parameters necessary for enhanced FVM phase length prediction accuracy. The steady state point stated in Table 2.1 (and represented in Figure 2.10) is still utilized, and a sensitivity analysis is performed on the additional multipliers proposed to improve the vapor phase point detection without affecting the evaporator outlet temperatures.

Multipliers were introduced to the heat transfer coefficient equations (2.18, 2.20), and the resulting equations are stated below as (2.21) and (2.22),

$$U_{f,sat} = U_{liq} \frac{\left(\frac{\xi_{f,i}}{8}\right) Re_{f,i} Pr_{f,i}}{1 + 12.7 \sqrt{\frac{\xi_{f,i}}{8}} (Pr_{f,i}^{0.667} - 1)} (1 + (d/l)^{0.667}) \frac{k_{f,i}}{d_{f,i}} \quad (2.21)$$

$$U_{f,vap} = U_{vap} \frac{\left(\frac{\xi_{f,i}}{8}\right) Re_{f,i} Pr_{f,i}}{1 + 12.7 \sqrt{\frac{\xi_{f,i}}{8}} (Pr_{f,i}^{0.667} - 1)} (1 + (d/l)^{0.667}) \frac{k_{f,i}}{d_{f,i}} \quad (2.22)$$

$$U_{f,mix} = U_{f,sat} \left\{ (1-x)^{0.01} \left[ (1-x)^{1.5} + U_{mix,1} * 1.9x^{0.6} \left( \frac{\rho_{f,sat}}{\rho_{f,vap}} \right)^{0.35} \right]^{-2.2} + x^{0.01} \left[ \frac{U_{f,vap}}{U_{f,sat}} \left( 1 + U_{mix,2} * 8(1-x)^{0.7} \left( \frac{\rho_{f,sat}}{\rho_{f,vap}} \right)^{0.67} \right) \right]^{-2} \right\}^{-0.5} \quad (2.23)$$

Definitions of the newly introduced multipliers are as follows:  $U_{liq}$  is the tuning parameter added to the liquid phase heat transfer coefficient equation.  $U_{vap}$  is the tuning parameter added to the vapor phase heat transfer coefficient equation, and  $U_{mix1,2}$  are two heat transfer multipliers added to the mixed-phase flow inside the boiler. In the case of two phase flow,  $U_{mix1}$  and  $U_{mix2}$  are applied within Eq. 2.23 such that the terms  $(1 - x)^{0.01}$  and  $x^{0.01}$  still preserve heat transfer coefficient continuity.

### 2.7.1 Manual Parameter Tuning

With the insertion of additional tuning parameters, it was critical to understand their influence on prediction of the working fluid phase lengths and outlet temperature. Therefore, for the conditions listed in Table 1,  $m_U$  (the general heat transfer coefficient multiplier in Eq. (2.6)) and  $\eta_m$  (the efficiency multiplier in equation Eq. (2.12)) were identified first and held constant. Subsequently, each of the newly proposed multiplier [ $U_{liq}$ ,  $U_{mix,1}$ ,  $U_{vap}$ ,  $U_{mix,2}$ ] values were changed  $\pm 50\%$  as a sensitivity analysis, as shown in Table 2.3.

In Table 2.3, the rows with  $U=1$  represent the baseline FVM phase length and outlet temperature with just the general heat transfer coefficient and efficiency multipliers utilized. The percent change [ $C$ , %] in phase length and outlet temperatures between subsequent parameter perturbations and the baseline was then calculated as

$$C, \% = (baseline - multiplier_{perturbation}) * 100 / target \quad (2.24)$$

where the *baseline* is the parameter value obtained while holding the new heat transfer multiplier at unity,  $multiplier_{perturbation}$  is the parameter value obtained when the new multipliers are perturbed (as 0.5, 0.1, 1.0, 10), and *target* is the parameter value obtained from the thermal image data as shown in Figure 2.10.



		% CHANGE, C			
		Change in Phase Length		Change in Evaporator outlet temperature	
	multiplier value	Mix point	Vapor point	Working Fluid	Exhaust gas
$U_{vap}$	1	0.57	10.00	0.00	-0.02
	1.5	6.32	12.86	-1.59	0.78
	0.5	-17.8	2.38	5.35	-2.77
$U_{liq}$	1	0.57	10.00	0.00	-0.02
	1.5	-0.57	9.05	-0.99	0.30
	0.5	2.87	12.14	2.76	-1.13
$U_{mix,1}$	1	0.57	10.00	0.00	-0.02
	1.5	-0.57	10.71	-0.39	0.19
	0.5	2.30	7.86	1.24	-0.76
$U_{mix,2}$	1	0.57	10.00	0.00	-0.02
	1.5	0.57	10.00	-0.04	-0.07
	0.5	0.57	10.00	0.07	-0.12
	10	2.87	12.38	2.62	-1.08
	0.1	5.17	9.76	4.11	-1.93
$U_{mix,1} = U_{mix,2}$	1.5	-0.57	10.95	-0.39	0.19
	0.5	5.17	9.29	4.36	-2.08

Table 2. 3. Analysis the effects of additional multipliers on phase lengths for test conditions in Table 1. [Negative error means under-estimation and positive error is over-estimation]

Figures 2.11 – 2.15 display the results of Table 2.3. Figure 2.11 shows the effects of changing the  $U_{vap}$  value. As expected, when  $U_{vap}$  is increased by 50 % (=1.5), the heat transfer coefficients of both the pure vapor and the mixed phases increase, resulting in increased heat transfer between exhaust gas and working fluid in both regions of the evaporator. Thus, the vapor phase change occurs earlier than baseline. This increase in heat transfer also results in higher working fluid outlet temperature. Decreasing  $U_{vap}$  by 50% (=0.5) resulted in exactly the opposite behavior.

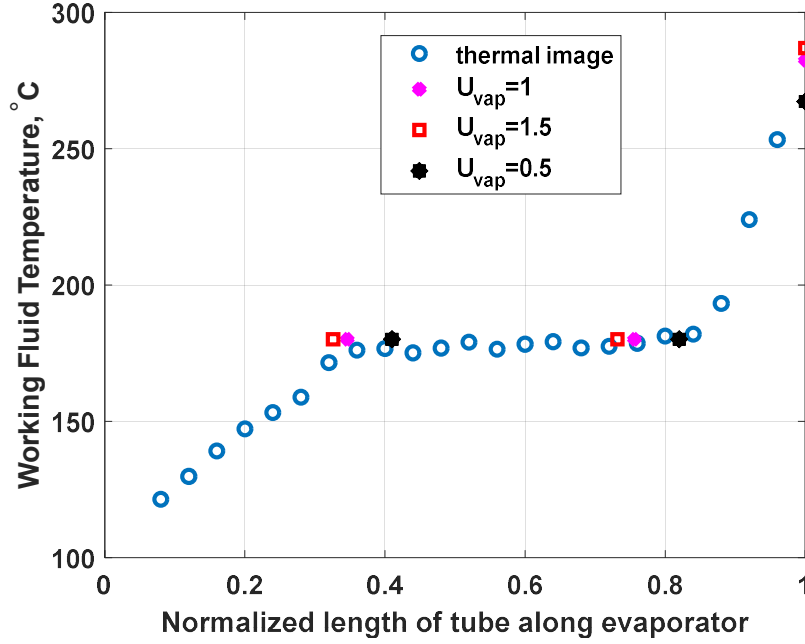


Figure 2. 11. Effects of varying  $U_{vap}$  values on phase lengths and outlet temperature.

Figure 2.12 illustrates the influence of  $U_{liq}$  on the working fluid phase lengths. The trend of  $U_{liq}$  is similar to that of  $U_{vap}$ . However, the magnitude of phase length change is reduced.  $U_{liq}$  indirectly influences  $U_{f,mix}$  by changing the value of  $U_{f,sat}$ . Since  $U_{f,sat}$  can be found in both the numerator and denominator of Eq. (2.23), the overall impact of  $U_{f,sat}$  on  $U_{f,mix}$  is minimal. A fifty percent increase in  $U_{liq}$  from 1.0 to 1.5 produces no discernable change in phase lengths from the baseline FVM. However, the trend can be verified by increasing  $U_{liq}$  by a factor of ten, which shows the phase changes occurring earlier and a higher outlet temperature. Predicted phase lengths displayed a weak inverse relationship with  $U_{liq}$  manipulation, requiring an order of magnitude parameter changes prior to phase length response.

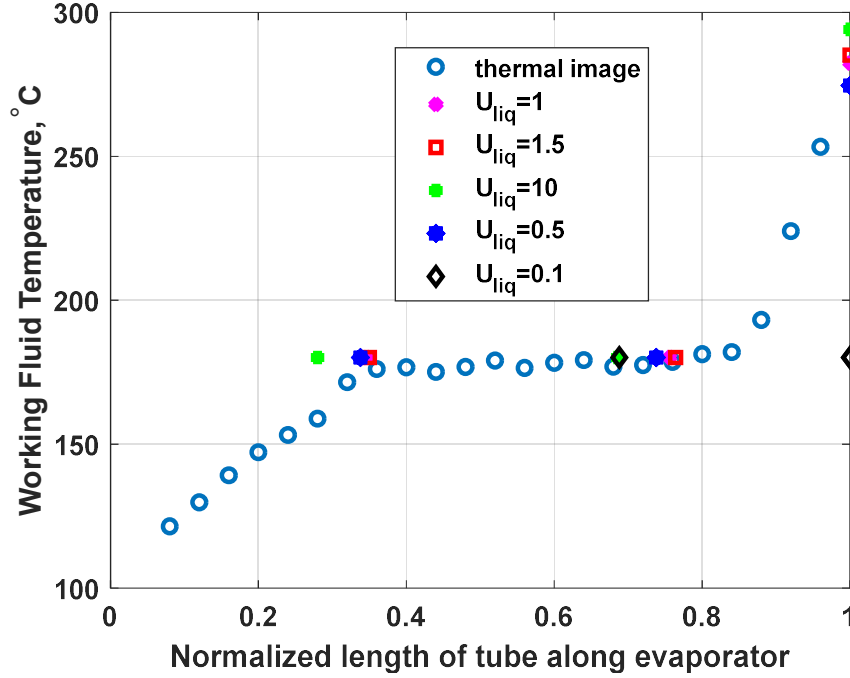


Figure 2. 12. Effects of varying  $U_{liq}$  values on phase lengths and outlet temperature.

The effects of  $U_{mix,1}$  and  $U_{mix,2}$  on working fluid temperature and heat transfer coefficient are shown in Figures 2.13 and 2.14, respectively. Comparing Figures 2.13 and 2.14 reveal the stronger influence of  $U_{mix,1}$  on the overall heat transfer coefficient,  $U_{f,mix}$  relative to  $U_{mix,2}$  in affecting the vapor point and mix point occurrence. The weaker influence of  $U_{mix,2}$  is the result of the normalization term  $\frac{U_{f,vap}}{U_{f,sat}}$  ahead of  $U_{mix,2}$ .

Figure 2.14 [2.14(b) is a zoomed in version of 2.14(a) for a clearer representation of the phase length changes] shows the heat transfer coefficient evolution along the evaporator tube length for various values of  $U_{mix,1}$  and  $U_{mix,2}$ . Increasing the  $U_{mix,1}$  by a factor of 10 affects the magnitude of overall heat transfer coefficient, but it does not influence the phase length significantly. Meanwhile, reducing the  $U_{mix,1}$  by a factor of 10 not only reduces the magnitude of the heat transfer coefficient but also increases the mix phase zone as seen from Figure 2.14 (a).

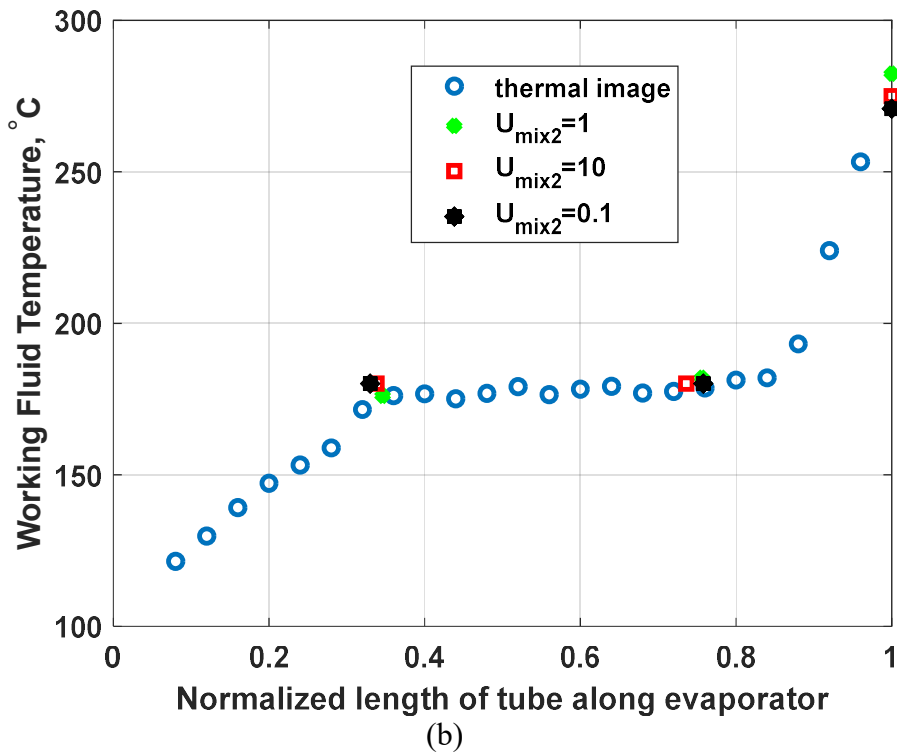
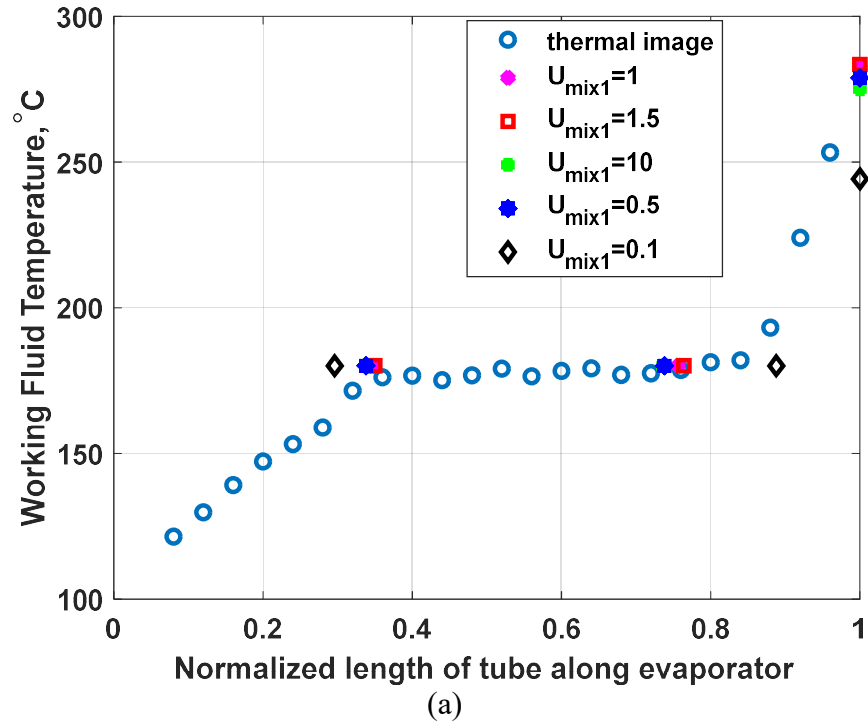
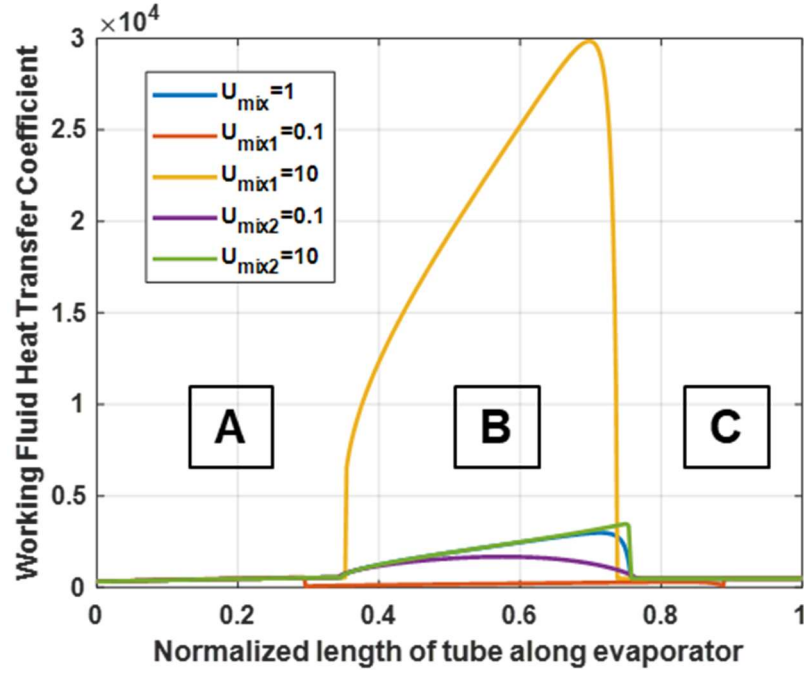
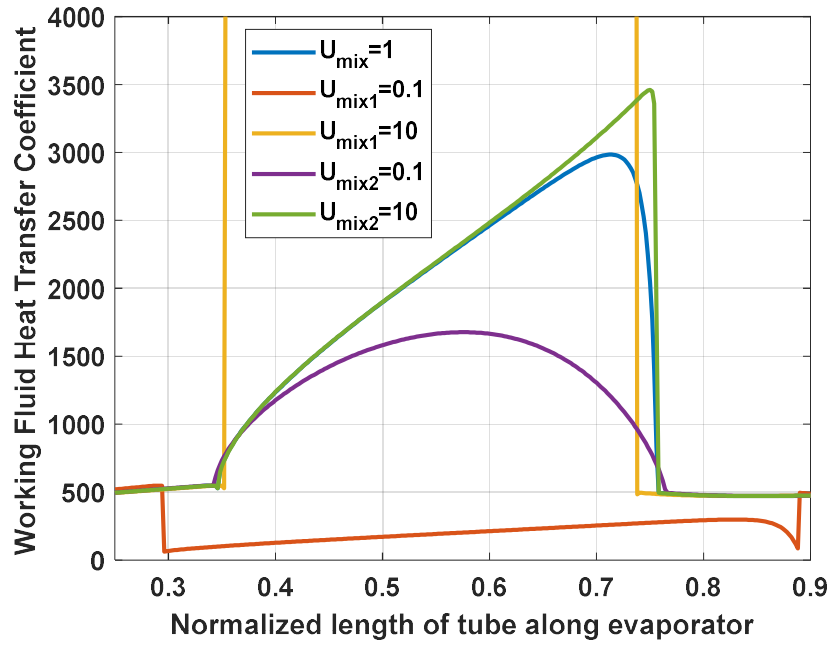


Figure 2. 13. Effects of varying  $U_{mix,1}$  and  $U_{mix,2}$  values on phase lengths and outlet temperature.



(a)



(b)

Figure 2. 14. Effects of varying  $U_{mix,1}$  and  $U_{mix,2}$  values on heat transfer coefficient.

Figure 2.14 (a) shows that, in the single phase convective heat transfer region A, the heat transfer coefficient is relatively constant despite changes to the  $U_{mix}$  multipliers. In the mixed phase

region B, as the quality of the fluid increases across the evaporator, the heat transfer coefficient increases rapidly. This is a physically correct phenomenon of bubble formation and transport resulting from higher fluid turbulence and mixing. The empirical correlations approximate the high heat transfer in the mix phase region caused by latent heat transfer from the formation of bubbles and the corresponding increase in turbulence. As the liquid film thickness reduces along the tube in the mixed phase forced convective region, the corresponding heat transfer coefficient increases with the vapor quality. Eventually, as liquid film thickness continues to decrease, it reduces the effect of forced convection and there is a rapid drop in heat transfer coefficient just before the onset of region C. Hence the heat transfer coefficient of the single phase vapor region C is always lower than the multiphase convection and evaporation heat transfer of region B. For reference, Appendix A [35], shows the typical flow patterns occurring inside the vertical tube heated uniformly over its length.

This sensitivity analysis of the newly proposed parameters provided useful insights regarding their relative impacts. These insights were utilized to configure the particle swarm optimization (PSO) bounds for the automated parameter identification discussed in the next section. For the PSO,  $U_{mix,2}$  was eliminated and only  $U_{mix,1}$  was utilized in the mix phase zone.

### *2.7.2 Particle Swarm Optimization Parameter Identification*

Once the relative impacts of each multiplier on the phase length and outlet temperature were understood, a PSO was utilized to identify the optimal values of all the model parameters for peak outlet temperature and vapor phase length accuracy. The five parameters that were simultaneously identified were  $[\eta_m, m_U, U_{liq}, U_{mix,1}, U_{vap}]$ .

The main criteria for modeling an evaporator is to accurately estimate the outlet temperatures and the PSO cost function weights were adjusted accordingly, i.e. higher weights were used for

temperature error compared to phase length error. The relative weights can be altered if the goals of future model implementations shift toward phase length prediction accuracy. The implemented PSO cost function is shown as Eq 2.25

$$J = 10 * \frac{(T_{f,sim} - T_{f,exp})^2}{200} + 10 * \frac{(T_{e,sim} - T_{e,ex})^2}{200} + \frac{(l_{M,sim} - l_{M,thermal})^2}{5000} + \frac{(l_{V,sim} - l_{V,thermal})^2}{5000} \quad (2.25)$$

where  $T_{f,i}$  denotes the working fluid outlet temperature,  $T_{e,i}$  is the exhaust gas outlet temperature,  $l_{M,si}$  is the mix phase point predicted by the FVM model,  $l_{M,therm}$  is the mix phase point determined from the thermal images,  $l_{V,sim}$  is the vapor point from FVM model, and  $l_{V,thermal}$  is the vapor point determined from the thermal images.

The cost function in Eq 2.25 involves two different variable types, working fluid temperatures and phase lengths, which have disparate orders of magnitude owing to their respective units. In order to compare these on equal footing, the temperature and phase length errors were normalized by 200 and 5000, respectively.

Table 2.4 shows the sensitivity study of different PSO targets for the operating conditions introduced in Figure 2.7 and Table 2.1. The varying PSO targets in Table 2.4 physically represent experimental uncertainty in  $l_{M,thermal}$  and  $l_{V,thermal}$ . As stated previously, the evaporator design relative to the thermal information available provides a level of uncertainty in the thermal imaging based phase length data on the order of twice the evaporator height. The objective behind this sensitivity study was to examine any improvement in phase length prediction while still maintaining the outlet temperature within acceptable margins of  $\pm 10^\circ\text{C}$ . In this study, importance was given to improving vapor phase length as compared to mix point. If the complete ORC system

is considered, the turbine is located after the evaporator, and safe operation of turbine requires confident prediction of the working fluid vapor quality exiting the evaporator.

Case#		Phase lengths		Evaporator Outlet Temperature (°C)	
		$l_M$	$l_V$	Working Fluid	Exhaust gas
	Thermal Image	0.36 +/- 0.04	0.84 +/-0.04	282.4	188.7
1	Baseline FVM results	0.348	0.758	281.7	188.7
	% Error in FVM results	-3.33	-9.76	-0.21	-0.37
2	PSO target	0.36	0.84	282.4	188.7
	% Error in FVM results	0	-2.62	-4.74	-2.8
3	PSO target	0.38	0.84	282.4	188.7
	% Error in FVM results	7.77	-2.85	-3.25	-2.06
4	PSO target	0.34	0.84	282.4	188.7
	% Error in FVM results	-3.89	-3.33	-4.5	-1.32
5	PSO target	0.36	0.8	282.4	188.7
	% Error in FVM results	<b>3.89</b>	<b>-5.95</b>	<b>-0.74</b>	<b>0.26</b>
6	PSO target	0.38	0.8	282.4	188.7
	% Error in FVM results	4.44	-6.43	-2.38	-0.28
7	PSO target	0.34	0.8	282.4	188.7
	% Error in FVM results	-9.44	-3.81	-3.72	-0.95

Table 2. 4. Summary of Sensitivity analysis of different PSO targets. Negative error in the above Table indicates under-estimation whereas positive error corresponds to over-estimation.

Case 5 provided the least error in the working fluid outlet temperature estimation while providing improvement in the vapor point prediction. Note that if the constraints for working fluid outlet temperature accuracy were relaxed, the parameters identified in Case 2 could provide addition phase length prediction accuracy. The PSO identified parameters from case 5 are compared with the baseline parameters in Table 2.5.



Parameters	Baseline	PSO
$m_U$	0.4517	0.4168
$\eta_m$	0.9646	0.9539
$U_{liq}$	1	0.9346
$U_{mix,1}$	1	2.7335
$U_{vap}$	1	2.6927

Table 2. 5. PSO identified variables for Case #5 in Table 2.4.

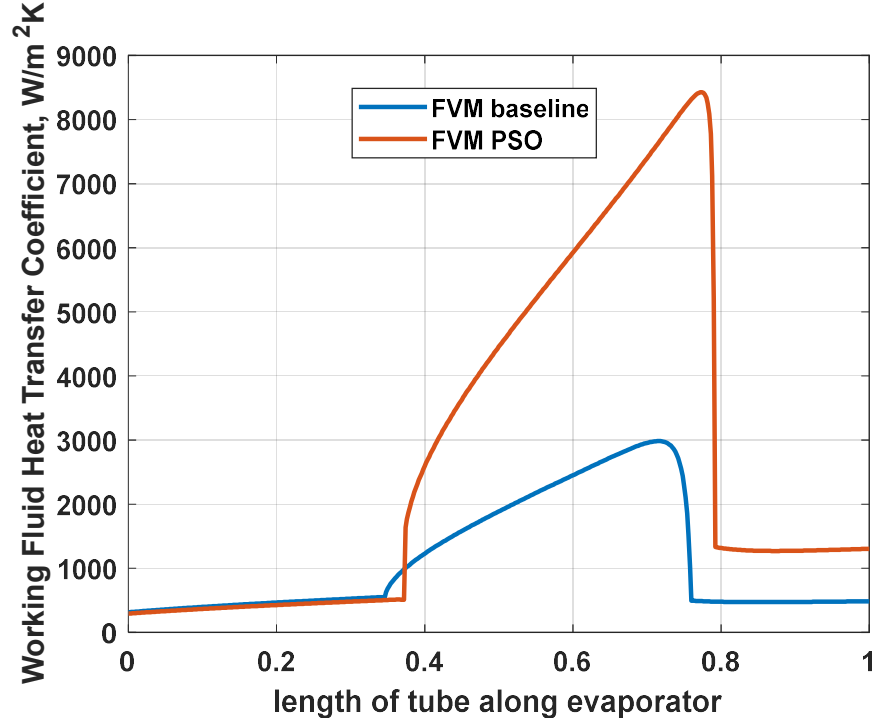


Figure 2. 15. Comparison of working fluid heat transfer coefficient from the FVM baseline model and the FVM with PSO identified values.

The effects of the multipliers  $U_{mix,1}$  and  $U_{vap}$  on the heat transfer coefficient is shown in Figure 2.15.  $U_{mix,1}$  and  $U_{vap}$  were increased by 2.8 and 2.7 times, respectively, leading to enhanced heat transfer prediction in the mixed-phase and vapor regions. The increase in heat transfer in each region is proportional to the increase in applied multiplier.

On interpreting PSO identified values, a value of 0.93 for  $U_{liq}$  does not substantially affect either the outlet temperature as observed during the sensitivity analysis shown in Figure 2.12. However, it can be concluded from Figures 2.11 and 2.13(a) that increasing  $U_{vap}$  and  $U_{mix,1}$

increases the evaporator outlet temperature, which in turn is counteracted by the lower overall heat transfer coefficient multiplier  $m_U$ . It can be also observed from Figure 2.13 (a) and later confirmed from Figure 2.14 that increasing  $U_{mix,1}$  also shifts the complete mix phase towards the evaporator outlet, the desired direction.

In order to match the evaporator outlet temperature and the working fluid phase lengths, the additional multipliers predict a higher heat transfer in the mixed phase region, as shown in Figure 2.15. This implies that the introduction of the generic empirical correlations (Eq. 2.12, 2.18, and 2.20) failed to capture the intensity of the real heat transfer phenomena within current the evaporator design. The introduction of additional multipliers compensates for lost physics in the mix phase region.

Figure 2.16 shows the working fluid temperature throughout the evaporator length for the Table 2.1 test conditions with both the baseline FVM and FVM utilizing the proposed PSO identified parameters. The FVM traces are plotted with the experimental thermal imaging data for comparison. The enhancement to FVM phase length prediction performance when utilizing the newly added PSO identified parameters is clear. While there is still room for further improvement, no further iterations were made within the scope of this study.

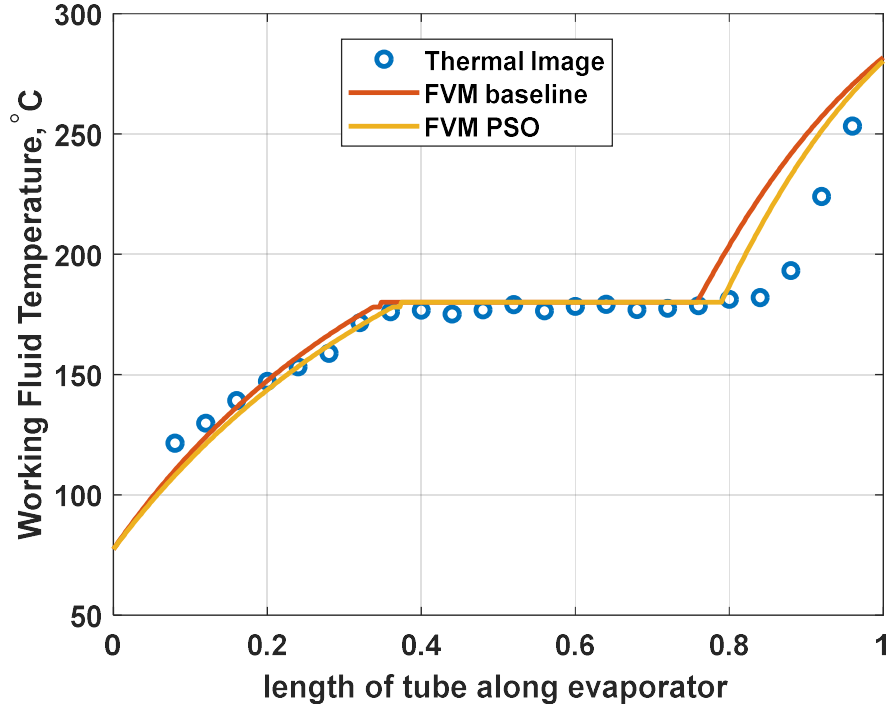


Figure 2. 16. Comparison of working fluid temperature along the length of the evaporator from the FVM baseline model and the FVM with PSO identified values.

## 2.8 Results

In this section, the performance of the enhanced PSO identified FVM, utilizing the parameters listed in Table 2.5, is evaluated relative to thermal imaging results collected from two different transient experimental runs. All of the experiments were performed on a thermal-flow bench, where the flow (hot gas) and temperature can be both controlled independently.

### 2.8.1 Transient Test Sequence #1

The first test sequence imitates a cold start. Figure 2.17 shows the test conditions for this experiment. Note that working fluid mass flow was initiated prior to the exhaust temperature rise. From 0s to 20s both the exhaust and working fluid are cold. Once the exhaust burner is initiated both the exhaust mass flow (360 kg/hr) and the exhaust temperature (327 °C) were kept constant for the remainder of the test. Conversely, working fluid pressure was kept constant at 20 bar and the outlet temperature was maintained at 280°C by altering the working fluid mass flow rate.

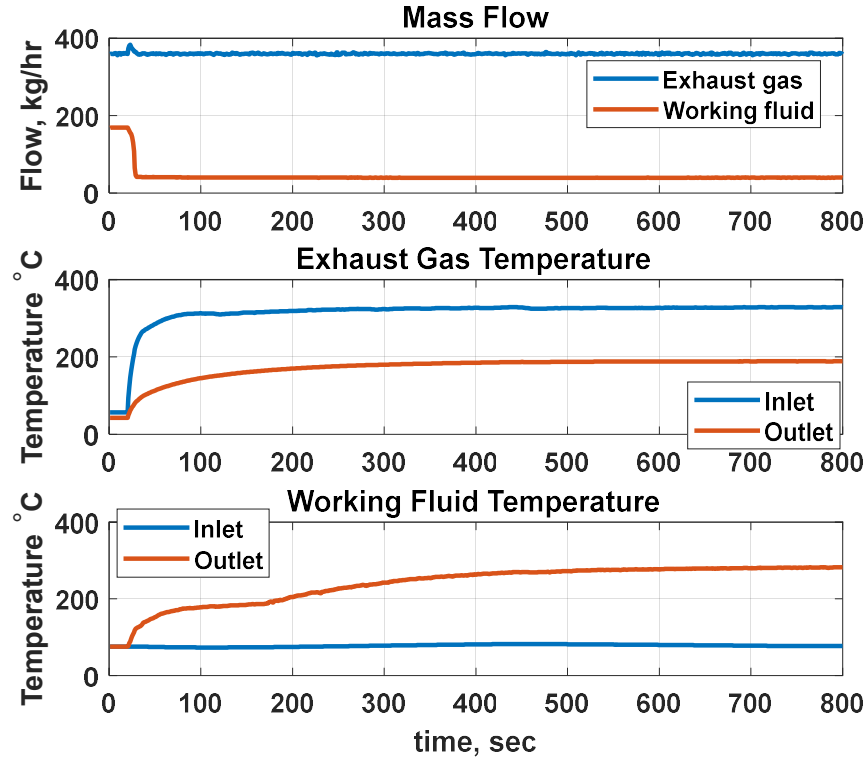


Figure 2. 17. Exhaust and Working Fluid conditions for Test 1.

Outputs of the enhanced FVM utilizing a 500 cell discretization are shown in Figure 2.18. Despite the initial offset in simulated exhaust outlet temperature (only observed in the cold region, which was outside the model calibration range), the FVM model precisely tracked the outlet temperatures. The mean error for the exhaust temperature was 1.45% whereas the working fluid the mean outlet temperature error was 1.68%. The model still exhibits a slight discrepancy at the onset of vapor phase, indicative of a slight disparity in wall thermal inertia.

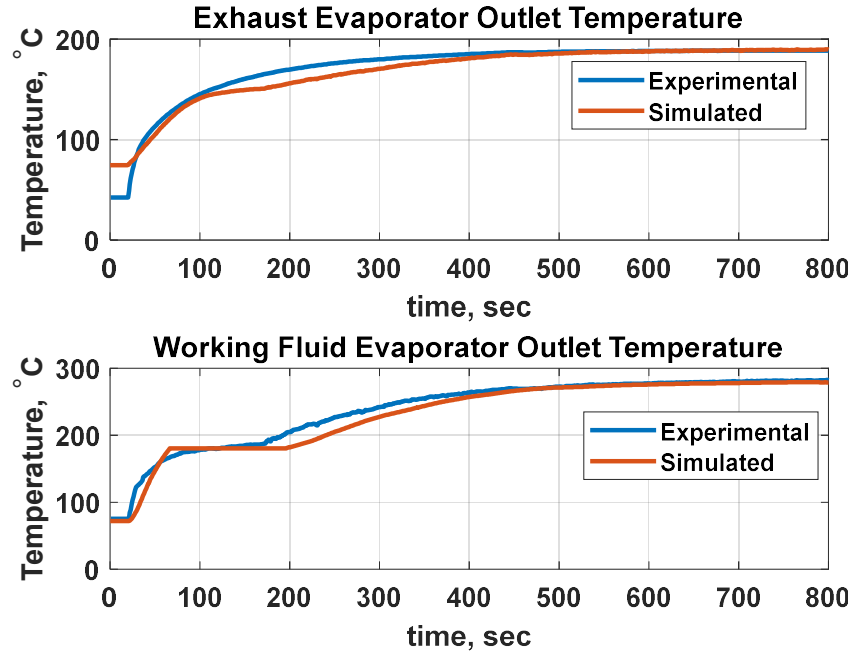


Figure 2. 18. Baseline FVM simulation results for the evaporator outlet temperatures for Test 1.

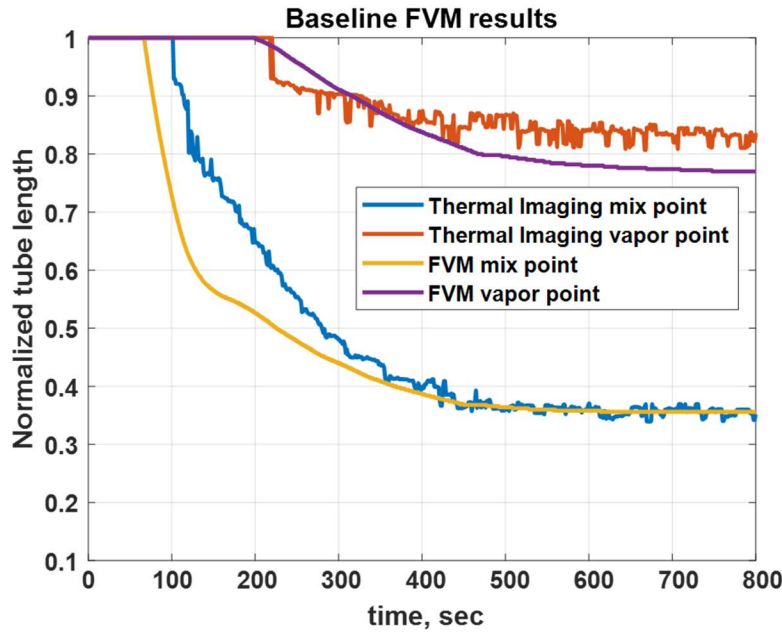


Figure 2. 19. Phase length comparison between the baseline FVM model and experimental thermal video for Test sequence #1.

Phase length predictions of the baseline FVM when utilizing test sequence #1 data as inputs are shown in Figure 2.19. Note that the high frequency error on the thermal imaging results is produced by the spatial resolution restrictions of utilizing the top evaporator surface for phase length prediction with an evaporator of this design. After 75s, as the working fluid temperature

increases, the FVM model prematurely predicts mix point. This may indicate a mismatch between the selected heat transfer correlations and the thermal behavior of the evaporator during harsh transients. However, as the system reaches equilibrium at the warmer working fluid temperature (after 300s), the mix phase length prediction accuracy increases, yet the length of the vapor phase is over-estimated (with respect to the evaporator outlet). These results correlate with Figure 2.10, which also displayed over-estimation of the vapor phase length relative to the thermal image results during another fully-warmed condition.

The next step was to evaluate the PSO identified values (Table 2.5) in the enhanced FVM over the complete transient. Application of additional multipliers showed a great improvement in the vapor phase length prediction with some penalty in mix phase length and working outlet temperature estimation [Figure 2.20]. Refer to Table 2.6 for the quantitative error comparison between base line and enhanced FVMs. Overall, the enhanced FVM exhibited a 43% improvement in mean vapor point prediction error.

	Baseline FVM		Calibrated FVM	
	Mix pt	Vapor pt	Mix pt	Vapor pt
Max % error	28	7.7	28.2	6.8
Mean % error	3.37	2.4	3.73	1.36

*Table 2. 6. Comparison of the phase length estimation between baseline FVM model and calibrated FVM model.*

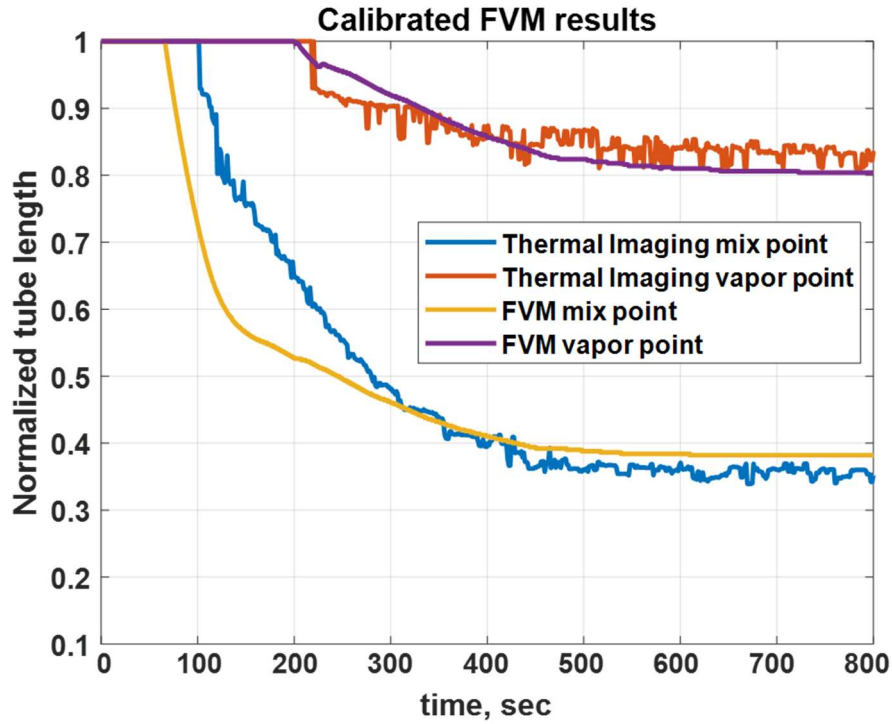


Figure 2. 20. Phase length comparison between the enhanced FVM and the experimental thermal video for Test #1.

Figure 2.21 displays the time varying phase length error comparisons between the baseline and enhanced FVMs. Both the mix point and vapor point predictions were shifted towards the evaporator outlet. Thus, the entire saturation zone was shifted towards the evaporator outlet. However, it is important to note that the change in vapor point position was greater than the change in mixing point prediction.

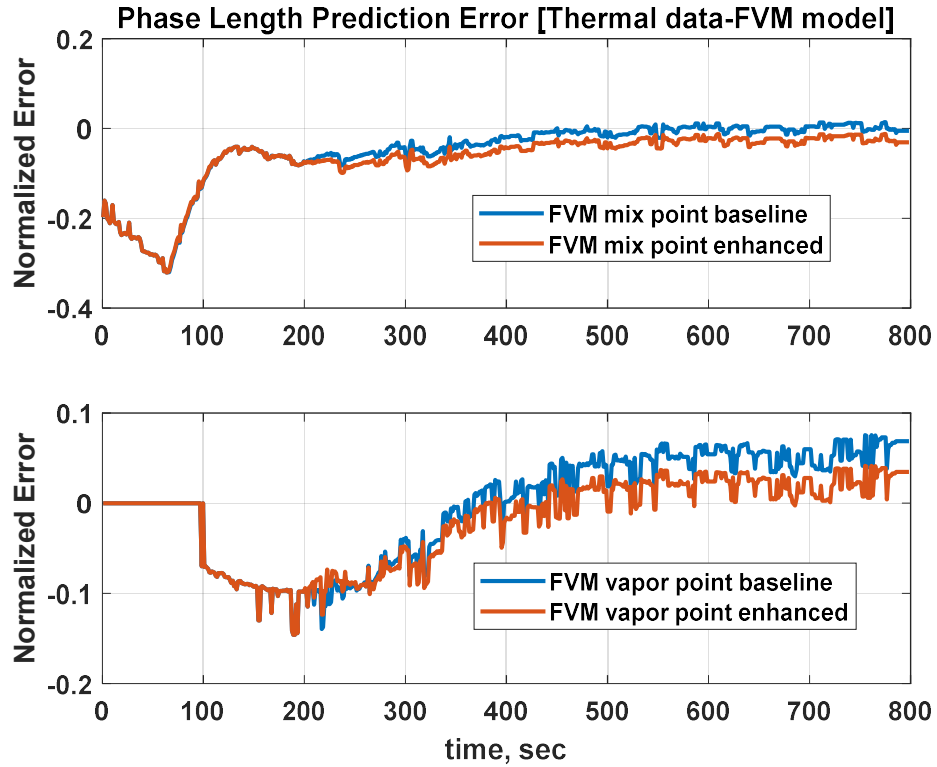


Figure 2. 21. Phase length error comparison for the baseline and enhanced FVMs relative to the thermal imaging results during transient Test 1.

Simulated exhaust and the working fluid outlet temperature error from the enhanced FVM remain representative of the experimental values, as shown in Figure 2.22. Although parameter identification for the enhanced FVM was limited to a single experimental condition, the new model accurately estimated the vapor phase length. Utilization of a broader data set during parameter identification will provide even better results during transient validation.



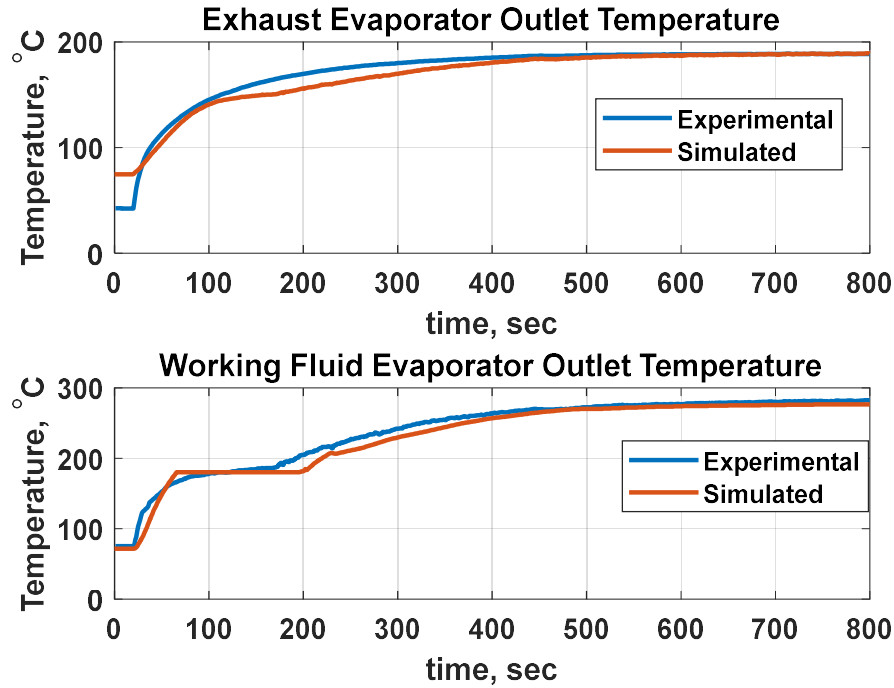


Figure 2. 22. Simulated working fluid and exhaust gas outlet temperature results from the enhanced FVM plotted relative to the experimental values for transient Test #1.

### 2.8.2 Transient Test Sequence #2

The second transient experiment maintained a constant ethanol flow rate (82 kg/hr) and exhaust temperature (350°C) while exhaust mass flow rate was ramped up and down, as shown in Figure 2.23. The phase length predictions of the enhanced FVM over transient test #2 are displayed in Figure 2.24. During portions of the test where all three working fluid phases are present within the evaporator (~100-500s), the enhanced FVM was able to predict the mix point accurately. However, during instances when the working fluid was saturated at the evaporator outlet, the model under predicted the mix phase length. This may be due to the utilization of turbulent equation (5.18), which increases the heat transfer coefficient and triggers the occurrence of mix phase prematurely. Note that the enhanced FVM was not calibrated with data displaying saturated working fluid outlet conditions.

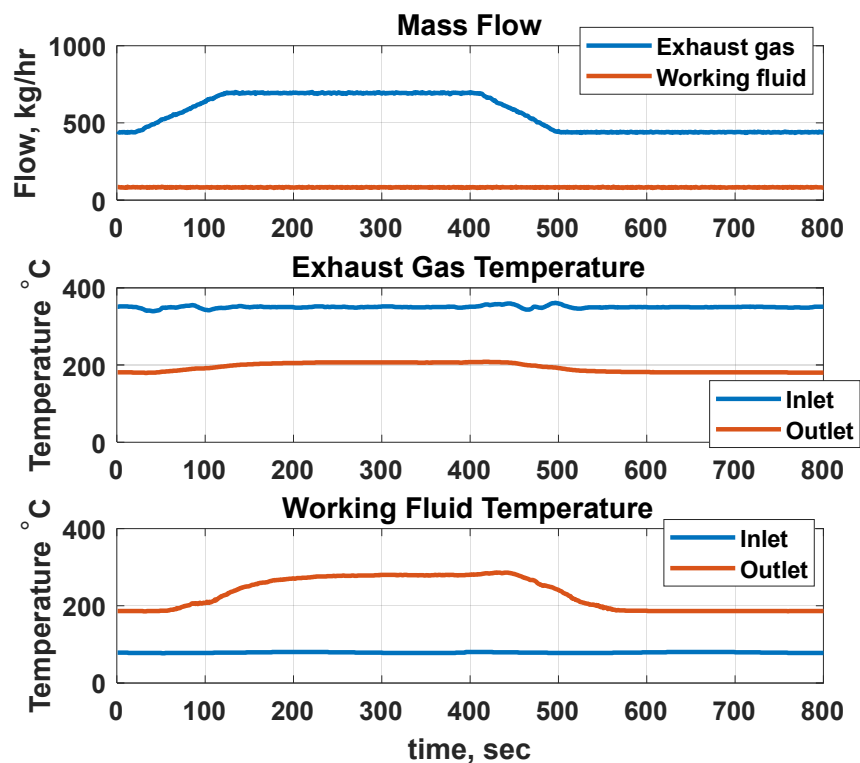


Figure 2. 23. Exhaust and Working Fluid conditions for Test 2.

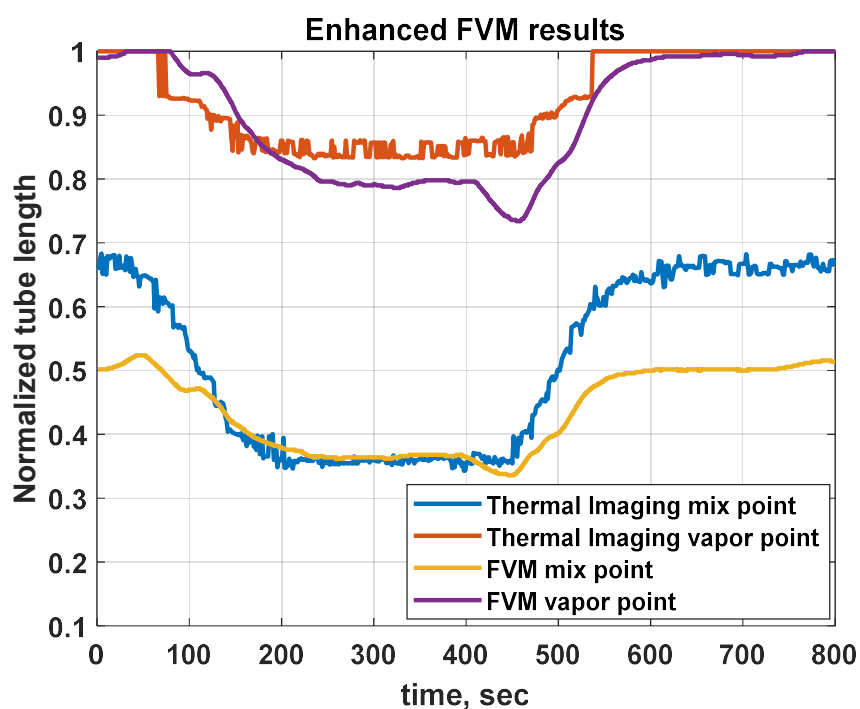


Figure 2. 24. Phase lengths comparison between the enhanced FVM model and the thermal videos for Transient Test #2.

The discrepancy of the vapor length during saturated outlet conditions can be improved by conducting parameter identification over a broader data set. No efforts were made in this work to improve the phase length predictions during saturated outlet conditions. Instead, focus was placed on accurate vapor phase length prediction. Even with the aforementioned shortcomings, the enhanced FVM still accurately predicts the working fluid and exhaust outlet temperatures in all the conditions, as shown in Figure 2.25, which is the most significant requirement of an evaporator model. The mean error for the entire transient test was 0.2% for the exhaust temperature and 1.55% for the working fluid.

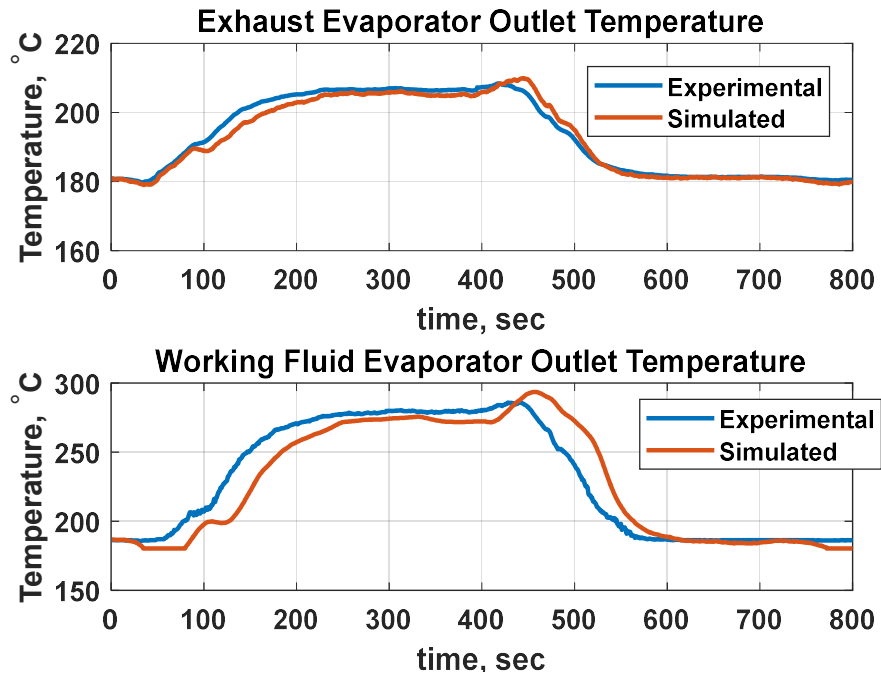


Figure 2. 25. Simulated working fluid and exhaust outlet temperatures using the enhanced FVM plotted relative to the experimental values during transient Test #2.

## 2.9 Conclusions

In this research work a high fidelity finite volume evaporator model was developed and validated for accurate estimation of working fluid phase lengths and evaporator outlet temperatures for a vertical tube cross-flow evaporator. A model discretization analysis showed that increased discretization increases the model's phase length prediction capability. A discretization of 10 cells

is enough to accurately model the evaporator outlet temperatures, while a 500 cell discretization provided the best phase length prediction capability.

A vertical tube type evaporator was experimentally tested on a flow bench. Thermal imaging data obtained from the corresponding transient tests was analyzed for experimental characterization of the working fluid phase lengths inside the evaporator. The baseline FVM estimation for mixed phase length is very accurate when all the three phases exist in the evaporator. However, the baseline FVM over-predicted the vapor phase region.

To improve the accuracy of the vapor phase length prediction, additional calibration parameters were included within the heat transfer coefficients for the mixed and vapor phases. A PSO was used to identify the optimal values for these multipliers utilizing the thermal imaging data. The enhanced FVM was then validated over two separate transient experimental data sets. The model adaptations included in the enhanced FVM resulted in a 43% improvement in vapor phase length prediction relative to the baseline FVM.

The current model formulation was not calibrated for instances where the working fluid is saturated at the evaporator outlet. The enhanced FVM still yielded accurate working fluid and exhaust gas outlet temperature results during these conditions, but the mixed phase length prediction accuracy suffered. Further calibration of the enhanced model will be necessary for accurate mixed phase length prediction during saturated working fluid outlet conditions.

Overall, a high fidelity FVM evaporator model was expanded to enhance the working fluid phase length predictions during transient operation. The methodology developed herein can bolster the evaporator design process and serve as basis for improving the moving boundary model for advanced ORC system control development.

## **CHAPTER 3. DYNAMIC CHARACTERIZATION OF EVAPORATOR**

### **3.1 Introduction**

This Chapter overviews the dynamics of the ORC system. First, the importance of characterizing the thermal inertia of the evaporator and working fluid properties is explained. Second, open loop analysis is performed on the ORC inputs and outputs that explains the plant dynamics and requirements of the controller design for an ORC-WHR system.

### **3.2 Background**

The thermal inertia of the evaporator affects the transient performance of ORC-WHR system. Under fluctuating loads, ORC system will respond in certain amount of time based on the thermal inertia. For optimal control of the set-point temperature or superheat tracking, the response time of the evaporators play a vital role [19, 24]. Evaporator dynamics is the slowest among other components of the ORC system, and therefore, the system inertia can be very well represented by the evaporator [36].

In this study, the ORC-WHR system contains two variants of the evaporator, the TP evaporator and the EGR evaporator. As the name suggests, the TP evaporator extracts heat from the TP exhaust and is located after the after-treatment system of the engine. Whereas the EGR evaporator extracts heat from the EGR exhaust flow and is located before the turbocharger and is in series with the EGR cooler to provide additional cooling. Because of their inherent locations both the evaporators are exposed to different dynamics of the exhaust heat source. Below is an example of a typical heat source for each evaporator.

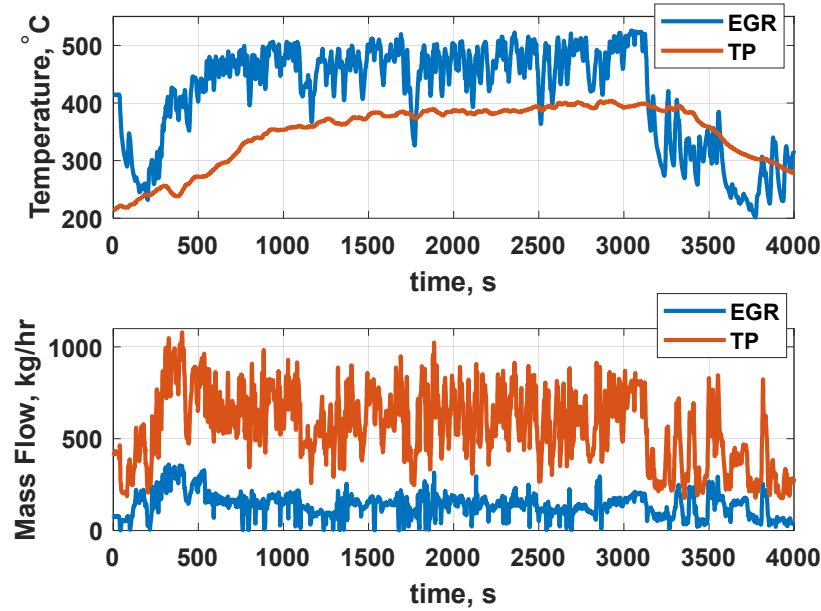


Figure 3. 1. Typical TP and EGR exhaust conditions

As shown in Figure 3.1, the frequency component of the exhaust mass flow dynamics for the both evaporators are similar, whereas the magnitude comparison shows that flow going through EGR evaporator is much less than the TP, because of which, in comparison to the TP evaporator, the EGR evaporators are much smaller in size. The exhaust temperature for EGR evaporator is as dynamic as the mass flow, but for the tailpipe evaporator the exhaust temperature is much dampened because of the after-treatment system. This shows that both the evaporators are exposed to different time-scale of exhaust conditions. Moreover the dynamic response of evaporator is a function of, 1) thermal inertia, 2) working fluid properties, 3) exhaust conditions and, 4) working fluid flow rate. A sensitivity study has being conducted for these parameters in the following sections.

### 3.3 Evaporator Thermal Inertia

The main aspects that affect the dynamic response of the evaporator can be grouped in the following areas: wall material, boundary conditions and geometry [36]. In this study, wall material and geometry of the evaporators are already fixed. The present work aims at investigating the

varying boundary conditions for two evaporators of different size, TP and EGR. Figure 3.2 shows the relative size comparison of the two evaporators under consideration.

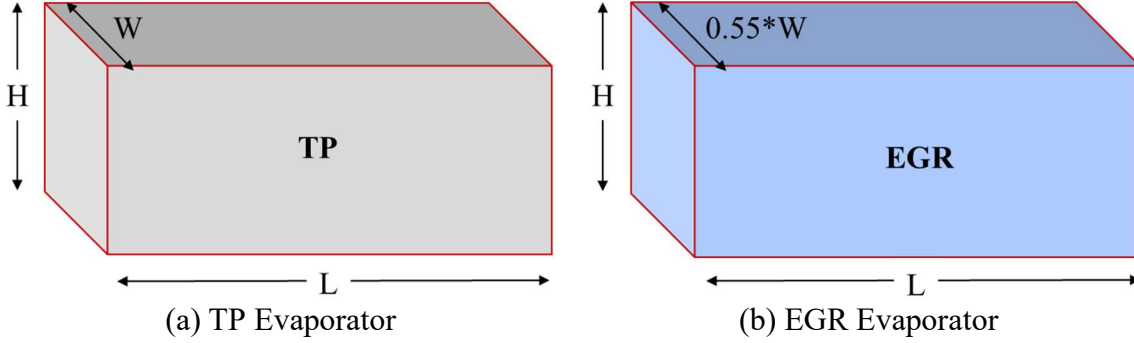


*Figure 3. 2. Evaporator size comparison*

Figure 3.2 (a) shows a single core TP evaporator. In this study, there are two single core TP evaporators connected in series. Therefore, effectively, the actual length of the TP evaporator is  $2*L$  whereas the width,  $W$  and height,  $H$  remains the same for this series connection. Figure 3.2 (b) shows the dimensions of the EGR evaporator with approximately half the width of the TP evaporator and is also half of the TP evaporator's effective length.

For this analysis, fluctuating loads with varying frequency are passed through the evaporator and the corresponding dynamic response of the evaporators is analyzed. This sinusoidal heat source can be viewed as alternating uphill and downhill road sections that can be encountered by the trucks in real-world operations. Understanding the effects of this fluctuating heat source is crucial for optimized ORC system operation. The analysis can aid as a tool for effective controller design for optimized dynamic operation in real world scenarios.

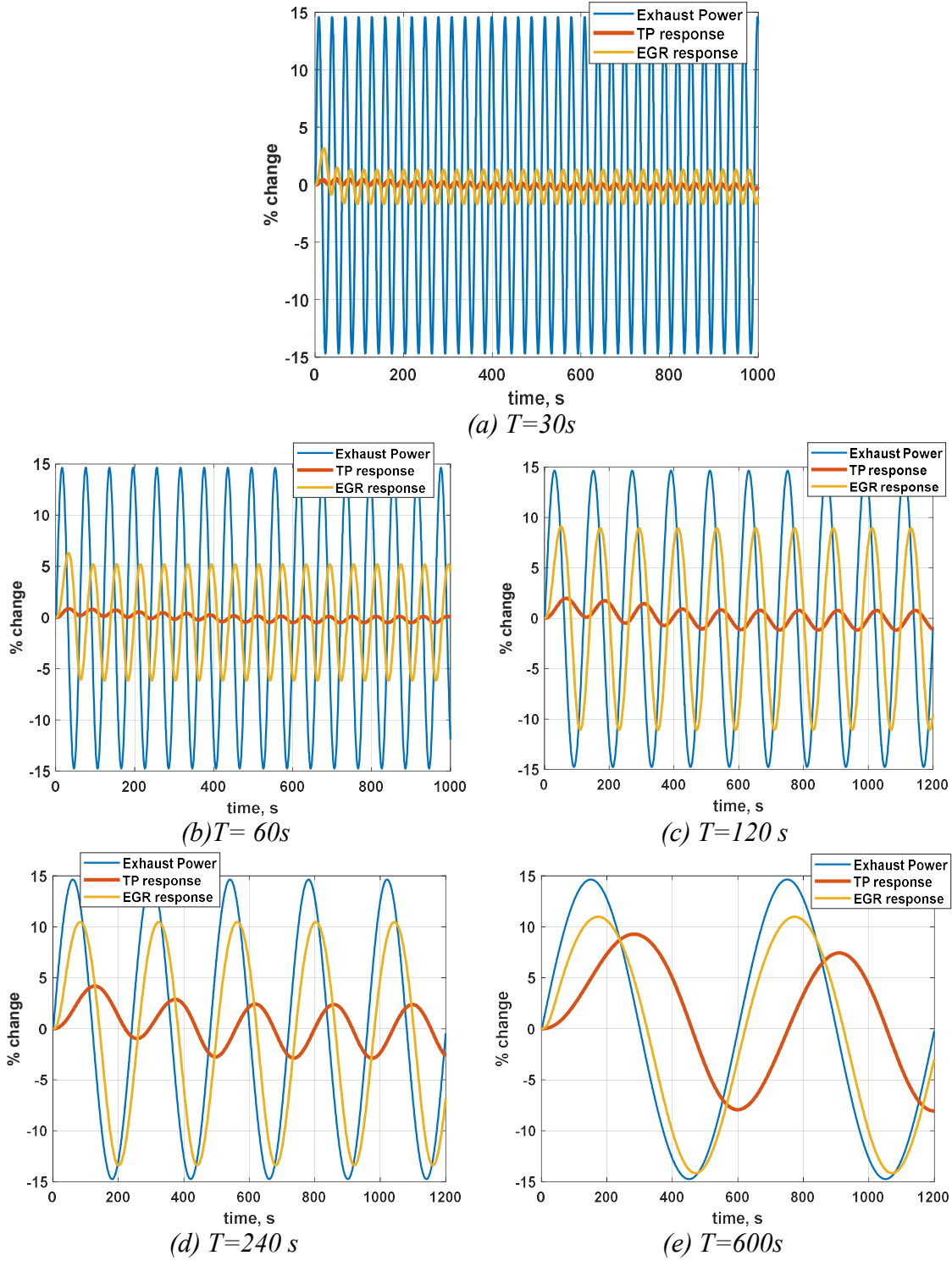


Figure 3.3. Thermal response of TP and EGR evaporators to sinusoidal exhaust conditions with varying time period,  $T$



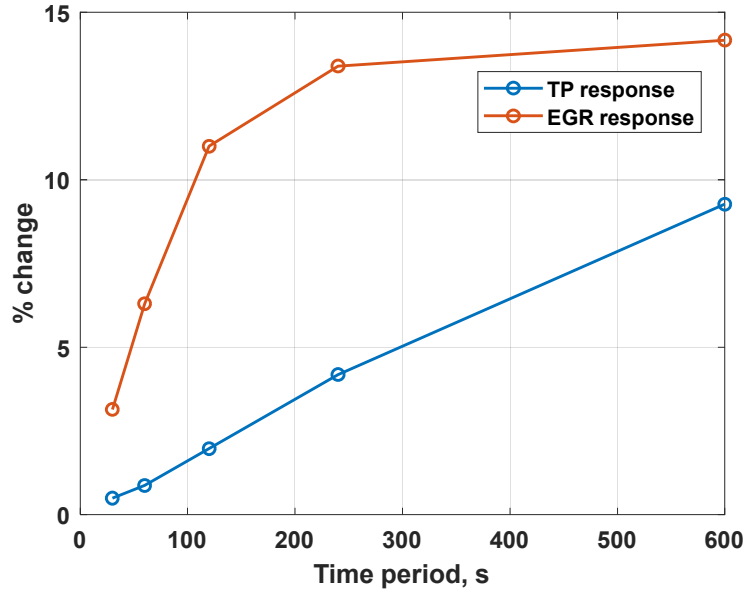


Figure 3. 4. Summary of thermal response of TP and EGR evaporator.

Figure 3.3 illustrates a systematic investigation of evaporator thermal response to different exhaust power frequencies. The thermal response of the evaporator is measured by the change in working fluid temperature at the evaporator outlet. The time-period of the sinusoidal exhaust power waveform is varied from 30 s - 600 s. For shorter time-periods, as seen from Figure 3.3 (a), the heat source fluctuations are filtered out by the thermal inertia of the evaporators. This is because heat transfer process inside the evaporator is a two-step phenomenon. In *Step 1*, heat energy flows from the exhaust gas to tube walls and depends on the tube material and thickness. These factors dictate the time necessary for the wall temperature respond. In *Step 2*, once the wall temperature responds, the heat then flows from the wall to the working fluid. Short period exhaust power fluctuations cannot fully influence the working as the power fluctuations cannot fully overcome the tube wall thermal inertia. Therefore, at high frequencies, only minimal changes in the working fluid temperature are observed. As the time-period of the heat signals is increased, the working fluid experiences increased fluctuation, as seen from Figure 3.3 (b) to 3.3 (e).

Relative to the TP evaporator, the dynamic response of the EGR evaporator is larger in magnitude and dynamically faster, i.e. the working fluid more closely tracks the exhaust power fluctuations. In other word, the smaller EGR evaporator dampens incoming exhaust power fluctuations less. Note that the higher thermal inertia TP evaporator produces a pronounced phase shift in the working fluid temperature response. This phase shift corresponds to the time taken by the thermal mass to complete the heat transfer process. Figure 3.4 summarizes the amplitude response to varying time-periods of the heat source for both the evaporators.

For optimal operation of the ORC system, the superheat tracking error should be as low as possible. If the temperature/enthalpy change of the working fluid at the outlet of the evaporator is to be remained unchecked than it's possible that the state of the working fluid will go below the saturation point inhibiting the turbine operation. In the following Chapters, it will be cleared on how to control this magnitude variation to the fluctuating heat source with a well-tuned model predictive control.

### 3.4 Working fluid properties

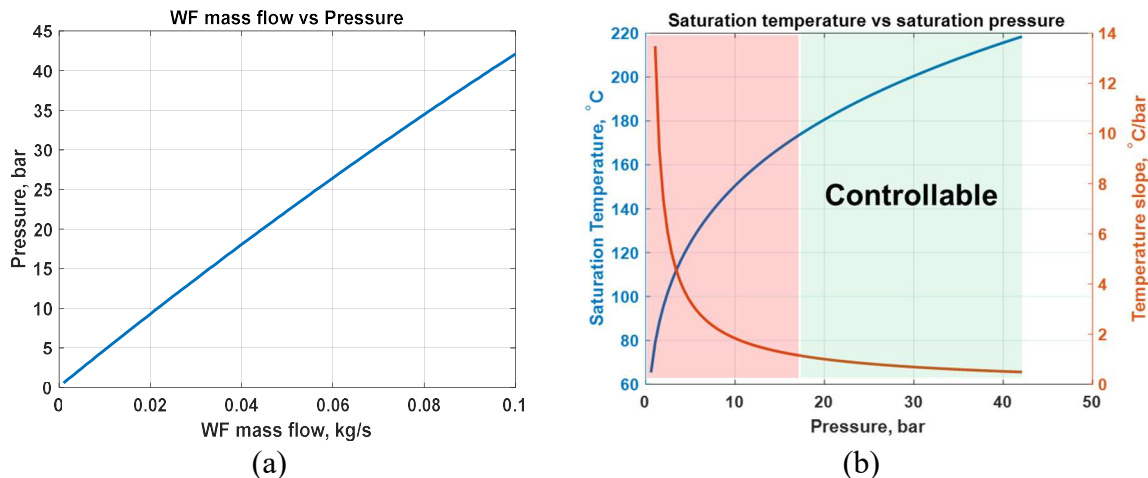


Figure 3. 5. (a) ORC system pressure as a linear function of Working fluid mass flow (b) Saturation temperature vs system pressure correlation for ethanol as working fluid

The correlation between working fluid flow rate and system pressure is a function of component characteristics i.e. the valves, turbine design, and tubing size in the ORC system. For a fixed valve position and a given turbine and tube design, the system pressure is a linear function of working fluid mass flow rate as seen in Figure 3.5(a). On the other hand, Figure 3.5(b) shows that increasing pressure causes the saturation temperature to increase non-linearly. This behavior is working fluid dependent. The curves shown in Figure 3.5(b) correspond to ethanol, the working fluid this study. A different working fluid will provide a different characteristic saturation temperature and system pressure correlation.

The slope of the saturation temperature shows that for pressures less than 18 bar, a small change in pressure will cause the saturation temperature to vary rapidly. This makes system operation difficult for pressures below 18 bar. Therefore, a control strategy should operate above pressures of 18 bar where slight pressure changes do not drastically affect the saturation temperature. Proper bounding of system operation will aid in maintaining superheat within acceptable limits.

### 3.5 ORC System dynamics evaluation

Once the evaporator dynamics are quantified, the next task would be to characterize the ORC systems inputs and outputs. For this analysis, an open loop evaporator and turbine model was created as shown in Figure 3.6. ORC system dynamics is a function of following parameters

1. Disturbances/Uncontrollable Inputs,  $\dot{m}_{exh}$ ,  $T_{exh}$
2. Control Input,  $\dot{m}_{wf}$

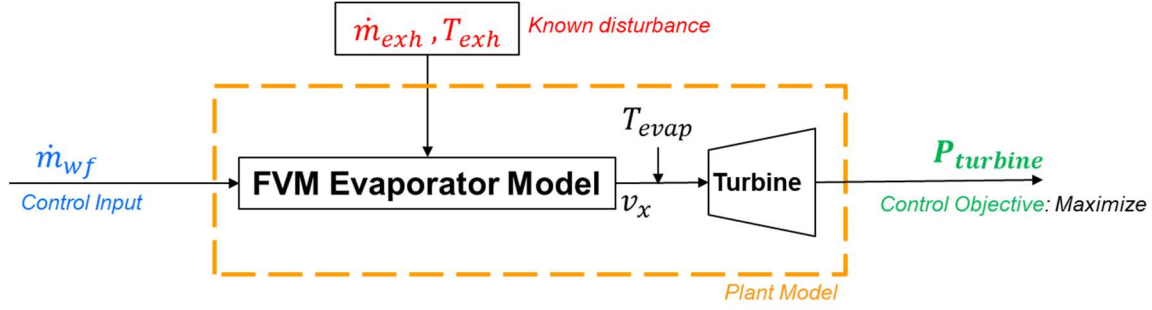


Figure 3. 6. Open loop plant model with inputs, outputs and control objective.

The input to the evaporator model is the working fluid mass flow rate which is controlled by the pump. The known disturbances that act on the evaporator model are the exhaust gas conditions,  $\dot{m}_{exh}$  and  $T_{exh}$ . The model output to be controlled is the working fluid temperature,  $T_{evap}$ /or superheat ( $\Delta H_{sh} = T_{evap} - T_{sat}$ ). The control objective is then to maximize the power production. In this simulation study, turbine is modelled as a map based function of evaporation pressure and saturation temperature. For a given ORC system operating with fixed valve position, evaporation pressure,  $P_{evap}$  is a linear function of working fluid.  $P_{evap}$  is estimated by formulating the mass flow and pressure relation from the experimental turbine map.

Table 3.1 summarizes the control objective of the ORC-WHR plant model. Superheating is required to be as low as possible that in order to increase the mass flow through turbine increasing its power output. From Figure 3.5 it can also be inferred that operating at higher pressure will lead to better controllability characteristic which will indirectly influence higher saturation temperature. For fixed valve openings and turbine speed, higher pressure can be achieved by increasing working fluid flow which in turn increase turbine power output. Ideally, condenser saturation temperature should be as low as possible to ensure complete cool-down of the working fluid before its circulated back in the evaporator. However, for on-board vehicle operation, cooling is limited to

radiator size. It is also dependent on ambient temperature and engine coolant temperature set-point. For simplicity, in this study the condenser saturation temperature was assumed to be constant.

Parameter	Objective	Constraints	
		Minimum	Maximum
Superheating, $\Delta H_{sh}$	Minimize	Safe turbine operation	WF deterioration limit
Evaporation Saturation temperature, $T_{sat}$	Maximize	None	None
Condenser saturation temperature, $T_{cond}$	Minimize	Ambient temperature	Available cooling capacity

Table 3. 1. Summary of the control objective of the ORC-WHR system.

### 3.5.1 Uncontrollable Inputs: Exhaust Conditions

For an automotive application, the ORC-WHR system is passive in nature. Therefore, the exhaust conditions are considered known (measured) disturbances or uncontrollable inputs. For this study, the engine conditions are changed in stepwise fashion while working fluid flow remains constant at  $\dot{m}_{wf} = 0.025$  kg/s. The test conditions are shown in Table 3.2 and the corresponding results are shown in Figure 3.7.

	Test A	Test B
$\dot{m}_{exh}$ , kg/s	0.3	0.3 - 0.35 - 0.4
$T_{exh}$ , °C	300 – 350 - 400	350

Table 3. 2. Exhaust conditions for sensitivity analysis on the uncontrollable inputs

Figure 3.7 (a), shows the exhaust temperature sensitivity. It can be observed that after the warmup (at 350 s), fixed magnitude (50 °C) step changes in exhaust temperature produce working fluid temperature changes of varying magnitude at the evaporator outlet. This non-constant behavior is a function of operating condition and results in a non-linear behavior.

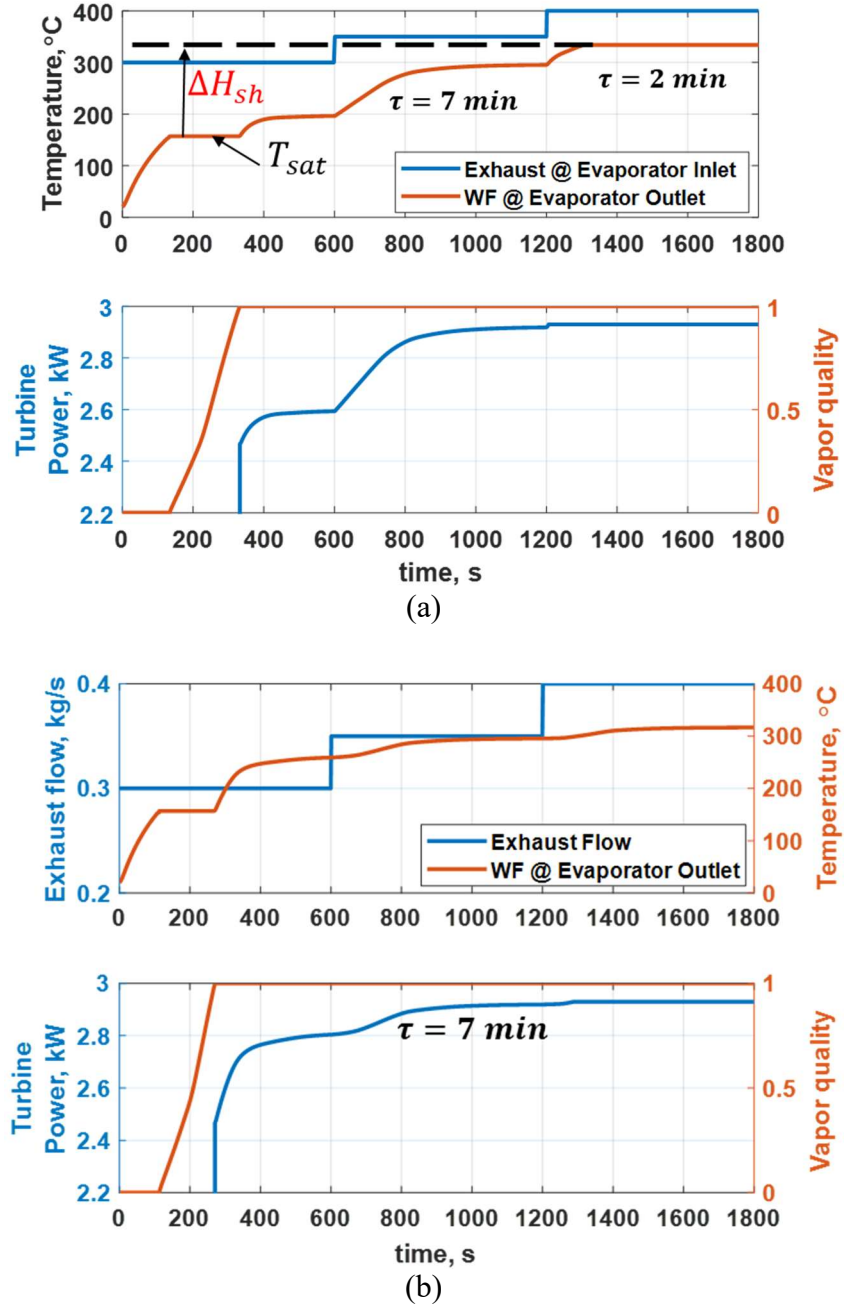


Figure 3. 7. Open loop simulation to characterize ORC system time constant for step changes in (a) exhaust mass flow (Test A) and (b) exhaust temperature (Test B). [ $\tau$  is the time constant for the response of the working fluid (WF) temperature].

It can be also inferred from the diminishing returns in turbine power with increased working fluid temperature that, at a constant working fluid flow there is an optimum working fluid

superheat level. Note that turbine power is a function of working fluid mass flow and the enthalpy change across the turbine as shown in equation (3.1) below,

$$P_{turbine} = \dot{m} * (h_{in} - h_{out}) \quad (3.1)$$

Where,  $\dot{m}$  is the working fluid mass flow rate,  $h_{in}$  is the enthalpy of the working fluid going into the turbine and  $h_{out}$  is the enthalpy of the working fluid out of the turbine.

As the temperature of the working fluid rises, its heat carrying capacity reduces saturating enthalpy,  $h_{in}$  and hence further increase in the exhaust power do not produce substantial gains in turbine power. Therefore  $P_{turbine}$  is nearly constant for the last step change as seen from Figure 3.7 (a).

Similarly, step changes in exhaust flow expose nonlinear evaporator dynamics, as shown in Figure 3.7 (b). However, the working fluid temperature changes are temporally damped. This can be attributed to the evaporator design and the reduced time available for heat transfer as the exhaust flow is increased. In summary, the evaporator non-linearity or the evaporator time constant is a function of engine operating conditions.

### 3.5.2 Controllable Inputs: Working fluid mass flow

The control input for an ORC system is the pump speed which manipulates the working fluid flow through the system to maintain vapor state at the evaporator outlet. In this case study, the working fluid flow is subjected to step changes to examine the system dynamics. The results of the working fluid step changes correlates with the experimental open loop analysis shown in chapter 1. For every step increase in working fluid flow rate the evaporator outlet temperature decreases. Correspondingly, the increase in working fluid mass flow increases the turbine power output, which correlates with Equation 3.1.

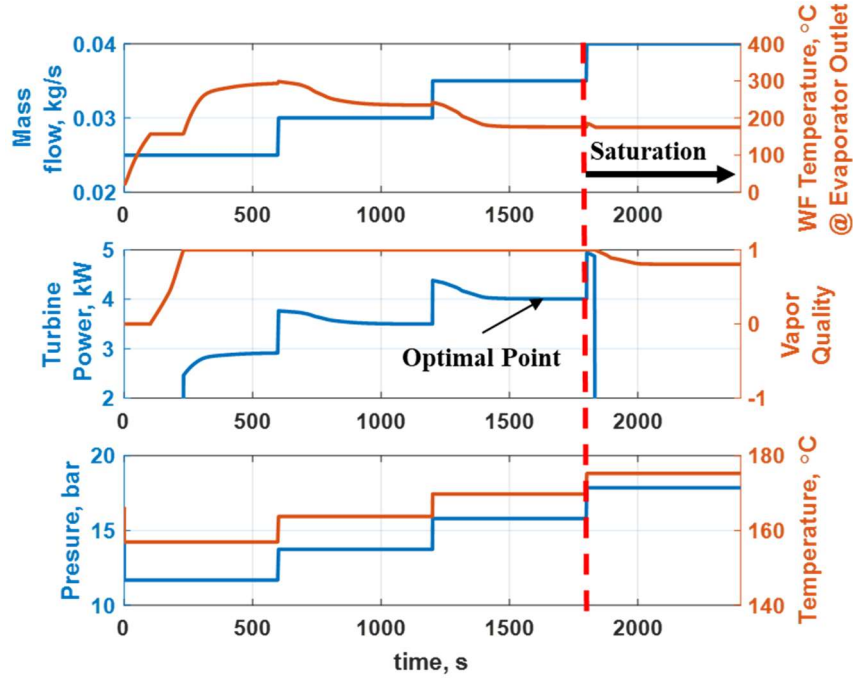


Figure 3. 8. Open loop simulation to characterize ORC system time constant for step changes in working fluid flow.

As shown in Figure 3.8, at 1800 sec (red dotted line) further step change in working fluid flow results in saturation. This loss in vapor quality arises for two reasons, 1) increasing the mass flow increases saturation pressure resulting in higher saturation temperature (bottom plot of Figure 3.8), reducing the superheat magnitude; 2) increasing the working fluid mass flow rate reduces the time available for heat transfer. Thus, for a given exhaust condition there is only one optimum working fluid flow for maximum turbine power generation and further increase of working fluid flow will lead to saturation, inhibiting turbine operation.

Another important conclusion is that the given ORC system is open loop stable since for a finite change in model inputs ( $\dot{m}_{exh}$ ,  $T_{ex}$ ,  $\dot{m}_{wf}$ ), the model outputs ( $T_{evap}$ ) reaches a stable steady state values, an important fact to be considered when designing an appropriate closed loop control law.



### 3.6 Conclusion

In this Chapter, an overview of different parameters influencing the dynamics of ORC-WHR system was presented. It was shown that the thermal inertia of the evaporator can be characterized by means of sinusoidal heat source with varying time period. Large size evaporators adds buffering towards high frequency heat source whereas the small size evaporators will respond faster to such high frequency inputs. This discrepancy in response time creates additional control challenge.

It was also demonstrated that for a fixed valve position, working fluid flow linearly changes the system pressure. This in turn proportionally changes the saturation temperature. It can be thus concluded that the ideal operating condition would be where a slight change in pressure would not affect saturation temperature substantially.

Open loop analysis showed the nonlinear nature of the evaporator, which is a function of engine operating conditions. The system time constant varies with exhaust mass flow, exhaust temperature and working fluid mass flow rate. From the open loop simulation it can be inferred that the ORC system is open loop stable. Since for each step changes in the input conditions the system arrived at a stable steady state condition. Further, it was also shown that for each exhaust condition only one optimal working fluid flow exist that provides the maximum turbine power output. An ideal controller will try to achieve this optimal point at transient engine conditions without inhibiting turbine operation nor violating the working fluid temperature constraints.

## CHAPTER 4. CONTROL DESIGN

### 4.1 Introduction

In this Chapter, a model predictive controller is designed for optimal control input based on the cost function objective. It is shown that for optimal turbine power generation low superheat is desired, consequently a superheat tracking controller is designed and the performance of designed controller is simulated over step inputs, drive cycle and a real-world sinusoidal time-varying exhaust conditions.

### 4.2 Background

Under highly fluctuating exhaust conditions, the main control requirement for uninterrupted turbine expander operation is to maintain the working fluid in a superheated state. Prior works have shown superior ORC-WHR performance through utilization of advanced control strategies like linear/nonlinear model predictive control [18-20, 23, 28], supervisory predictive control [21], and extended prediction self-adaptive control [22, 29] compared to traditional PID control.

Feru et al. [19] developed a switching MPC control strategy linearized over three operating conditions. Their proposed control strategy produced 3% increase in average output power relative to a classical PI strategy. In their simulation study, Esposito al. [20] proposed a nonlinear MPC where the receding horizon optimization problem was solved using a Particle Swarm Optimization (PSO) algorithm.

Hou et al. [21] developed a supervisory predictive control with constrained regulatory and economy targets within the optimization procedure. Their proposed strategy demonstrated less overshoot and shorter settling time under process and measurement disturbances in comparison to a traditional optimized PID control. Hernandez et al [22] evaluated the Extended Prediction Self-Adaptive Control (EPSAC) for multivariable systems (in this case, an ORC system). EPSAC used

input/output models for prediction, avoiding the need for state estimators. Simulation results suggested that for a steady heat source, PID control and EPSAC produced similar performance. However, for an unsteady heat source, EPSAC outperformed the PID controller in regulating the superheat temperature.

The next frontier is enhancing the MPC performance through a look-ahead approach.

#### *4.2.1 Look-ahead ORC control*

All of the aforementioned advanced control strategies have considered exhaust mass flow and temperature as disturbance inputs. The controller designs only consider the current exhaust condition for computing the control inputs for the complete prediction horizon. A key MPC capability is explicitly accounting for future disturbances, which automatically results in a feedforward control action [37]. Hence, better knowledge of disturbances over an extended horizon which will ensure more optimal control. Many research works [38-45] have exploited the potential of look-ahead control strategies utilizing future road topography and traffic conditions for fuel economy improvements.

Ganji, and Kouzani [38] have shown hybrid electric vehicle (HEV) performance and efficiency improvements by optimizing the split ratio between engine and battery power utilizing future road conditions. Gong et al. [39] evaluated trip based optimal power management of a plug-in hybrid electric vehicle (PHEV) using a Dynamic Programming (DP) algorithm with and without historic traffic data. In comparison to a simple trip model without historic data, simulation results showed an improvement of 18% in fuel economy due to usage of historic traffic data. Similar energy management optimal control strategies have been evaluated in a PHEV application by multiple researchers [40-42].

Huang and Bevly [43], investigated setting optimal vehicle speeds for a Heavy Duty truck to save fuel and trip time utilizing roadway geometry and a constrained Nonlinear Programming solver. Simulation results showed that the truck driving at optimal speed was able to significantly reduce fuel consumption with small penalty in travel time, when compared to constant speed cruise driving. Whereas Turri [44], exploited platooning and look-ahead control for reducing fuel consumption in a MPC framework. In this work, the optimal speed profile was established for the whole platoon rather than the first vehicle. This was done not only to reduce fuel consumption but to also maintain safe inter-vehicular distances. Additionally, Gáspár and Németh [45] evaluated a multi-objective optimization problem to predict an adaptive energy-efficient cruise control strategy based on the motion of surrounding vehicles. This paper proposed a look-ahead control utilizing several factors for calculating the optimal vehicle speed, such as: energy reduction, road slopes, traveling time, and speed limits.

#### *4.2.2 Opportunity and Uniqueness of the current work*

While many studies [18-20, 23, 28] have exploited the benefits of complex model based control strategies, all the published works utilize current exhaust conditions for prediction of the optimal control input. The approach pursued in this research study, differs in two ways.

**Firstly**, in this study, the potential benefits of look-ahead control strategy for an ORC system are investigated. It is assumed that the future vehicle speed can be predicted utilizing road topography and V2V connectivity [43-45]. This vehicle speed is then used to predict the engine speed and torque, culminating in the estimation of future exhaust conditions. The predicted exhaust conditions are then used to estimate the optimal control inputs in this MPC framework.

**Secondly**, MPC is inherently a state feedback control scheme using the current state and a system model for prediction. In literature, an extended Kalman filter (EKF) is widely used for

nonlinear state estimation by successive linearization of the nonlinear model at current predicted states [46]. In this study, the EKF is augmented with a disturbance model for offset free MPC tracking [47-48]. The performance of the proposed controller is then compared to the baseline NMPC control strategy, which lacks the look-ahead feature.

This Chapter is organized as follows: first the system under consideration is described, followed by control oriented modeling methodology. Then the control strategy is described with the augmented state estimator. The augmented state estimator performance is evaluated for disturbance rejection. Then MPC's preview capability is exploited in the next section. For the look-ahead control strategy, future exhaust conditions are considered when calculating the optimal control input for the given prediction horizon. Performance of the look ahead NMPC strategy is then evaluated relative to baseline NMPC performance for a step sequence exhaust conditions and for a drive cycle.

#### **4.3 Moving Boundary Control Model**

For control design, it is desired to have a low-computation model which is very efficient in capturing all the system dynamics of the evaporator. The finite volume model presented in Chapter 2 with 100 cells results in 300 states and is not acceptable for online implementation of MPC strategy. Therefore, in this section a reduced order control oriented model is presented.

During normal operation, i.e. typical heat exchange process, the evaporator contains working fluid in three different phases: liquid, mix and vapor. There are two boundaries that subdivide the evaporator into these three phases. The main function of the MBM is to track the length of each working fluid phase inside the evaporator by determining the boundary locations. Figure 4.1 illustrates the three working fluid phases for the MBM approach.

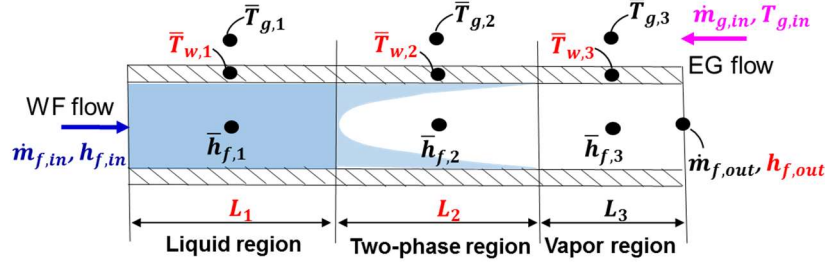


Figure 4. 1. Schematic representation of Moving Boundary Model used for evaporator control-oriented modeling (counter flow).

Applying energy balance equations to the working fluid and wall in each phase results in a 6-state MBM [28, 49]. Dynamics of the exhaust gases are neglected due to their fast transient characteristics. The derivation of the MBM assumes the existence of all three phases. The system of differential equations are summarized below:

#### Liquid region:

Phase length dynamics in the liquid phase ( $L_1$ ):

$$\begin{aligned} \bar{\rho}_{f,1} (\bar{h}_{f,1} - h_{f,l}) \frac{dL_1}{dt} = & \\ & - \frac{1}{2} AL_1 \left[ \bar{\rho}_{f,1} + \frac{\partial \bar{\rho}_{f,1}}{\partial h} (\bar{h}_{f,1} - h_{f,l}) \right] \frac{dh_{in}}{dt} + \\ & \dot{m}_{f,in} (h_{f,in} - h_{f,l}) + \pi d_{tube} L_1 U_{fw,1} (\bar{T}_{w,1} - \bar{T}_{f,1}) \end{aligned} \quad (4.1a)$$

Wall temperature dynamics ( $\bar{T}_{w,1}$ ):

$$\begin{aligned} Ac_p \rho_w L_1 \frac{d\bar{T}_{w,1}}{dt} + Ac_p \rho_w (\bar{T}_{w,1} - \bar{T}_{w,l}) \frac{dL_1}{dt} = & \\ & \pi d_{tube} L_1 U_{fw,1} (\bar{T}_{f,1} - \bar{T}_{w,1}) + \\ & \eta \pi d_{shelleqv} L_1 m_{HTC} U_{g,w} (\bar{T}_{TP,1} - \bar{T}_{w,1}) \end{aligned} \quad (4.1b)$$

#### Two-phase region:

Phase length dynamics for the mixed phase ( $L_2$ ):

$$\begin{aligned}
A \left[ \bar{\rho}_{f,1} (h_{f,l} - h_{f,g}) \right] \frac{dL_1}{dt} + A(1-\bar{\gamma}) \left[ \rho_{f,l} (h_{f,l} - h_{f,g}) \right] \frac{dL_2}{dt} = \\
-\frac{1}{2} AL_1 \frac{\partial \bar{\rho}_{f,1}}{\partial h} \frac{dh_{in}}{dt} (h_{f,l} - h_{f,g}) + \\
\dot{m}_{f,in} (h_{f,l} - h_{f,g}) + \\
\pi d_{tube} L_2 U_{fw,2} (\bar{T}_{w,2} - \bar{T}_{f,2})
\end{aligned} \tag{4.2a}$$

Wall temperature dynamics ( $\bar{T}_{w,2}$ ):

$$\begin{aligned}
Ac_p \rho_w L_2 \frac{d\bar{T}_{w,2}}{dt} + Ac_p \rho_w (\bar{T}_{w,l} - \bar{T}_{w,g}) \frac{dL_1}{dt} + \\
Ac_p \rho_w (\bar{T}_{w,2} - \bar{T}_{w,g}) \frac{dL_2}{dt} = \pi d_{tube} L_2 U_{fw,1} (T_{sat} - \bar{T}_{w,2}) + \\
\eta \pi d_{shelleqv} L_2 m_{HTC} U_{g,w} (\bar{T}_{TP,2} - \bar{T}_{w,2})
\end{aligned} \tag{4.2b}$$

**Vapor region:**

Evaporator outlet enthalpy dynamics ( $h_{f,out}$ ):

$$\begin{aligned}
A \left[ \bar{\rho}_{f,3} (h_{f,out} - \bar{h}_{f,3}) + \bar{\rho}_{f,1} (h_{f,g} - h_{f,out}) \right] \frac{dL_1}{dt} + \\
A \left[ \bar{\rho}_{f,3} (h_{f,out} - \bar{h}_{f,3}) + ((1-\bar{\gamma}) \rho_{f,l} + \bar{\gamma} \rho_{f,g}) (h_{f,g} - h_{f,out}) \right] \frac{dL_2}{dt} + \\
\frac{1}{2} AL_3 \left[ \bar{\rho}_{f,3} - \frac{\partial \bar{\rho}_{f,3}}{\partial h} (h_{f,out} - \bar{h}_{f,3}) \right] \frac{dh_{f,out}}{dt} = \\
-\frac{1}{2} AL_1 \left[ \frac{\partial \bar{\rho}_{f,1}}{\partial h} (h_{f,g} - h_{f,out}) \right] \frac{dh_{in}}{dt} + \\
\dot{m}_{f,in} (h_{f,g} - h_{f,out}) + \\
\pi d_{tube} L_3 U_{fw,3} (\bar{T}_{w,3} - \bar{T}_{f,3})
\end{aligned} \tag{4.3a}$$

Wall temperature dynamics ( $\bar{T}_{w,3}$ ):

$$\begin{aligned}
& Ac_p \rho_w L_3 \frac{\partial \bar{T}_{w,3}}{\partial t} + Ac_p \rho_w (\bar{T}_{w,g} - \bar{T}_{w,3}) \frac{dL_1}{dt} + \\
& Ac_p \rho_w (\bar{T}_{w,g} - \bar{T}_{w,3}) \frac{dL_2}{dt} = \\
& \pi d_{tube} L_3 U_{fw,3} (\bar{T}_{f,3} - \bar{T}_{w,3}) + \\
& \eta \pi d_{shelleqv} L_3 m_{HTC} U_{g,w} (\bar{T}_{TP,3} - \bar{T}_{w,3})
\end{aligned} \tag{4.3b}$$

where  $L_3 = L - (L_1 + L_2)$ ;  $d_{tube}$  and  $d_{shelleqv}$  are the heat exchanger hydraulic diameters on the working fluid and exhaust gas sides, respectively;  $m_{HTC}$  is a calibration parameter for the gas side heat transfer coefficient, and  $\eta$  is a calibration parameter accounting for heat loss between the exhaust gas and the ambient. The subscripts  $i = 1, 2, 3$  stand for liquid, two-phase, and vapor regions, respectively.

Assuming the exhaust gas temporal dynamics are ignored, the exhaust gas temperature evolution is predicted by the following algebraic equations:

$$\bar{T}_{g,1} = \frac{\left[ \pi d_{tube} L_1 U_{g,w} \bar{T}_{w,1} + \dot{m}_g C_{pg} \{ 2\bar{T}_{g,2} - 2\bar{T}_{g,3} + T_{g,in} \} \right]}{\dot{m}_g C_{pg} + \pi d_{tube} L_1 U_{g,w}} \tag{4.4a}$$

$$\bar{T}_{g,2} = \frac{\left[ \pi d_{tube} L_2 U_{g,w} \bar{T}_{w,2} + \dot{m}_g C_{pg} \{ 2\bar{T}_{g,3} - T_{g,in} \} \right]}{\dot{m}_g C_{pg} + \pi d_{tube} L_2 U_{g,w}} \tag{4.4b}$$

$$\bar{T}_{g,3} = \frac{\left[ \pi d_{tube} L_3 U_{g,w} \bar{T}_{w,3} + \dot{m}_g C_{pg} T_{g,in} \right]}{\dot{m}_g C_{pg} + \pi d_{tube} L_3 U_{g,w}} \tag{4.4c}$$

Thus in this model based design the evaporator system consists of 6 states,

$$[L_1, \bar{T}_{w,1}, L_2, \bar{T}_{w,2}, \bar{T}_{w,3}, h_{f,out}].$$



#### 4.4 NMPC Problem Formulation

For the ORC system under consideration, the primary control input is a working fluid mass flow, which is actuated via pump speed manipulation. The NMPC is then formulated as a finite horizon optimal control problem subject to system dynamics, as well as state and input constraints.

For control formulation, the resulting differential and algebraic equations in (4.1 – 4.4) can be written in the standard nonlinear state space form:

$$\begin{aligned}\dot{x} &= f(x, z, w, u) \\ z &= g(x, w)\end{aligned}\tag{4.5}$$

where  $x = [L_1, \bar{T}_{w,1}, L_2, \bar{T}_{w,2}, \bar{T}_{w,3}, h_{f,out}]^T$  is the dynamic state vector;  $z = [\bar{T}_{g,1}, \bar{T}_{g,2}, \bar{T}_{g,3}]^T$  is the algebraic state vector;  $u = \dot{m}_{f,in}$  is the control input;  $w = [\dot{m}_g, T_{g,in}]^T$  is an exogenous known disturbance vector (input from the engine to the ORC system) containing future predictions.

Then the NMPC formulation is written as follows:

$$\begin{aligned} & \min_{\bar{u}(\cdot), \bar{x}(\cdot)} J(\hat{x}(t), \bar{u}(\cdot)) \\ S.t. : & \left\{ \begin{array}{ll} \dot{\bar{x}}(\tau) = f(\bar{x}(\tau), \bar{z}(\tau), u(\tau), w(\tau)) \\ \bar{y}(\tau) = h(\bar{x}(\tau), \bar{z}(\tau), \bar{u}(\tau), w(\tau)) + d(t) \\ \bar{x}(t) = \hat{x}(t) \\ d(\tau) = d(t) & \forall \tau \in [t, t + T_p] \\ y^{lb} \leq \bar{y}(\tau) \leq y^{ub}, & \forall \tau \in [t, t + T_p] \\ u^{lb} \leq \bar{u}(\tau) \leq u^{ub}, & \forall \tau \in [t, t + T_c] \\ \bar{u}(\tau) = \bar{u}(t + T_c), & \forall \tau \in [t + T_c, t + T_p] \\ x^{lb} \leq \bar{x}(\tau) \leq x^{ub} \end{array} \right. \end{aligned}\tag{4.6}$$

where  $J: \mathbb{R}^n \times \mathbb{R}^m \rightarrow \mathbb{R}$  is the performance index for optimization;  $n$  and  $m$  are dimensions of state and input;  $T_p$  and  $T_c$  denote the prediction and control horizon, respectively with  $T_c \leq T_p$ , and  $d(t)$  is the disturbance state added for offset free tracking. The superscripts  $lb$  and  $ub$  indicate the lower and upper bounds of the constrained variables, respectively. The bar ( $\bar{\cdot}$ ) denotes predicted variables based on the control model using the estimated state feedback,  $\hat{x}(t)$ , and predicted input  $\bar{u}$ .

The NMPC computes the control input at each time instant  $t$  by minimizing the performance index,  $J$ .

$$J = \sum_{k=0}^{N-1} W_y(y(\tau) - y_r(\tau))^2 + W_{\Delta u} \Delta u^2 \quad (4.7)$$

where  $y_r$  is the reference working fluid superheat to be tracked by the output  $y$ , and  $\Delta u$  is rate of change of working fluid mass flow. Weights,  $W_y$  and  $W_{\Delta u}$  are tuned to attain the desired control performance.

#### 4.5.1 ACADO Implementation

For the current NMPC simulation study, ACADO [50-52] an open-source software environment, has been used to implement the proposed controller scheme. ACADO implements real-time iteration scheme to solve optimal control problems. The ACADO toolkit is equipped with a collection of algorithms for solving various automatic control and dynamic optimization problems. ACADO is also capable of automatically generating a highly efficient *s-function* code for fast MPC applications using MATLAB/Simulink while performing a robust optimization for medium to large scale non-linear problems.

## 4.6 Disturbance Model and Observer Design

NMPC is inherently a state-feedback algorithm and assumes the availability of full-state information through measurement or estimation at the initial condition. In order to achieve offset-free tracking in this formulation, the nominal system dynamics (Equation 4.5) are augmented with additional integrating states or disturbances [53-54]. The general augmented linearized system is given as follows:

$$\begin{aligned} x_a(t+1) &= A_a x_a(t) + B_a \bar{u}(t) \\ y(t) &= C_a x_a(t) \end{aligned} \quad (4.8)$$

In which:

$x_a = \begin{bmatrix} x \\ d \end{bmatrix}$  is the augmented state matrix, where  $d$  is the disturbance and is assumed to stay constant over the prediction horizon.

$$A_a = \begin{bmatrix} A & B_d \\ 0 & I \end{bmatrix}, B_a = \begin{bmatrix} B \\ 0 \end{bmatrix}, C_a = [C \ C_d]$$

In this study, the values  $B_d = 0$  and  $C_d = 1$  are utilized making the augmented system as an “output integrator” [55]. The augmented states in equation (4.8) is estimated at each time step given the output measurement by means of a posteriori observer, containing a prediction phase and correction phase.

*Prediction Phase:* For forward prediction of the state trajectories  $\hat{x}^0(t+1)$ , an implicit numerical integration method called Rosenbrock-Wanner (ROW) is used.

$$\hat{x}^0(t+1) = A\hat{x}(t) + B\bar{u}(t) \quad (4.9)$$

For the ORC system dynamics as stated in equations (4.1 – 4.4), a two-stage ROW method described below [28] is implemented to estimate  $\hat{x}^0(t+1)$ :

$$x_{n+1} = x_n + dt \sum_{i=1}^2 b_i k_i$$

$$W_n k_i = f \left( x_n + dt \sum_{j=1}^{i-1} a_{ij} k_j \right) + dt J_n \sum_{j=1}^{i-1} d_{ij} k_j, \quad i = 1, 2 \quad (4.10)$$

$$W_n = I - dt d_{ii} J_n, \quad J_n = \frac{\partial f(x_n)}{\partial x}$$

The coefficients for the two-stage ROM method are:  $a_{21} = \frac{2}{3}, d_{11} = 1 + \frac{1}{\sqrt{2}}, d_{21} = -\frac{4}{3}, b_1 = \frac{1}{4}$  &  $b_2 = 3/4$ . For detailed derivation of the ROM method, one can refer to [56].

*Correction Phase:* In the correction stage, an Extended Kalman Filter (EKF) is utilized,

$$\hat{x}_a(t+1) = \hat{x}^0(t+1) + K_a[y(t+1) - \bar{y}^0(t+1)] \quad (4.11)$$

where  $K_a = \begin{bmatrix} K_x \\ K_d \end{bmatrix}$  is the augmented state matrix,  $K_x$  is the Kalman gain, and  $K_d$  is the disturbance gain that is tuned to achieve the required performance for overshoot and rise time for a unit step change.

Note that the augmented state formulation (4.8) is only used to obtain and define the states  $(\hat{x}, \hat{d})$  but is not used in the NMPC formulation (4.5).

## 4.7 Simulation Results

In this section simulation results are presented to demonstrate the performance of the proposed controller over step inputs in exhaust conditions and for a drive cycle. For this simulation study, all the working fluid flow is passed through turbine by keeping the bypass valve closed and turbine valve completely opened. The evaporator pressure is then a function of working fluid flow rate, more flow will result in higher evaporation pressure and vice-versa.

The NMPC designed in this section utilizes 100 prediction steps ( $N$ ) with model time step ( $T_s$ ) of 0.6 seconds, making the prediction horizon ( $H_p$ ) 60 seconds. Note that in simulation studies prediction horizon of less than 60 sec resulted in short-sightedness for the MPC to solve the optimal problem. The control horizon is set equal to the prediction horizon.

#### 4.7.1 NMPC Cost function formulation

The main objective of the ORC-WHR system is to recover as much heat energy as possible through the turbine shaft. For this case, the NMPC cost function was formulated to track a constant fraction of exhaust power to be recoverable. A quadratic cost function was formulated as stated below,

$$J = W_P \frac{(P_{turb,ref} - P_{turb})^2}{P_{max}} + W_{du} \frac{(du_{ref} - d_{pump})^2}{du_{max}} \quad (4.12)$$

A superheat constraint is imposed,  $30 < SH < 150$  and the other parameters are as follows

$$P_{max} = 100 \text{ kW}, P_{ref} = 15 \text{ kW}, du_{max} = 0.0025, du_{ref} = 0, W_P = 1, W_{du} = 5.$$

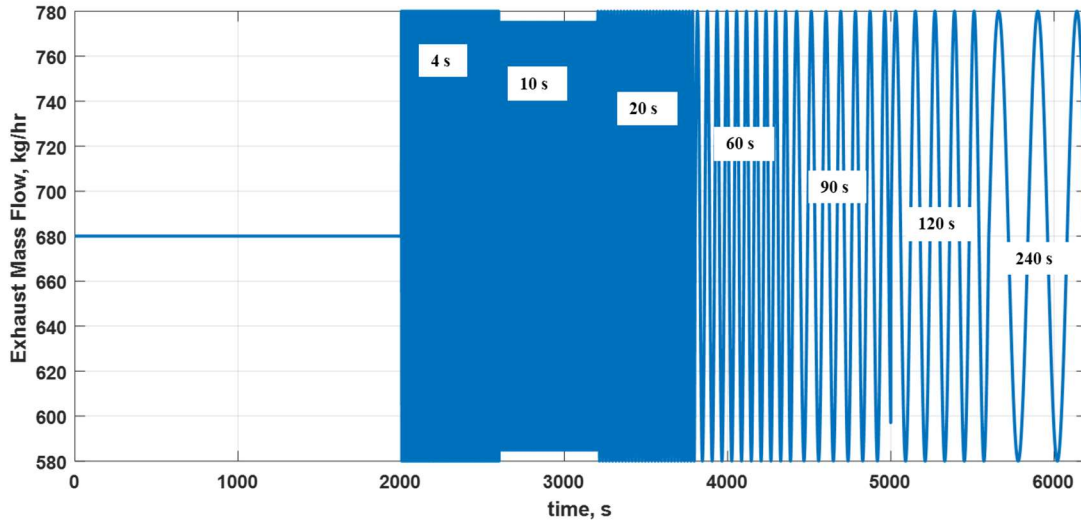


Figure 4. 2. Generated sinusoidal exhaust mass flow with varying time periods to test the NMPC controller

To test the controller and the cost function, a sinusoidal exhaust condition was generated as shown in Figure 4.2. In a transient condition, exhaust mass flow changes frequently with RPM and requested torque, whereas the change in exhaust temperature is very slow due to the thermal inertia of the after-treatment system. Hence in the generated sinusoidal heat source signal, exhaust temperature was kept constant and the time period of the mass flow was varied from 4s to 240 s.

The performance of the formulated MPC with objective function for maximizing the turbine power is shown in Figure 4.3. It can be seen from Figure 4.3 that during the initialization section from 0 to 2000 sec, MPC brings the superheat as low as the constraints allow in order to maximize the turbine power. Once the oscillatory heat signals are initiated at 2000 sec, the lower time period signals don't show significant response from the TP evaporator, which was an expected behavior as explained in section 3.3 of Chapter 3. As the time period keeps increasing, there is enough time for the heat transfer to occur from exhaust gas to working fluid and thus the working fluid temperature at the evaporator outlet becomes more responsive to changes in heat source signal. The controller response to changes in the working fluid temperature can be seen in the top plot of Figure 4.3 (b). As the time period keeps on increasing the amplitude of the working fluid flow increases. Now, since all the valve positions are fixed, a change in working fluid causes the saturation pressure to change accordingly. This can be seen in the bottom plot of Figure 4.3 (b). This causes the saturation temperature to change and since pressure dynamics is faster compared to temperature dynamics, at the on-set of 120 sec heat signal, working fluid saturates.

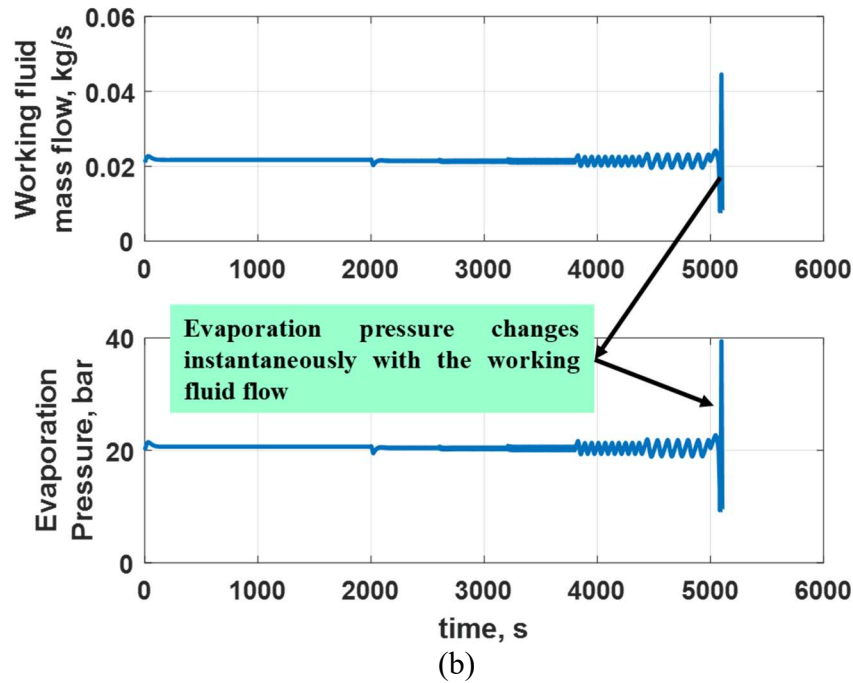
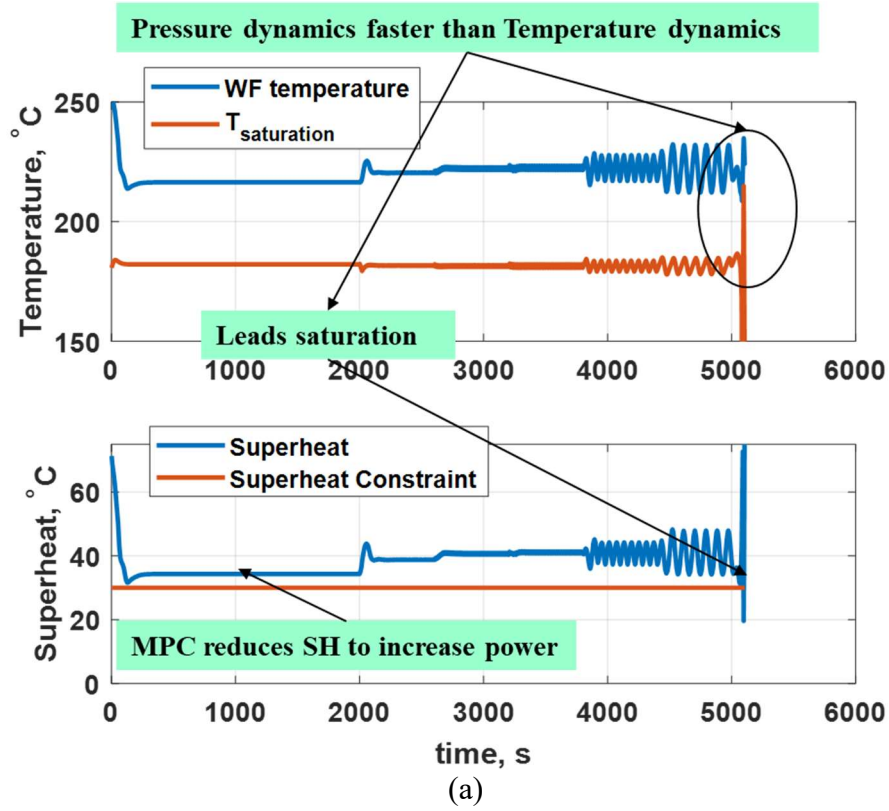


Figure 4. 3. Power maximization MPC performance for the exhaust condition shown in Figure 4.2. Plot (a) shows the response of the working fluid temperature at the evaporator outlet to different sinusoidal

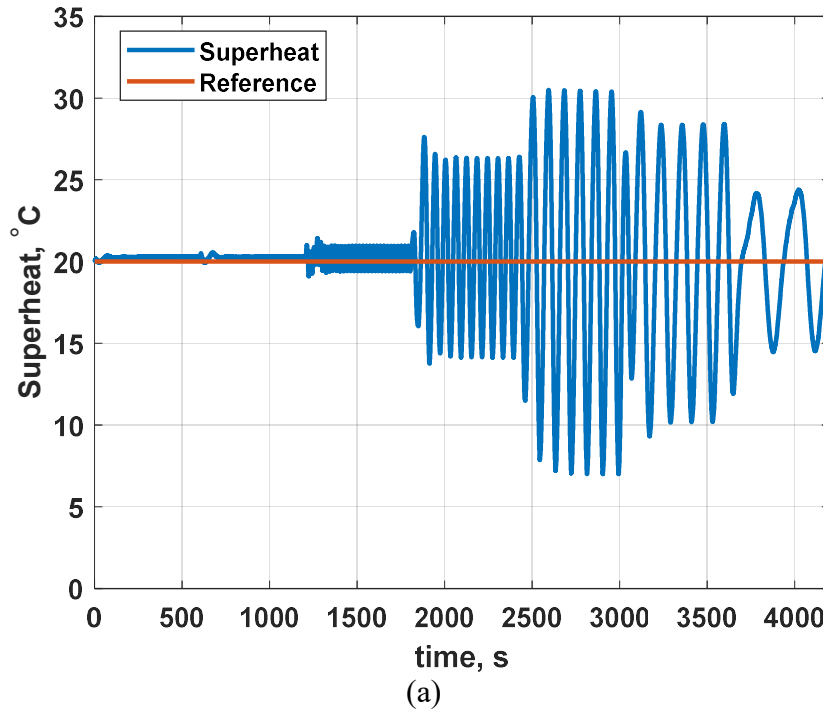
inputs with the superheat plot shown in the bottom graph. Plot (b) shows the controller generated control input and corresponding response of the saturation pressure.

The nature of the cost function, drives the MPC solution to keep the superheat as low as possible in order to maximize the turbine power. Although, the controller is not violating the minimum superheat constraint but its formulation is not helping ORC-WHR dynamics. For maximum turbine power output, minimum superheat is required which was verified from the open loop analysis and the turbine power as cost function. This suggests that tracking the power might not be the ideal cost function objective. Hence the cost function was modified to track superheat instead, as shown in equation 4.13.

$$J = W_{SH} \frac{(SH_{reference} - SH_{evap})^2}{SH_{max}} + W_{du} \frac{(du_{ref} - d_{pump})^2}{du_{max}} \quad (4.13)$$

With  $SH_{max} = 200$ ,  $SH_{ref} = 20^\circ\text{C}$ ,  $du_{max} = 0.005$ ,  $du_{ref} = 0$ ,  $W_{SH} = 1$  and  $W_{du} = 5$ .

It was found that for the TP evaporator alone, the minimum superheat that could be tracked was  $20^\circ\text{C}$  and the results of which are shown in Figure 4.4, for input heat conditions of Figure 4.2.





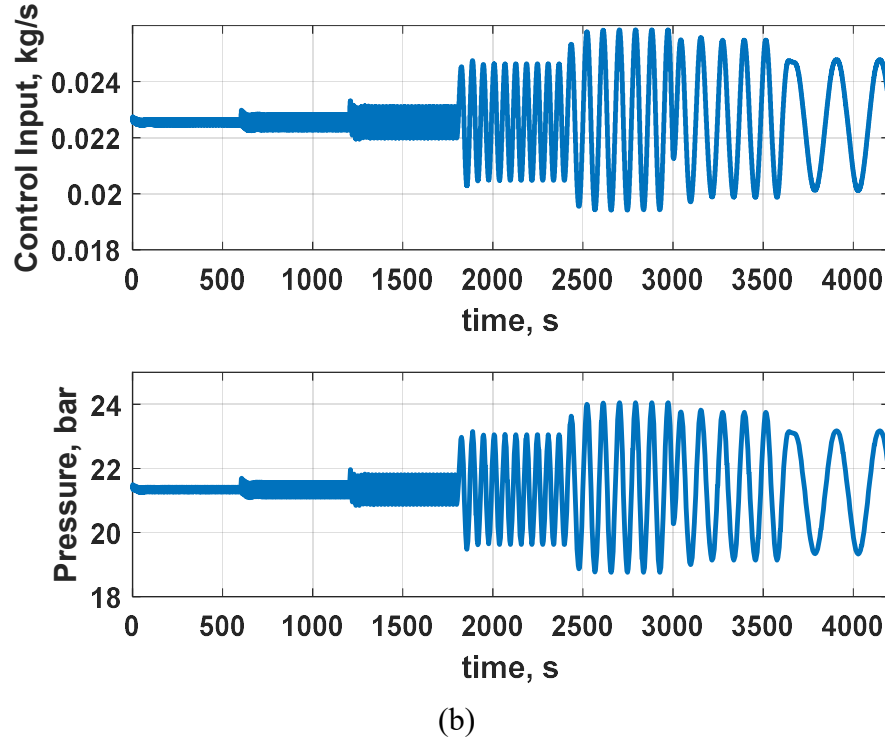


Figure 4. 4. Plot (a) Superheat tracking MPC performance for the exhaust condition shown in Figure 4.2. Plot (b) shows the controller generated control input and corresponding response of the saturation pressure.

Two important observations can be made from the results of superheat tracking shown in Figure 4.3. First, the control effort for the lower time period doesn't change at all as the thermal inertia of the evaporator is dampening the fast changing heat signals. Second, with the increase in time period of the heat signals, the dynamic response increases and significant deviation in the control input is observed. Both these observations correlate with what was observed in the open loop simulation study shown in Chapter 3.

#### 4.7.2 Disturbance Rejection

In a WHR-ORC system, the two main sources of disturbances are, 1) a mismatch between the plant and control models, and 2) measurement noise. Under such circumstances it is crucial for any controller to have robust performance and track the desire temperature as accurately as possible avoiding any steady state tracking error. The performance of the NMPC when utilizing

the disturbance augmented state estimator is evaluated in this section to evaluate the capability of the augmented system.

#### A. Plant and Control Model Mismatch

In this study, the FVM ORC plant model is more accurate than the 3 cell MBM control oriented model due to discretization disparities. In this section, we show how the disturbance augmented state estimator enhances the temperature tracking performance of the NMPC by addressing the mismatch in FVM and MBM evaporator model output predictions. Figure 4.5 below shows the step sequence of the exhaust test condition utilized for this comparison.

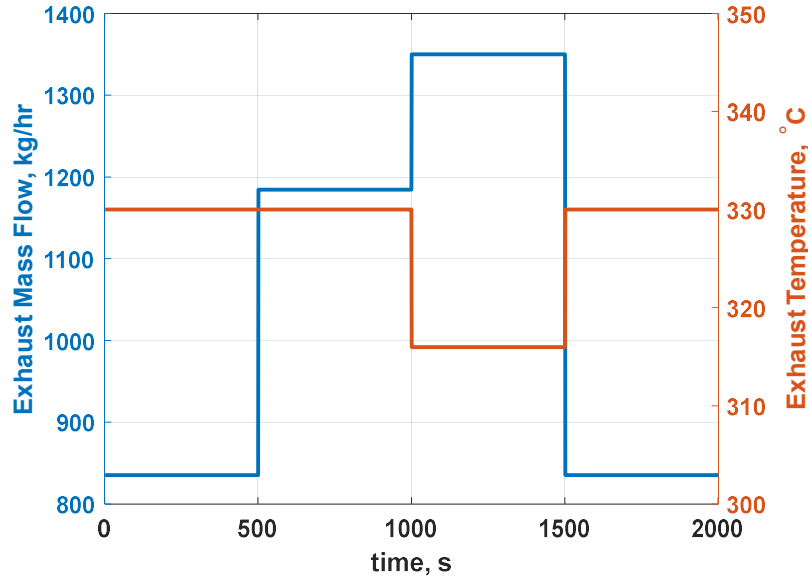


*Figure 4. 5. Step sequence of the exhaust test conditions for plant and control model mismatch comparison*

Figure 4.6 shows the NMPC performance comparison with and without the disturbance model for the test conditions shown in Figure 4.5. It can be clearly observed that, depending on the exhaust condition, there is an offset of 3-10°C without the disturbance model. Augmenting with the disturbance model decreases this offset to less than 1°C.

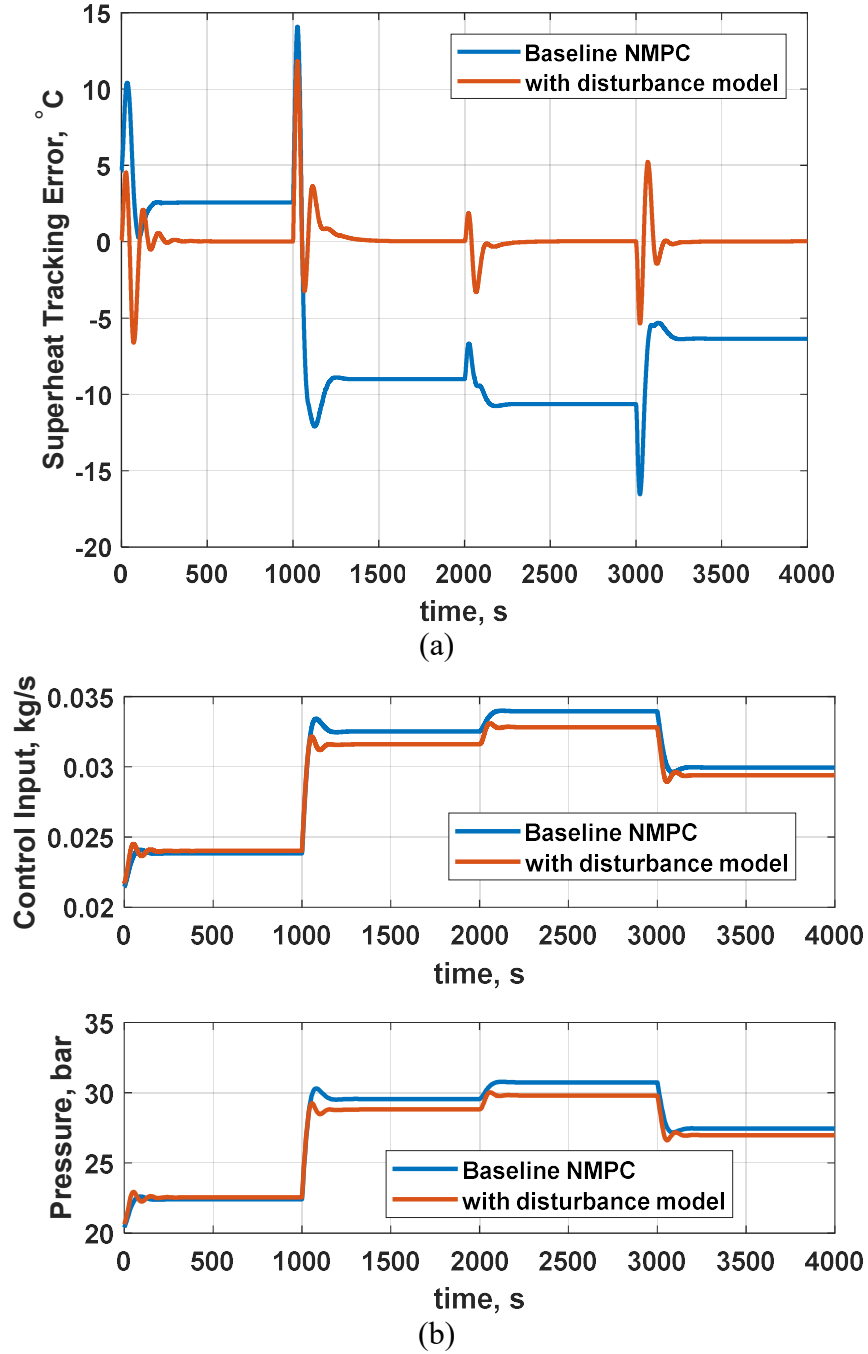


Figure 4. 6. NMPC performance comparison with and without the augmented disturbance model during a period of mismatch between the plant and control models.

The performance of the augmented model can be seen as equivalent to integral action, which assists in the elimination of steady state error. The mean absolute error using the baseline NMPC control design was found to be 7.26°C whereas inclusion of the disturbance model reduces the

mean absolute error to 0.46°C. Thus, the inclusion of disturbance model reduces the offset in tracking as expected.

## B. Measurement Noise

Exhaust gas mass flow rate and exhaust temperature determine the waste heat power available for recovery in the evaporator. On the vehicle, exhaust mass flow rate is available via the ECU whereas the exhaust temperature is measured via thermocouples. In this section, to demonstrate effectiveness of the NMPC and augmented estimator in the face of measurement noise/error, the control oriented model is purposely sent faulty thermocouple temperature values. Precisely, a constant temperature difference/offset (-10°C, + 40°C) is added to the control model input and the NMPC performance is evaluated as shown in Figure 4.7. The plant model is sent the corrected/actual values (+10°C, - 40°C) without any offsets and no changes were made to the exhaust mass flow measurements.

On perturbing the offsets, it was found that a maximum of 10 °C could be applied to the control model without affecting the controller performance whereas a maximum of -40 °C on the opposite end of perturbation was successfully simulated. As seen from Figure 4.7, even with a -40°C inform erroneous exhaust temperature sensing, the disturbance augmented NMPC performance is admirable. It is interesting to note that, for negative offsets overshoot are larger. This can be attributed to the slower response of the control input arising due to the integral action of the disturbance rejection. Setting a value for  $K_d$  in equation (4.11), is often a trade-off between decreasing overshoot and increasing settling time. In this study,  $K_d$  was chosen to be a constant for all offset conditions and, as a result, the overall response for the -40°C offset case produced more overshoot and increased settling time. It is also worth noting that the overshoot and settling

time characteristics vary with the operating conditions, which further emphasizes the nonlinearity of the heat exchanger model.

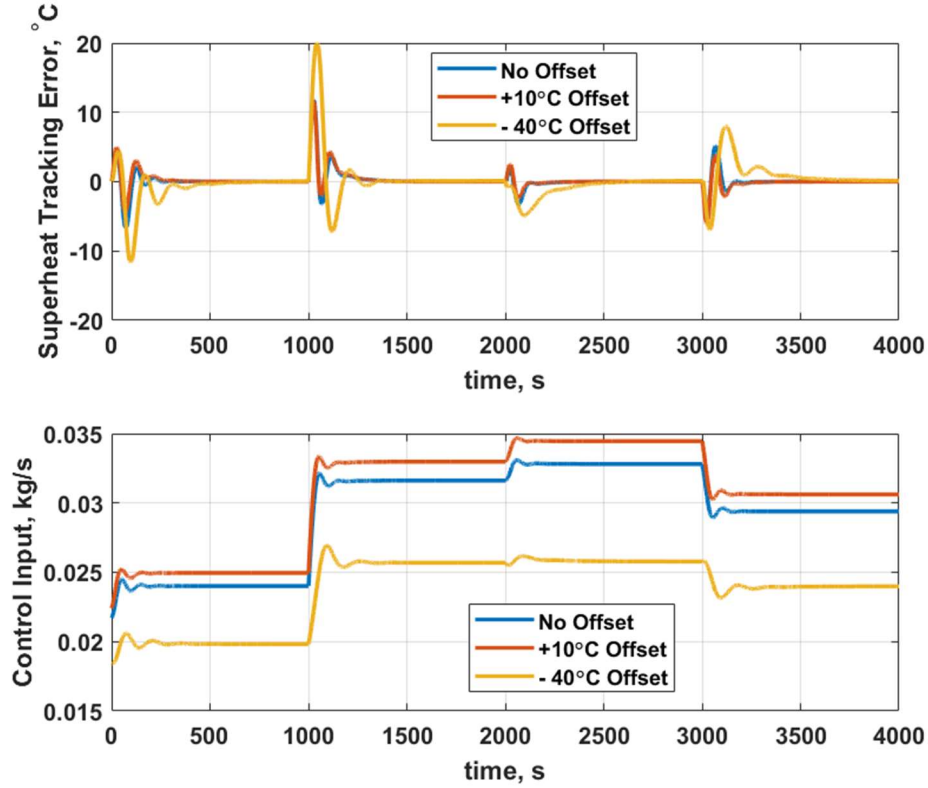


Figure 4. 7. Disturbance augmented NMPC performance comparison for various constant temperature offsets between plant and control model.

#### 4.7.3 Look-ahead NMPC

In this section, a look-ahead non-linear model predictive controller (NMPC) for tracking the working fluid evaporator outlet temperature is described. Specifically, the proposed control scheme consists of an NMPC to regulate the evaporator outlet working fluid temperature and a state estimator, which is augmented with a disturbance model. The stated approach addresses and explores two distinct features. First, the proposed MPC approach has a preview capability – i.e. the MPC incorporates future reference information into the control problem to improve the controller performance. This addresses and enhances the predictability of the nonlinear evaporator

dynamics. Second, the control oriented evaporator model is based on empirical correlations which are bound to differ from the actual component design and other disturbances like measurement noise. Hence, the inclusion of a disturbance model in the estimator design contributes to off-set free tracking by considering the model and plant mismatch. A schematic of the proposed closed-loop control law is shown in Figure 4.8.

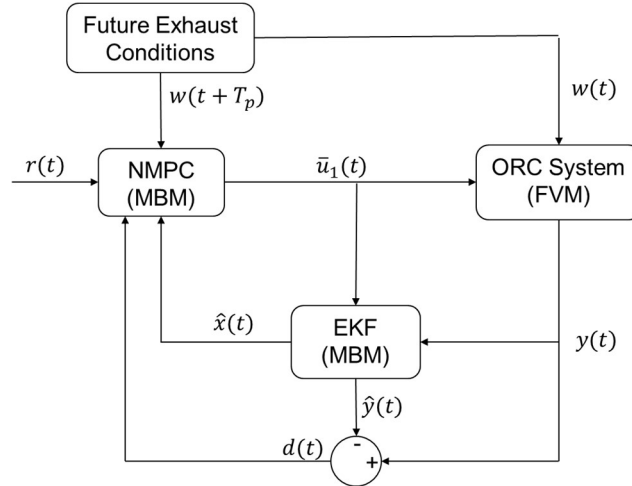


Figure 4. 8. Proposed control law for the ORC-WHR system.

In this study, it is assumed that the exhaust conditions are known for the complete drive cycle. These conditions are stored in the Future exhaust conditions block in Figure 4.8. The Future exhaust conditions block then sends out the current and future exhaust conditions based on the MPC prediction horizon. In future studies, this block will be replaced by an engine model with engine speed and torque as inputs, and exhaust temperature and mass flow as outputs.

In the following section simulation results are presented to demonstrate the performance of the proposed controller over step inputs in exhaust conditions and for a drive cycle. For this simulation study, the evaporator bypass valve is completely closed and turbine valve is completely opened, allowing the evaporation pressure to vary proportionally with working fluid mass flow rate.

## A. Drive Cycle

Figure 4.9 shows an aggressive heavy duty diesel drive cycle run on the Clemson University's state of the art heavy duty engine dynamometer. ETAS INCA was used to record ECU parameters to calculate real time exhaust mass flow rate. Thermocouple measurements of exhaust gas temperature were recorded in the tailpipe just before the evaporator. This drive cycle was developed by our project sponsor to represent a typical heavy duty truck during highway driving. The drive cycle was initiated once the engine was completely warmed.

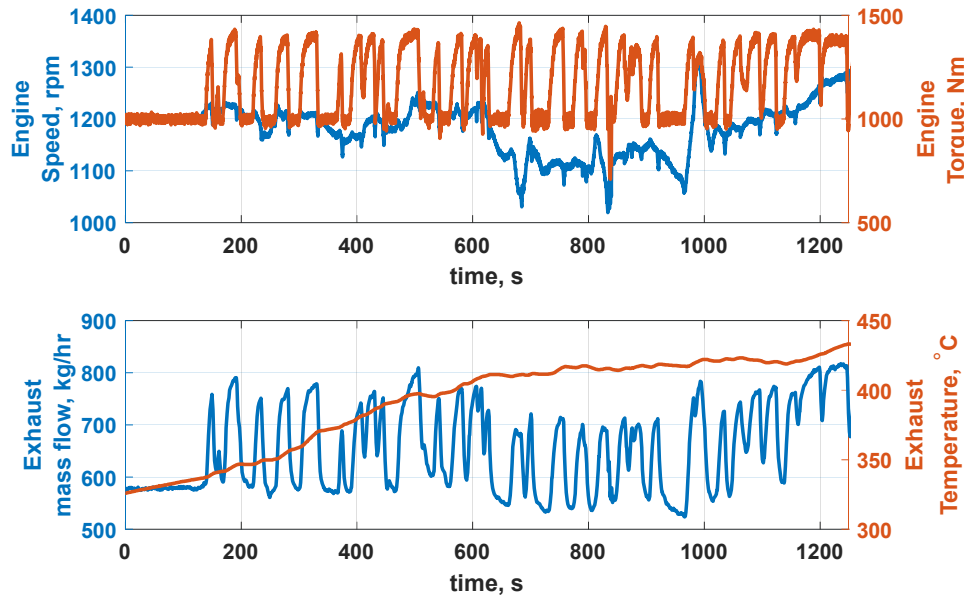
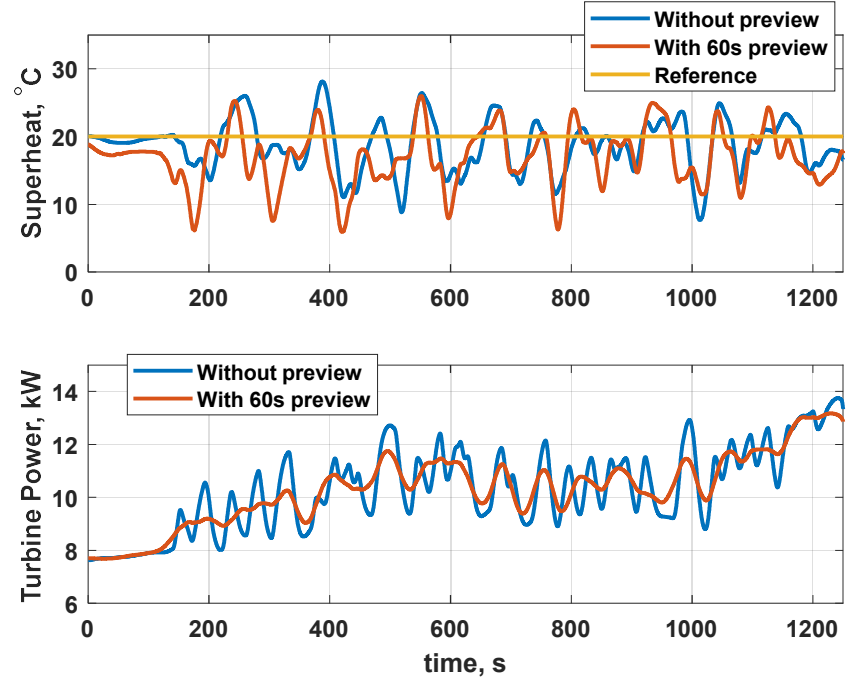
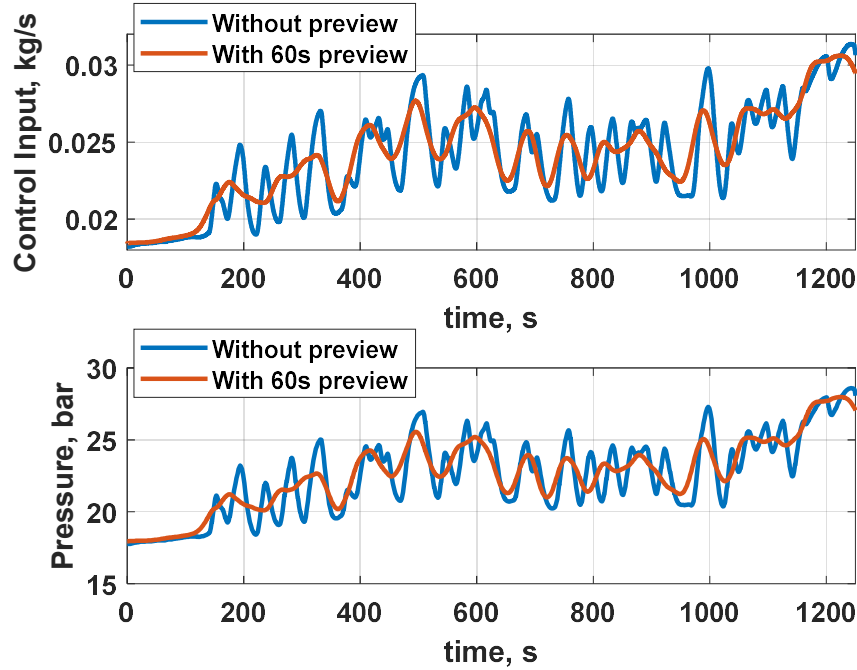


Figure 4. 9. HDDE Drive Cycle exhaust test conditions for NMPC analysis

The bottom plot of Figure 4.9 shows that the rate of change of exhaust temperature doesn't corresponds to that of exhaust mass flow. As explained before, this is attributed to the thermal inertia of the aftertreatment system, which is located upstream of the evaporator and reduces the high frequency thermal components of the varying exhaust gases. This recorded exhaust conditions are used for the following simulation studies.



(a)



(b)

Figure 4. 10. Look-ahead NMPC performance ('with preview') compared to the baseline NMPC ('without preview') during a drive cycle.

It can be observed from Figure 4.10, that the performance of both control strategies is acceptable in keeping the temperature error within  $\pm 10^{\circ}\text{C}$  during this heavily transient drive cycle.

A quantitative summary of temperature error for both strategies is shown in Table 4.1.



While the impact of the look-ahead NMPC on temperature error is minimal, there is a substantial reduction in control action with preview capability. This reduction in control action will be beneficial by increasing pump durability and reducing pump power consumption. The controlled working fluid mass flow change will also inhibit localized abrupt pressure changes inside the evaporator, resulting in uniform temperature distribution across the evaporator and better estimation of working fluid phase lengths inside the evaporator.

	Mean Absolute Temperature Error, °C	Max Absolute Temperature Error, °C	Total Turbine Energy produced, kJ
Without Preview	3.14	12.32	13.216
Look-ahead NMPC	4	14.1	13.184

Table 4. 1. Quantified NMPC temperature error comparison with and without preview capability for the drive cycle in Figure 4.9.

#### I. NMPC Preview time sweep

The look-ahead NMPC preview time window was altered to assess its impact on NMPC performance. For the drive cycle shown in Figure 4.9, three different scenarios were evaluated. The minimum prediction horizon ( $H_p$ ) for stable NMPC performance was established as 60s. Subsequently, *preview time* windows of 10s, 30s, and 60s were simulated. More specifically, for a *preview time* of 10s, only 10s of future exhaust conditions were provided to the NMPC and, for the remaining 50s of the prediction horizon, the exhaust conditions were kept constant. A summary of these conditions with results is shown in Table 4.2.

Figure 4.11 compares all three preview time scenarios. Similar conclusions to Figure 4.10 results can be made. No significant difference in temperature error prediction was observed whereas less control action overshoot was observed as the preview time increased. The 10 sec *preview time* case is tending towards the case of *without preview* from Figure 4.10. Figure 4.11 again exhibits unexpected results in terms of temperature tracking performance. No clear trend in

evaporator temperature error reduction emerged from the preview window length alterations. In an ORC system, the evaporator experiences a slower thermodynamic response because of its thermal inertia. This slow response is due to the heat capacity of the heat exchanger tube wall as well as the flow regime dependent heat transfer characteristics of the working fluid. These heat transfer characteristics are a function of the evaporator tube design, material, and working fluid properties. The evaporator design in this study was capable of filtering out large amplitude exhaust condition fluctuations, resulting in a more robust system and a more effective dynamic control. Therefore for a simplified ORC system operation, which in this case is a single evaporator operating under a constant pressure working fluid flow, knowledge of future exhaust stream conditions does not necessarily enhance the temperature tracking ability of the controller.

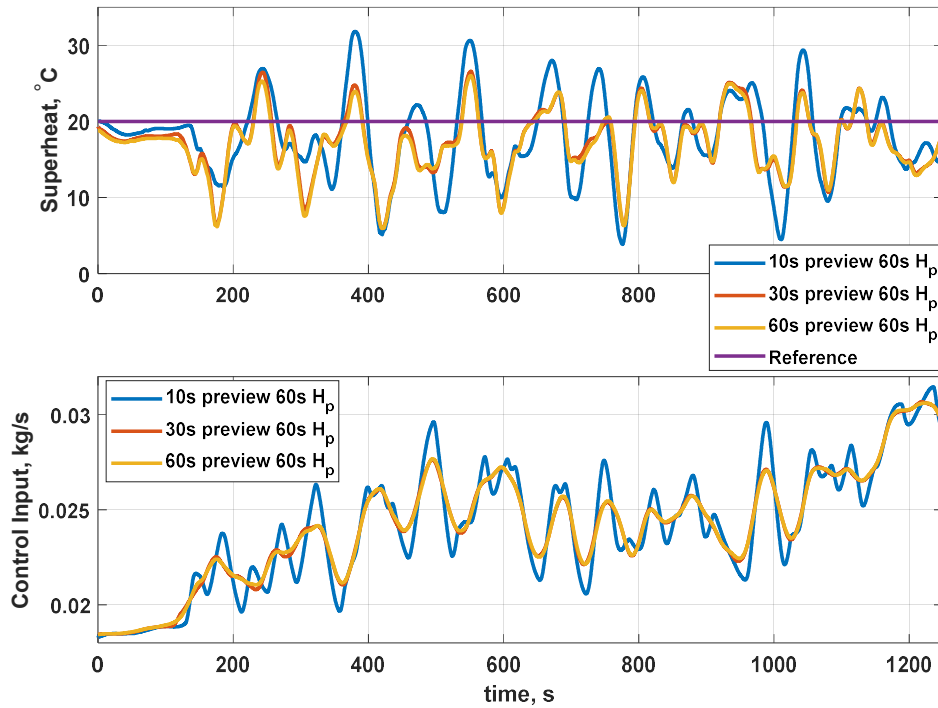


Figure 4. 11. Look-ahead NMPC performance comparison with different preview window sizes (total preview time).

Preview time	Prediction Horizon time	Mean absolute Temperature error, °C	Max absolute temperature error, °C
10s	60s	4.71	16.16
30s	60s	3.96	14.07
60s	60s	4.01	14.06

*Table 4. 2. NMPC temperature error for different preview times of Figure 4.10.*

#### B. Sinusoidal Input:

To further investigate the look-ahead NMPC effectiveness under a highly fluctuating heat loads, a sinusoidal heat exhaust source with varying frequency mass flow oscillations was designed and the controller performance was evaluated. Due to the substantial temperature trend dampening of the after-treatment system, high frequency oscillations in exhaust temperature at the evaporator inlet are not possible. Thus, for this exercise, the exhaust temperature was kept constant at 350°C while the mass flow frequency was varied as shown in Figure 4.12. For the sake of simplicity, a sinusoidal heat source was considered where half of the sine wave can be assumed to be a representative of acceleration and the other half a deceleration action. The time period of sine wave varied from 4 sec to 240 sec and was applied for 600 sec to give enough time for the controller to achieve steady state. Figure 4.12 shows the same sinusoidal signals as shown in Figure 4.2, except the initialization time period.

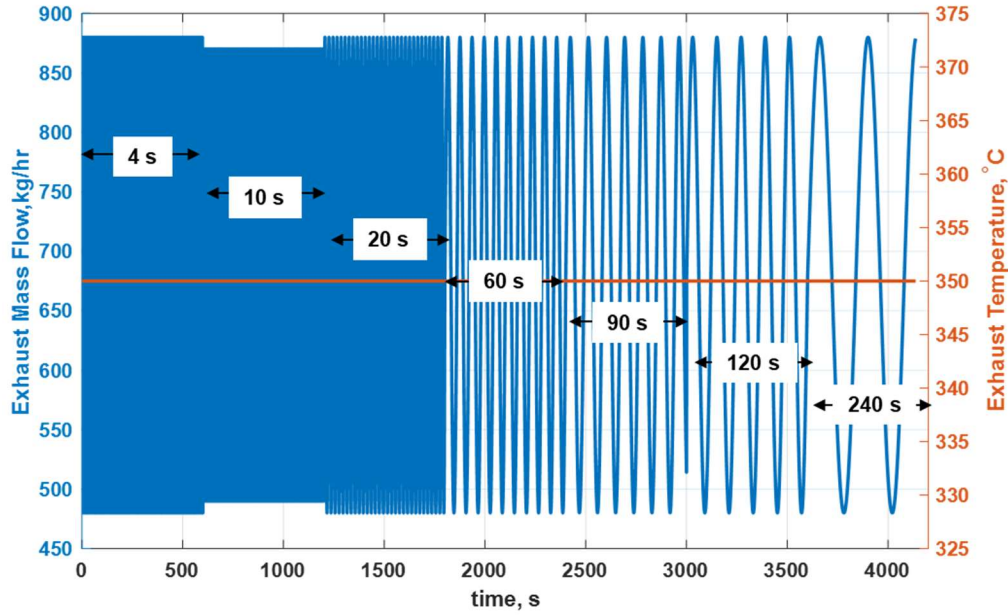


Figure 4. 12. Sinusoidal exhaust test conditions for comparison of the look ahead and baseline NMPC.

Figure 4.13 shows the performance of both the look-ahead NMPC (*‘with preview’*) and baseline NMPC (*‘without preview’*) NMPC controllers. The look-ahead preview time ( $H_p$ ) was chosen to be 60 sec. Like previous tests results, the top plot from Figure 4.12 (a) shows that the temperature error from both NMPC controllers are comparable. The summary of mean and max temperature error for each of the sine wave frequency is quantified in Table 4.3. For heat source fluctuations with smaller time periods, the temperature error is small and the error increases with the period of the heat source oscillation. For smaller heat source oscillation time periods (4 sec to 20 sec), the thermal inertia inherent to the evaporator design dampens the heat source oscillations, resulting in only minimal changes in the working fluid mass flow actuation from the controller.

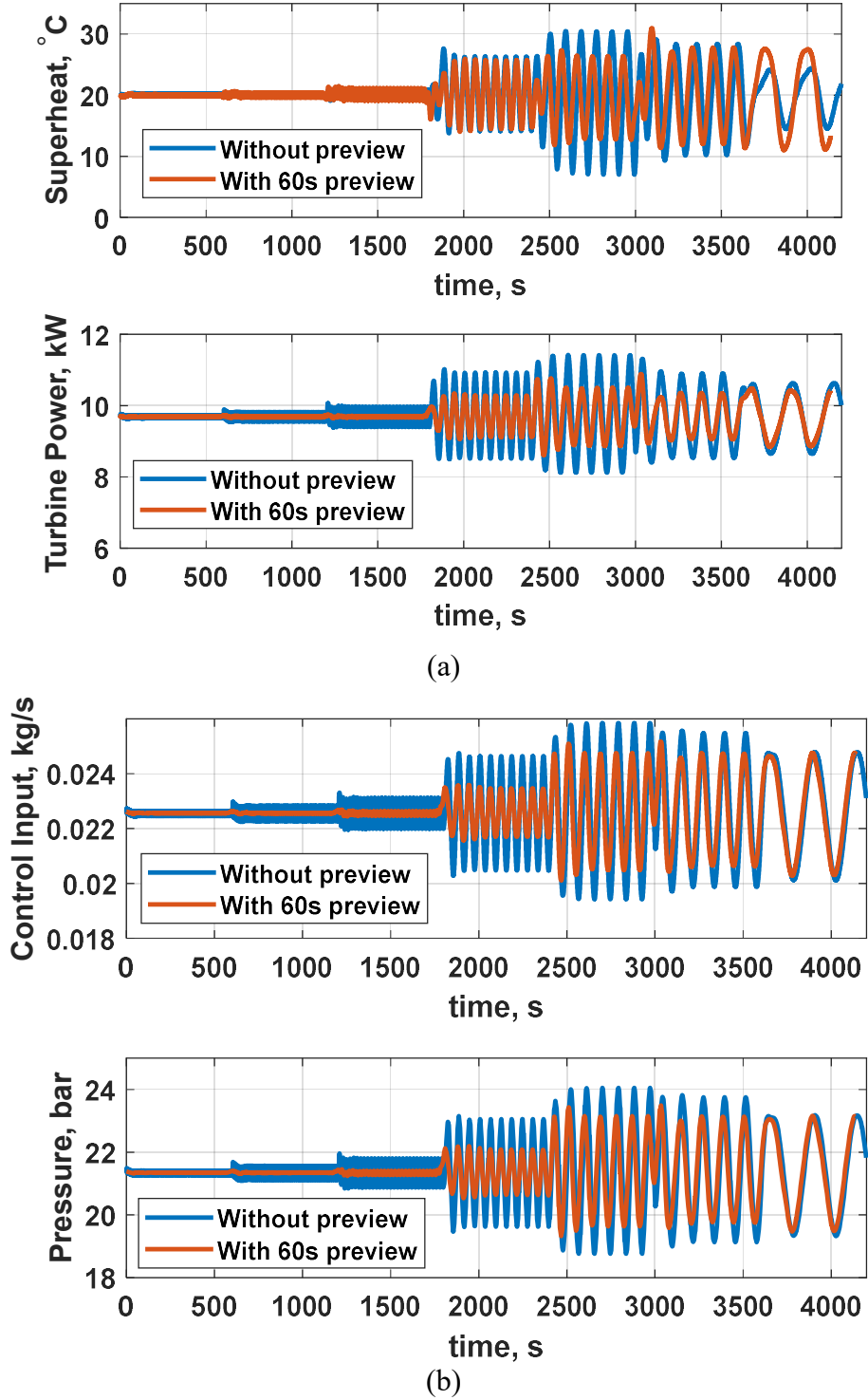


Figure 4. 13. Performance comparison for the look-ahead NMPC ('with preveiw') and the baseline NMPC ('without preview') while subjected to the sinusoidal heat source.  $H_p=60$  s. SH Reference =  $20^{\circ}\text{C}$

From Table 4.3 and Figure 4.13, it can be concluded that the mean and max error for both the controllers are comparable for all the sine waves with the exception of 60s, 90s and 120s time periods. The maximum gain was seen from the 90s time period, the look-ahead NMPC strategy showed 40% improvement in mean superheat error reduction and 37% in the max superheat error reduction. While at higher time periods look-ahead NMPC strategy generated slower control response, affecting the temperature error mitigation, as seen from 240s time period response.

Time period	Mean Superheat error, °C		Max Superheat error, °C	
	Without Preview	Look-ahead NMPC	Without Preview	Look-ahead NMPC
4s	0.22	0.09	0.36	0.33
10s	0.24	0.26	0.55	0.66
20s	0.52	0.67	1.42	2.1
60s	3.77	3.29	7.62	5.9
90s	6.93	4.17	13	8.2
120s	5.66	4.9	11.46	10.97
240s	3.25	5.46	8.3	8.98

Table 4. 3. NMPC temperature error comparison for different time periods of the sinusoidal input of Figure 4.11.

The main advantage of look-ahead NMPC is shown in the control action plot of Figure 4.13 (b). The control action of the look-ahead NMPC (*‘with preview’*) is smooth and well regulated as compared to the baseline NMPC. The reduction in amplitude of the control action is summarized in Table 4.4 using equation (4.14).

$$\% A_{reduction} = (A_{wo,preview} - A_{w,preview}) * 100 / A_{wo,preview} \quad (4.14)$$

where A is the amplitude of the control signal, *wo* = without and *w* = with.

Sinusoidal Time period	% reduction in control input amplitude Look-ahead NMPC
4s	95.38
10s	95.16
20s	85.38
60s	56
90s	33.55
120s	25.91
240s	20.25

*Table 4. 4. Percentage reduction in control input amplitude for the look-ahead NMPC ('with preview') for different time periods of the sinusoidal input in Figure 4.11.*

From the results of Table 4.3 it was concluded that for certain frequency having the preview capability helps maintain superheat within tight limits. To prove this, a further reduction in superheat reference was initiated and the simulated results are shown in Figure 4.13. As expected at lower time periods there was no change in superheat prediction. But at time period of 90 sec which showed the maximum error in Table 4.3, the control strategy without preview saturates inhibiting turbine operation and in turn reducing the power producing capability.

It is important to note that from Figure 4.13 and Table 4.3, a reduction in 5 °C superheat tracking should have been attainable by without preview control strategy. However, a reduction in 5 °C superheat causes the working fluid mass flow to increase which leads to increase in saturation pressure and therefore the saturation temperature. This increase in saturation temperature reduces the operability window for the controls strategy to track the superheat. This further emphasizes that the non-linearity of the ORC system as it changes the acceptable operability limits depending on the operating point of the system.

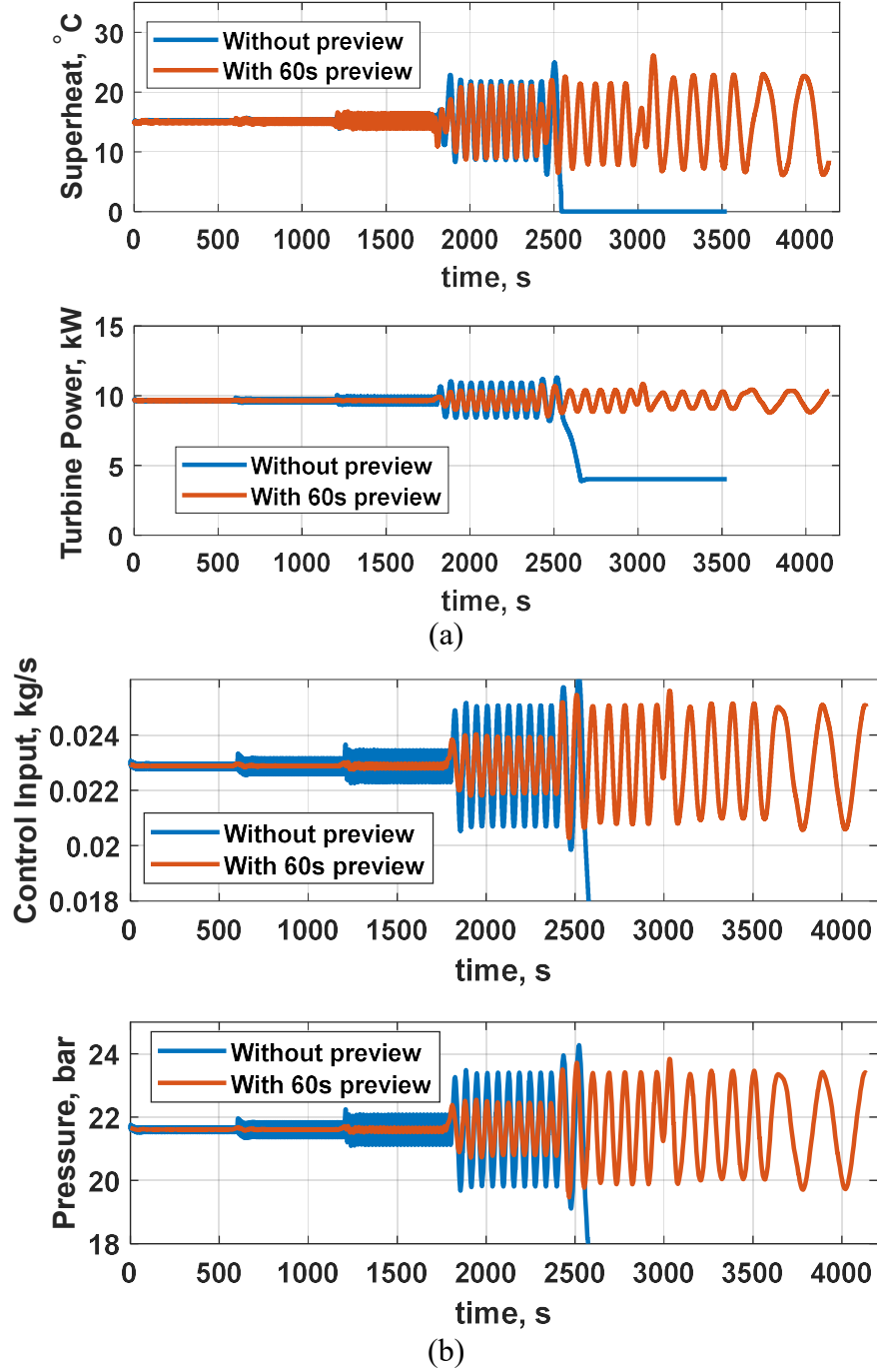


Figure 4. 14. Performance comparison for the look-ahead NMPC ('with preveiw') and the baseline NMPC ('without preview') while subjected to the sinusoidal heat source.  $H_p=60$  s. SH Reference =  $20^{\circ}\text{C}$

For a HDD truck that follows an aggressive drive cycle either through traffic or road load conditions, the corresponding exhaust conditions at the ORC evaporator can vary on 10s to 90s time intervals. In such scenarios, a look-ahead NMPC would be beneficial in reducing the ORC system control action, reducing the pump power consumption and improving system efficiency.



In addition, for control action that demands rapid variations in pump speed, the current drawn to honor the controller request would be detrimental to pump longevity. Obviously, robustness in control action is improved with the introduction of preview feature.

This case study shows the evaporator design's effectiveness at mitigating some frequency components of the fluctuating exhaust thermal load irrespective of the controller utilized. Also with the knowledge future exhaust condition dynamics, a look-ahead NMPC controller can reduce the required ORC system control action and also, to smaller degree, reduce evaporator outlet temperature error.

## 4.8 Conclusions

In this chapter, a disturbance augmented, look-ahead NMPC strategy is proposed for superheat tracking of a single evaporator WHR-ORC system. The NMPC is designed based on a 3-cell control oriented moving boundary model. For state estimation, an EKF was designed, which was augmented with a disturbance model for offset free MPC tracking.

Simulations were utilized to evaluate the performance of the NMPC over step changes in exhaust conditions and over a drive cycle. With the inclusion of disturbance rejection functionality, the steady state offset in evaporator outlet temperature decreases significantly. The disturbance rejection capability was further validated by adding 10 - 40°C modeling error during the simulation, which still produced minimal steady state temperature tracking errors. The performance comparison between a look-ahead NMPC which benefited from a preview of upcoming exhaust conditions and a baseline NMPC without a preview of exhaust conditions revealed comparable temperature tracking performance. The thermal inertia of the evaporator played a vital role in attenuating the fluctuating frequency components of the exhaust conditions. Hence, knowing the future exhaust conditions gained only minimal benefits. However, the look-

ahead NMPC generated a smoother control action. The controlled action can be helpful towards maintaining pump durability and reducing pump power consumption.

## CHAPTER 5. NMPC EXPERIMENTAL VALIDATION

### 5.1 Introduction

In this Chapter, the controller designed in Chapter 4 is experimentally validated. First, the model was calibrated online to counter the performance shifts due to system aging. Second, NMPC weights were calibrated to give satisfactory control response for both a step rise and a step down in engine conditions. Drive cycle verification showed that the thermal inertia of the evaporator helped to dampen the high frequency components of the heat source and the tuned controller limited working fluid superheat overshoots/undershoots within acceptable limits. Finally, the generated sinusoidal cycle was utilized to understand the thermal response of the evaporator for different time period of the engine conditions.

### 5.2 Background

While there are multiple studies conducted to determine the best optimal control strategies for WHR-ORC system but they are all simulation based studies, ranging from a traditional PID to more advanced model based approaches. There are only few studies that have validated their control design experimentally [58-60].

In their study, Peralez et al. experimentally compared traditional PID control strategy with a PID augmented with dynamic inverse model in feedforward control to track the superheat [58]. The ORC system utilized R245fa as working fluid which had a higher mass flow due to their limited heat carrying capacity. This high mass flow results in higher operating pressure. Therefore, for safe operation the exhaust gas was bypassed from the evaporator to limit the pressure rise inside the ORC system. This approach is not an ideal solution as it reduces the ability of the ORC system to recover heat energy.

Hernandez et al. compared MPC and PID control strategy for ORC-WHR in their experimental investigation for tracking the optimized working fluid temperature [59]. In this study, an optimal evaporating temperature is computed for tracking. The computed temperature which is a function of exhaust flow and temperature is used to track by MPC and PID. MPC outperformed PID strategy in tracking the temperature and generated 17% more electrical power output. However, this study utilized a lower order model which is identified over a specific range of exhaust conditions and for it to be implemented real time more identification needs to be done which might change the required tuning efforts and controls structure of the proposed MPC.

Seitz et al. investigated six different control approaches for possible real-time implementation strategy [60]. Following strategies were evaluated experimentally, 1) Static feedforward with PI feedback, 2) MB (Moving Boundary) feedforward with robustified PI feedback, 3) MB feedforward with LQR GS feedback (proposed controller). 4) MB feedforward with PI feedback, where P gain dependent on the sign of the control error ( $\text{sign}(T_{F,out,SH} - 15 \text{ K})$ ), and 5) IMC feedback controller, based on the simplified MB model. The proposed controller MB feedforward with LQR GS feedback (proposed controller) was found to be showing superior performance in terms of thermal to electric efficiency. However, the identified model lacks accuracy and it's valid only around the identified points. The superheat tracking of their proposed controller is poor and has maximum overshoots of 60 °C in some instances.

To address some of this concerns and gaps, this Chapter focuses on testing the designed NMPC controller from Chapter 4. This section systematically address the issues and their remedies, as faced during online implementation of the NMPC control algorithm. Three test scenarios are evaluated, ramp inputs for tuning the NMPC algorithm, drive cycle to verify the tuned weights of

the NMPC and sinusoidal heat signals to understand the frequency rejection capability of the thermal inertia of the evaporator.

### 5.3 Experimental Set-up

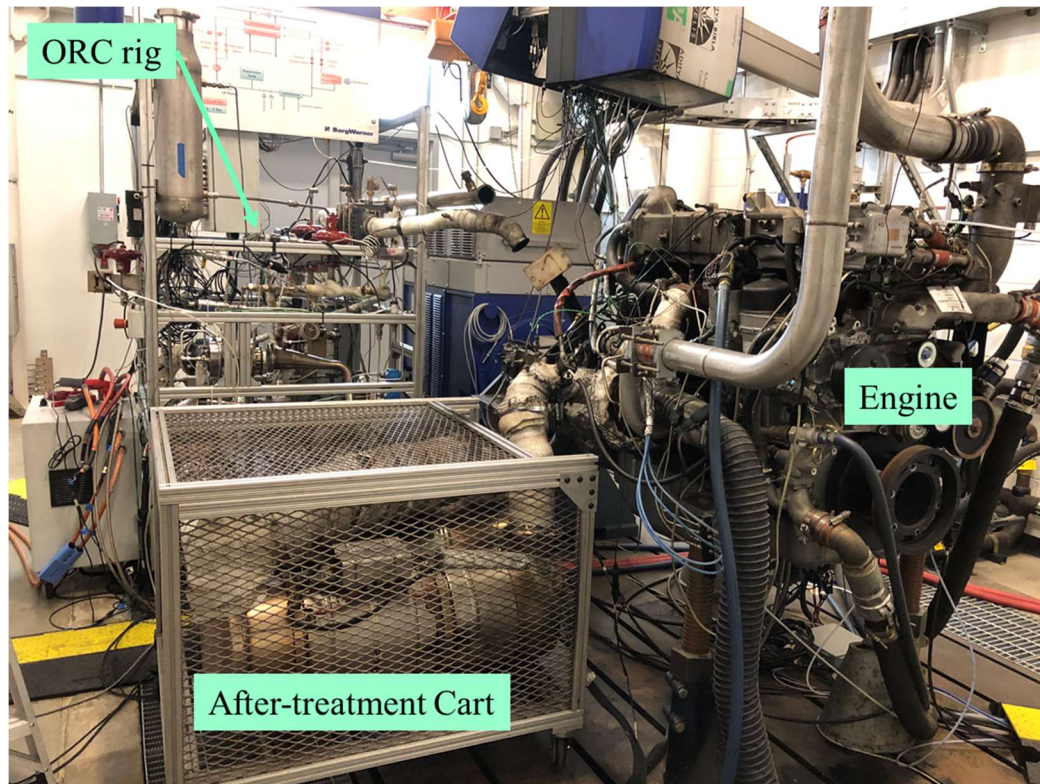


*Figure 5. 1. Experimental set-up showing the Engine, after-treatment system and the ORC rig in a transient capable heavy duty engine dynamometer at Clemson University's Automotive research facility.*

All of the following tests are conducted in a state of the art dynamometer facility at Clemson University's Automotive Engineering department. The NMPC algorithm is implemented via DSPACE MicroAutoBox to run in parallel to the engine operation. ORC system being the passive system doesn't provide any feedback to the ECU. AVL's PUMA is used to collect temperature and pressure data of the ORC system and initiate a heavy transient drive cycle. DSPCA ControlDesk software is used to collect NMPC related parameters.

All of the testing was done without the turbine in the ORC system and hence the turbine power output numbers are not available. The primary focus of this study was to investigate the superheat

tracking ability of the controller under varying exhaust conditions. In the absence of the turbine, the superheated working fluid flowed straight to condenser, which utilized the facilities water maintained at 25°C and represented infinite cooling capacity for this study. The system's lack of turbine operation did not alter the NMPC controller performance presented in this study. The working fluid temperature at the condenser outlet was maintained at 35 °C for all experiments.

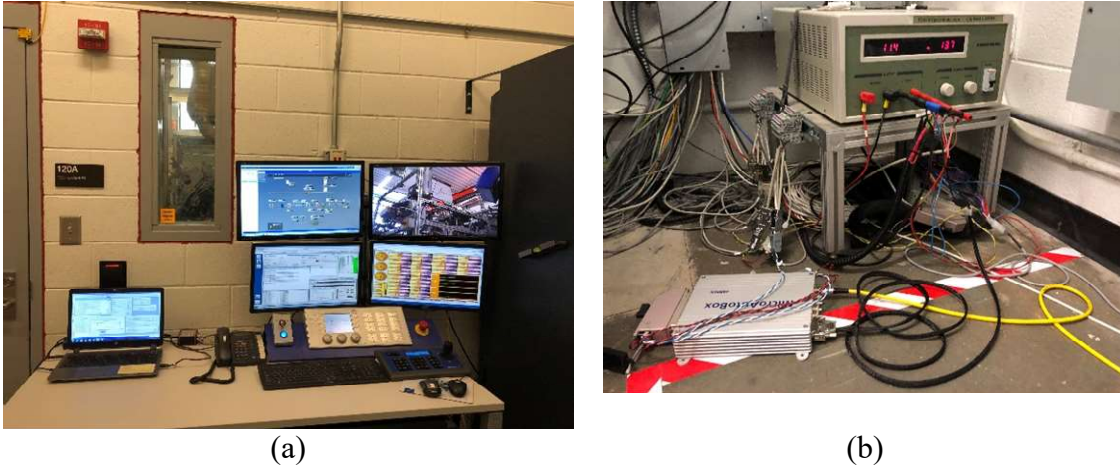


*Figure 5. 2. (a) AVL's PUMA and INCA data collection interface (b) DSPACE MicroAutoBox for implementing the NMPC algorithm*

For the NMPC validation, the prediction horizon was kept at 60 s, and equal to control horizon. For the NMPC validation, the prediction horizon and control horizon were set at 60s. The measurement update rate and the control input refresh rate were each set to 0.2 s. Note that the ORC evaporator has time constant of several minutes, making the 0.2s ample time for the controller to take appropriate action in response to varying exhaust conditions. The turbine bypass valve was fixed at 30% open and the turbine valve was closed for the entire test. This allows the evaporation pressure to vary as per the working fluid flow rate. Ethanol was used as the working fluid for this ORC system.

#### 5.4 Online Model Calibration

The system under consideration consisted of prototype components and had accumulated a significant run time hours over the course of this development project. Due to which at the

beginning of the NMPC testing a system level performance shift was observed because of system aging. The exact cause of the aging is being investigated. The hypothesis for the potential causes of this aging could be working fluid aging, internal working fluid leakage not captured by the flowmeters or component damage/aging.

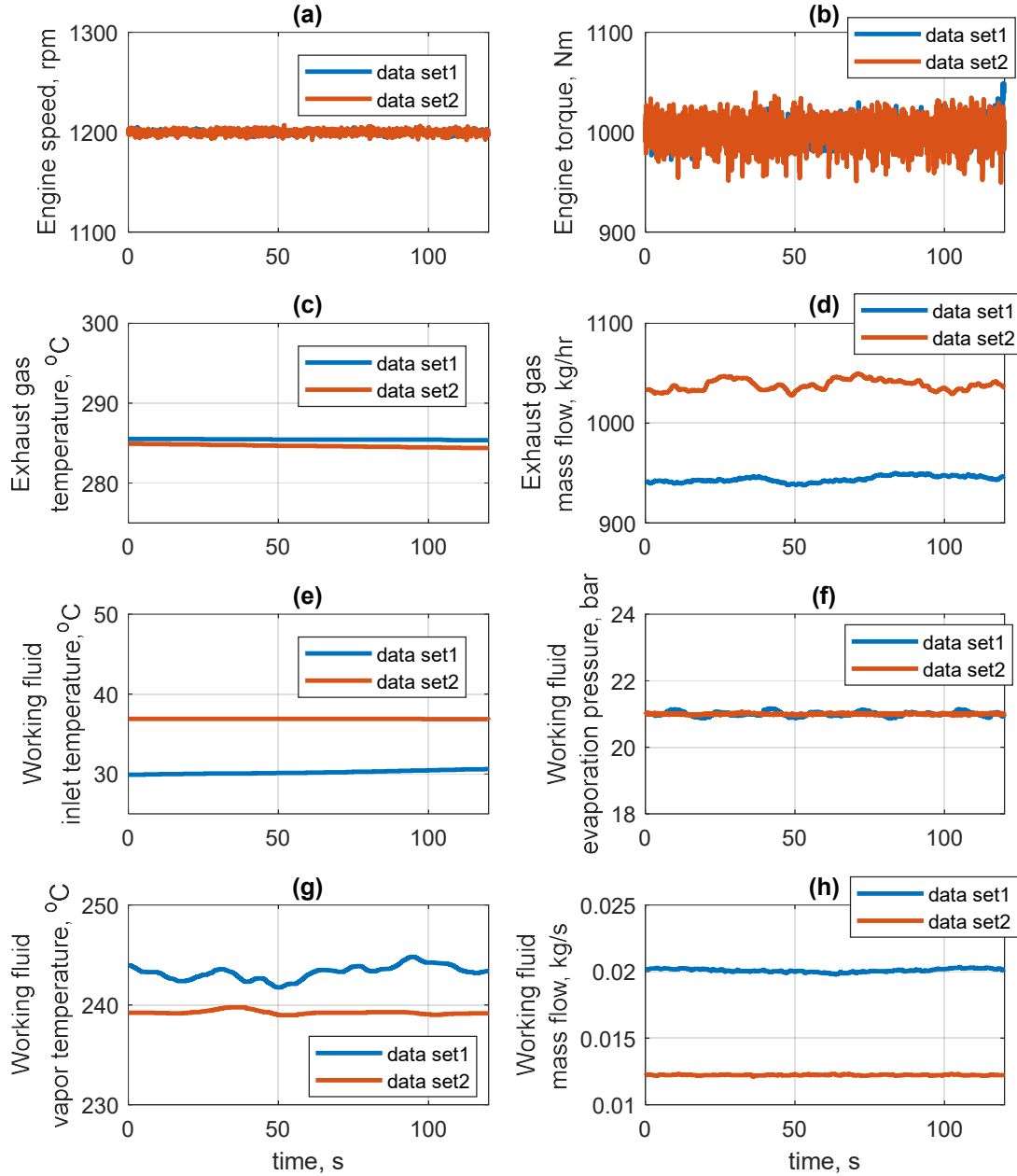


Figure 5. 3. System aging characterization for the same engine conditions with data set 1 being the green ORC system and data set 2 representing the aged ORC system.

Shown in Figure 5.3, is an example of performance comparison of the aged system with respect to the green system. For identical engine conditions and working fluid superheat set-point, the required working fluid flow was 40% lower. The heat transfer coefficient described in equations (4.1 – 4.3) of chapter 4, was re-calibrated to match the performance of the aged system.

#### *5.4.1 EKF state estimation error*

A high heat transfer rate was observed for the green ORC system and thus a higher heat transfer coefficients were identified during evaporator identification process for the control oriented model. EKF also utilizes this control-oriented model for state estimation. Now, due to system aging, the EKF generated erroneous states. The higher baseline heat transfer coefficients resulted in over-predicting of the working fluid outlet temperature.

An example of behavior of the aged system relative to the estimates based on green system is shown in Figure 5.4. The engine conditions are held constant at 1200 rpm 1000Nm. In the first 200 sec of Figure 5.4, it can be seen that the baseline heat transfer coefficients made the model overestimate the evaporator outlet temperature due to aged system's reduced mass flow at the same working fluid superheat set-point and that resulted in over-prediction of working fluid evaporator outlet temperature. This lead to the over-prediction of working fluid enthalpy and a larger vapor phase region culminating in decreasing phase lengths L1 and L2 for pure liquid phase and mix phase, respectively.



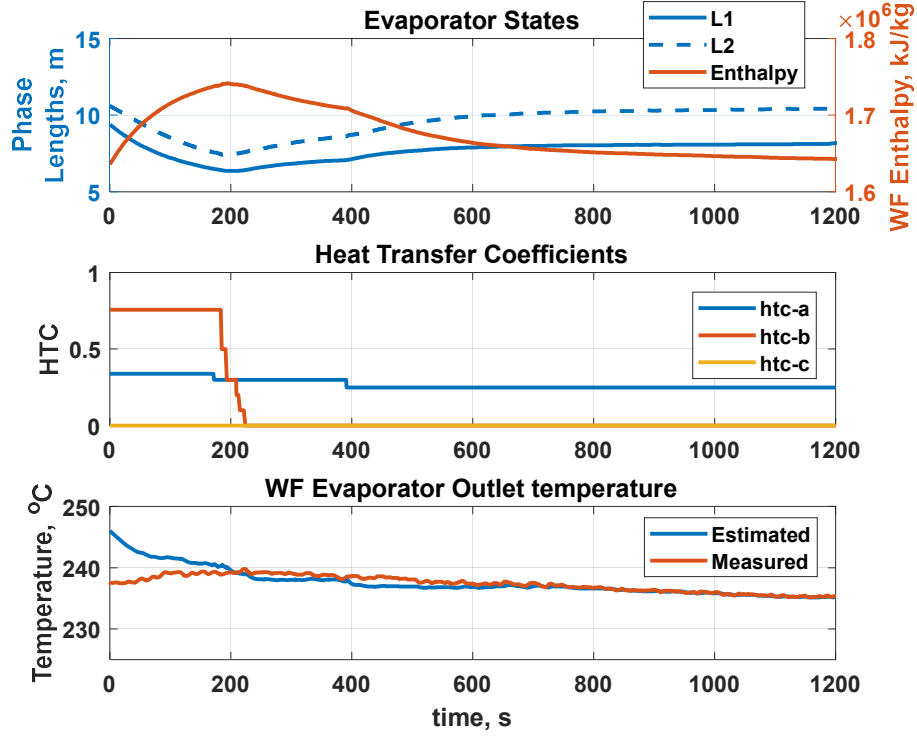


Figure 5. 4. Online tuning of heat transfer coefficients for MBM of TP evaporator resulted in stable state estimation by the EKF

To reduce error in the EKF estimation, the heat transfer coefficients were reduced in Figure 5.4 until working fluid outlet temperature agreement was obtained. The recalibration of these coefficients resulted in stable phase length estimations and working fluid enthalpy predictions. The new identified heat transfer coefficients were used for the remainder of the testing. This exercise of online tuning the heat transfer coefficients depending on the age of the system showed that it's vital to keep track of the system level performance shifts. For model based advanced controls strategy modeling a parameter characterizing the system age would be beneficial.

The proposed control approach that was shown in Figure 4.8 can serve as a frame-work to include a system aging adaptation variable,  $\varepsilon(t)$  that will manipulate the heat transfer coefficients as shown in Figure 5.5.

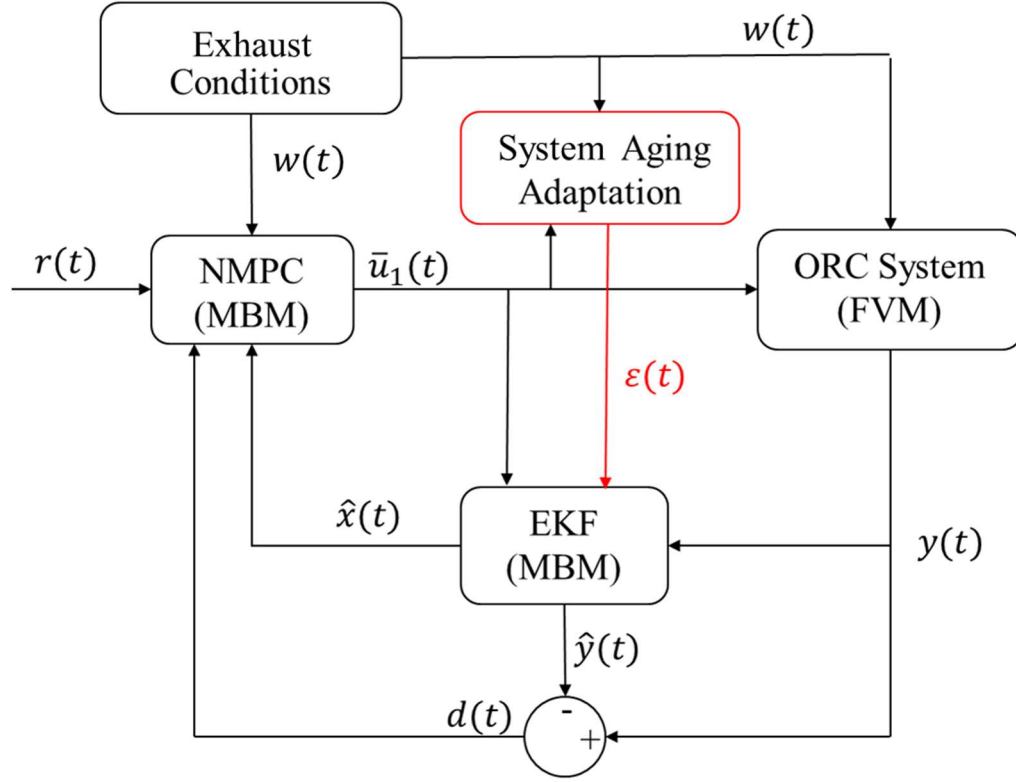


Figure 5. 5. Proposed control law (Figure 4.8) incorporated with *system aging adaptation variable,  $\varepsilon(t)$* .

The system aging block will store the working flow mass flow required to maintain a fixed amount of superheat at the evaporator outlet for a set of exhaust conditions. Then, in real time implementation the working fluid flow from the NMPC block will be compared to the stored working fluid mass flow values for that set of exhaust conditions. If the required working fluid flow is less than the stored values than the  $\varepsilon(t)$  value will manipulate the heat transfer coefficient for the MBM model in EKF block. In future experimental testing, a nominal operating would be repeated at equal intervals to understand the behavior of the heat transfer coefficients as the system ages. This will dictate the necessary change in  $\varepsilon(t)$  variable needed to accurately portray the age of the system.

## 5.5 Ramp-up and Ramp-down Events

A conventional method of controller tuning is examination of its response to step changes. In this section, two input ramps (with rise times of 30sec and 5sec) of engine speed and torque are used to analyze the evaporator response and tune the NMPC weights towards tracking a constant superheat of 60°C. Note that a superheat of 60°C was recommended by the project sponsor to safeguard these early prototype components and to avoid constant switching between saturation and vapor phase as the controller was tuned. In simulation, it was concluded that the best way to optimize turbine power was to lower the superheat temperature. In future testing, this reference will be optimized further with the turbine installed.

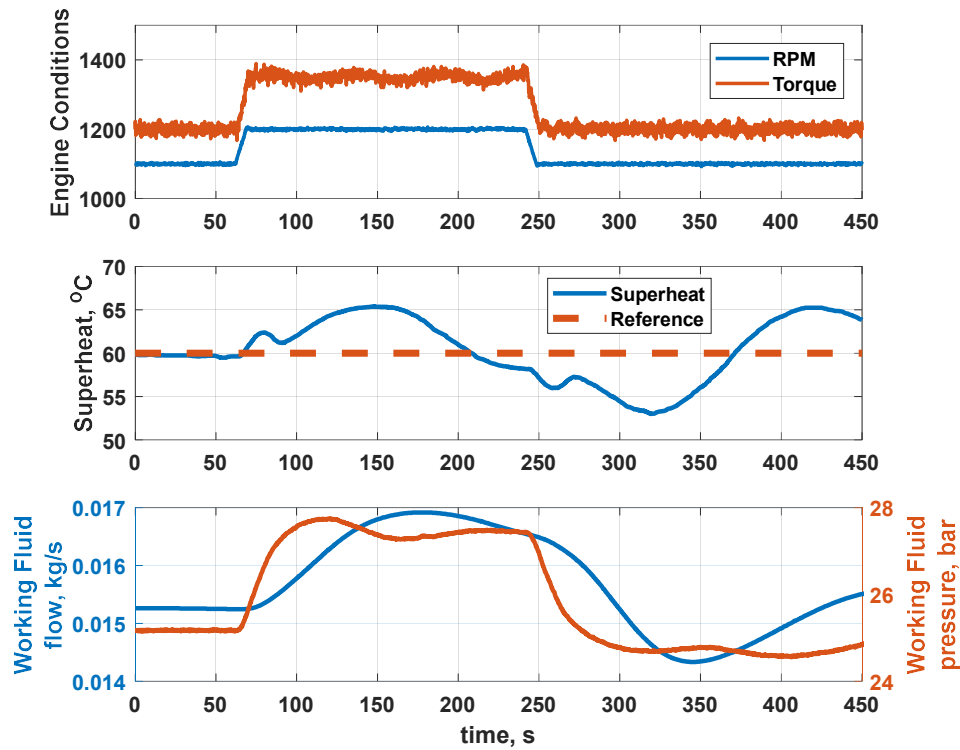


Figure 5. 6. Tuned NMPC performance for a 30s ramp in engine conditions.

The weight  $W_{du}$  in the cost function shown in equation 4.13 in Chapter 4, was tuned to 20 to give an acceptable performance in superheat tracking of  $\pm 5^\circ\text{C}$  as shown in Figure 5.6. In the tuning process, it was found that to ensure superheat tracking within  $\pm 5^\circ\text{C}$  a larger weight on  $du$

term was necessary. The slower evaporator response due to its thermal inertia required a slower change in mass flow to maintain tracking performance for both the rise and fall in engine conditions.

It should also be noted that the first 60 sec of Figure 5.6 shows zero steady state error which confirms that the disturbance model introduced in the NMPC formulation is performing as anticipated. Since the both the turbine bypass valve and the turbine valve were fixed, the change in working fluid flow changes the evaporation pressure as seen from the bottom plot of Figure 5.6. This change in evaporation pressure changes the evaporation temperature which in turn affects the superheat tracking condition.

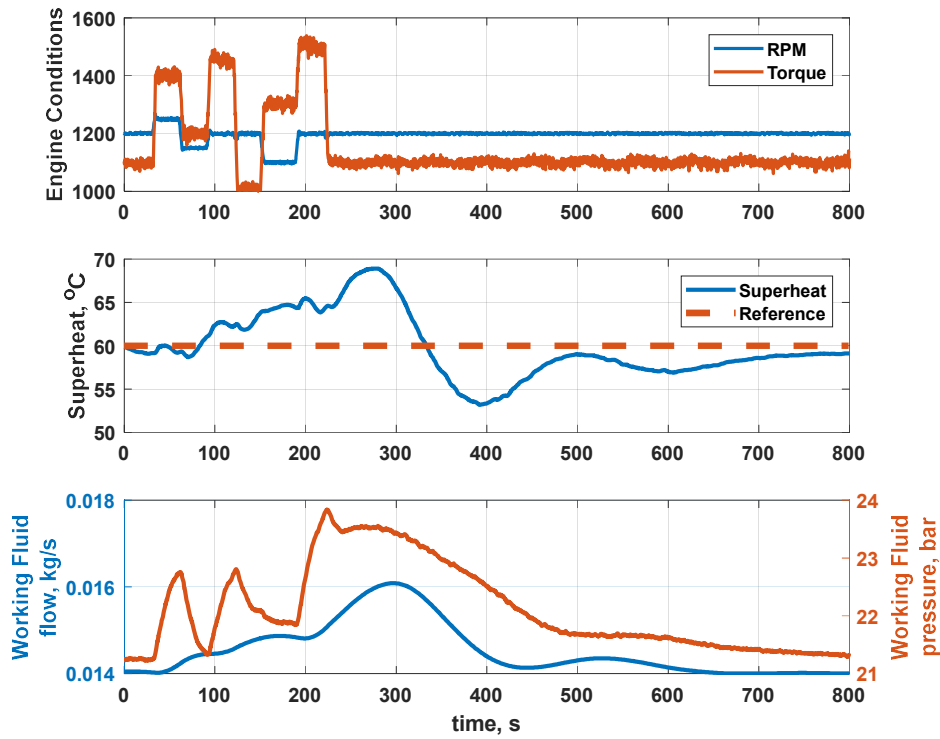


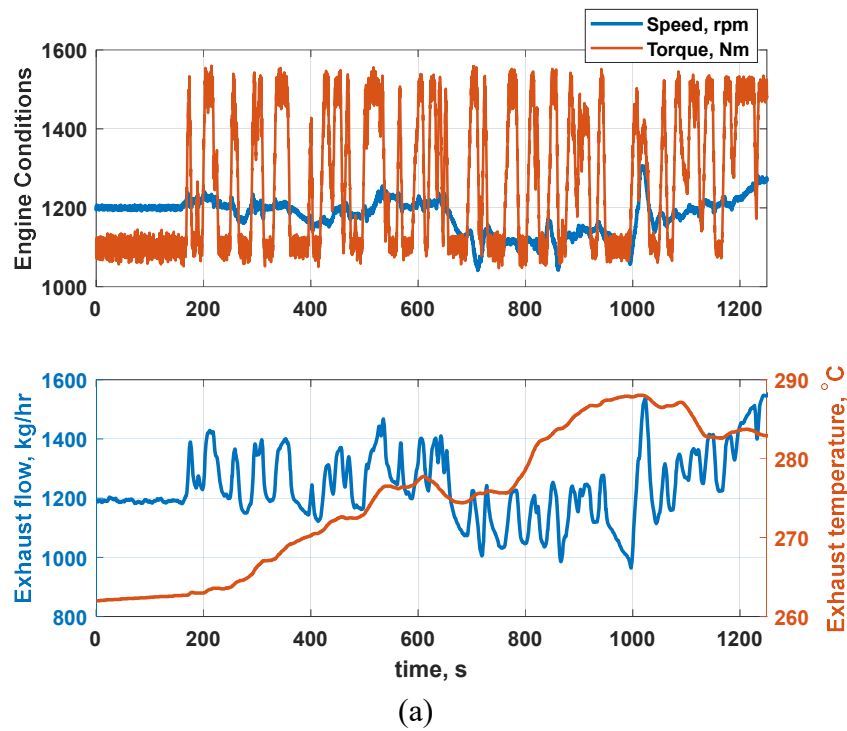
Figure 5. 7. Tuned NMPC performance for a ramp input of rise time 5 sec

Next, the controller performance in response to a more aggressive 5s ramp in engine conditions is shown in Figure 5.7. With the same cost function weights, the tracking performance is outside the  $\pm 5^{\circ}\text{C}$  target range, however the overshoot is still below  $10^{\circ}\text{C}$  and is easily recovered as seen

after 400 sec in Figure 5.7. Again the controller performance remarkable in reducing the steady state error.

## 5.6 Drive cycle

A true test of the controller would be to verify its performance on heavy transient conditions representative of real-world driving. For this an engine dyno test cycle was developed as shown in Figure 5.8 (a). In real world operations, majority of the life cycle of a heavy duty diesel engines is spent on highways and accordingly a near constant engine speed and variable load cycle was developed. The bottom plot of Figure 5.8 (a), is the corresponding exhaust mass flow and temperature conditions recorded at the evaporator inlet location.



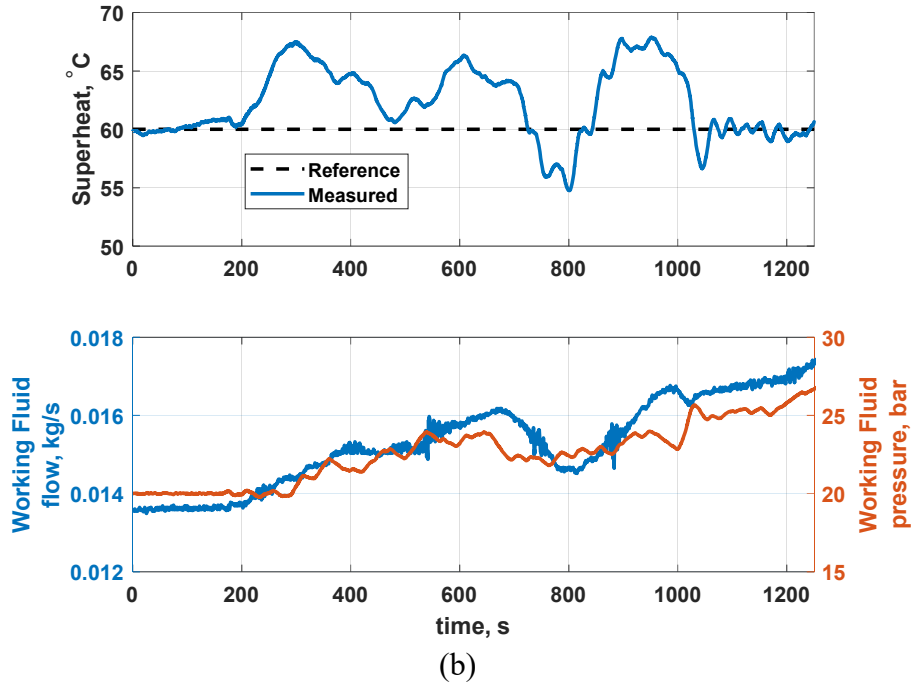
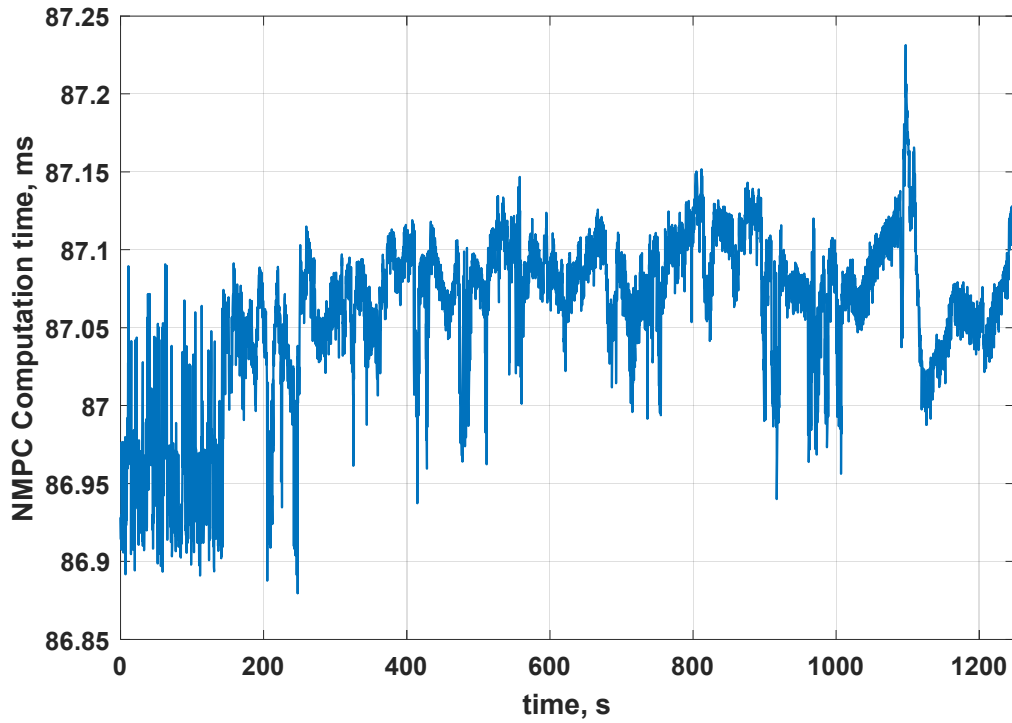


Figure 5. 8. (a) Engine conditions for the constant speed drive cycle (b) Tuned NMPC superheat tracking performance and generated working fluid flow rate

As seen from the exhaust condition plot, the mass flow dynamics are fast, changing rapidly with the drive cycle. However, temperature dynamics are relatively slow and dampened by the after-treatment system. The NMPC superheat tracking performance over this highly-transient engine cycle is provided in Figure 5.8(b). The maximum overshoot in working fluid superheat is  $7.9^{\circ}\text{C}$  with a mean error of  $2.9^{\circ}\text{C}$ . The working fluid flow predominantly mimics the exhaust temperature trend without suffering variation from the highly transient exhaust flow changes. This can be attributed to the high frequency of the exhaust gas flow and the large thermal inertia of the evaporator.



*Figure 5. 9. NMPC Computation time for the constant speed drive cycle*

An inhibiting factor for real time MPC implementation is the incurred computation cost. The designed controller and model computation time averaged 87ms over the entire drive cycle as shown in Figure 5.9. With an update rate of 0.2s, the controller has ample time to complete the calculations and provide optimal control inputs to the system.

In Chapter 4, it was found that the main advantage of knowing the future exhaust conditions is reduced control effort, however in the experimental validation no significant variation in working fluid mass flow was observed as seen from the bottom plot of the Figure 5.8 (b). Therefore, in the drive cycle case, the preview capability was not validated experimentally. Instead, a series of sinusoidal exhaust conditions were experimentally tested to evaluate the controller performance.

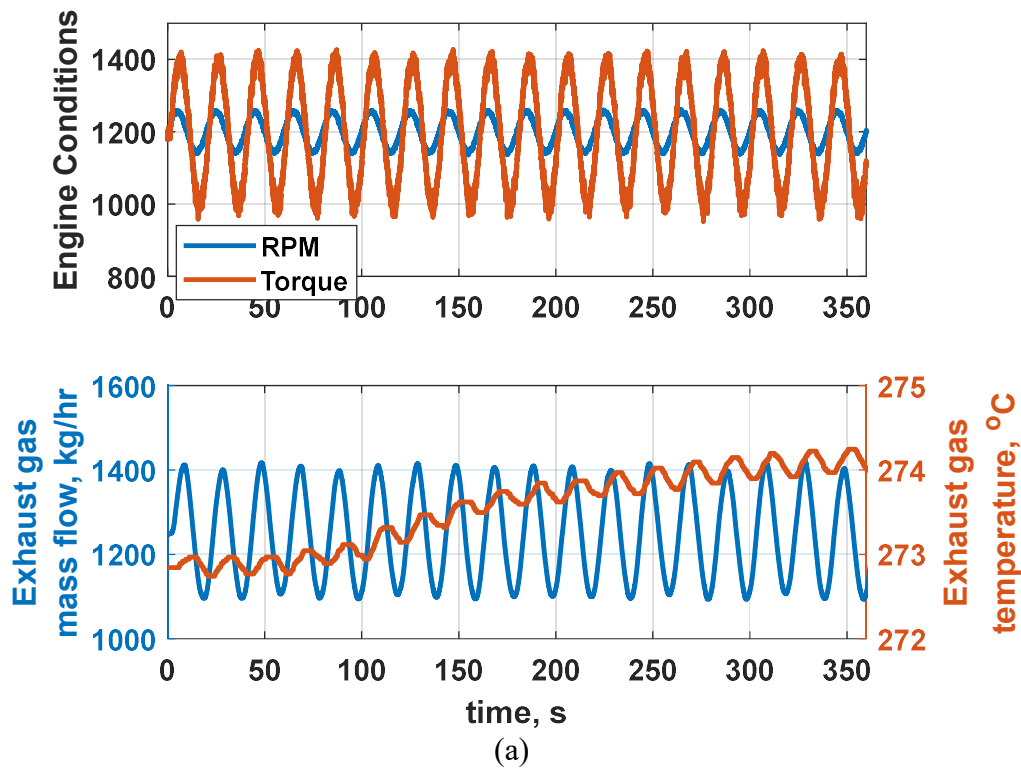
### **5.7 Sinusoidal Inputs**

Since no oscillatory behavior was seen during the drive cycle tests. Sinusoidal tests were conducted at different frequency to understand the variation of the heat transfer process and best

approach to tune the given ORC system under different frequency of heat signals. This set of tests were prepared to be in correspondence to the open loop simulation done in Chapter 3. For this analysis, controller performance is experimentally evaluated over a series of sinusoidal heat signals with time periods of 20 secs, 60 secs, and 120 sec.

#### 5.7.1 Time period of 20 s

From the perspective of real world applicability a sinusoidal waveform can be treated as alternate acceleration and deceleration/coast-down. To generate the sinusoidal exhaust conditions at the evaporator inlet and recognizing the real world applicability, amplitude of the engine speed was kept at 100 rpm whereas amplitude of the torque was kept at 400 rpm. Figure 5.10 (a) shows the engine conditions for 20 sec time period. As stated before the dynamics of exhaust mass flow is in cohesion with the engine speed and torque. Whereas the exhaust temperature is seen steadily increasing with a dampened frequency component.





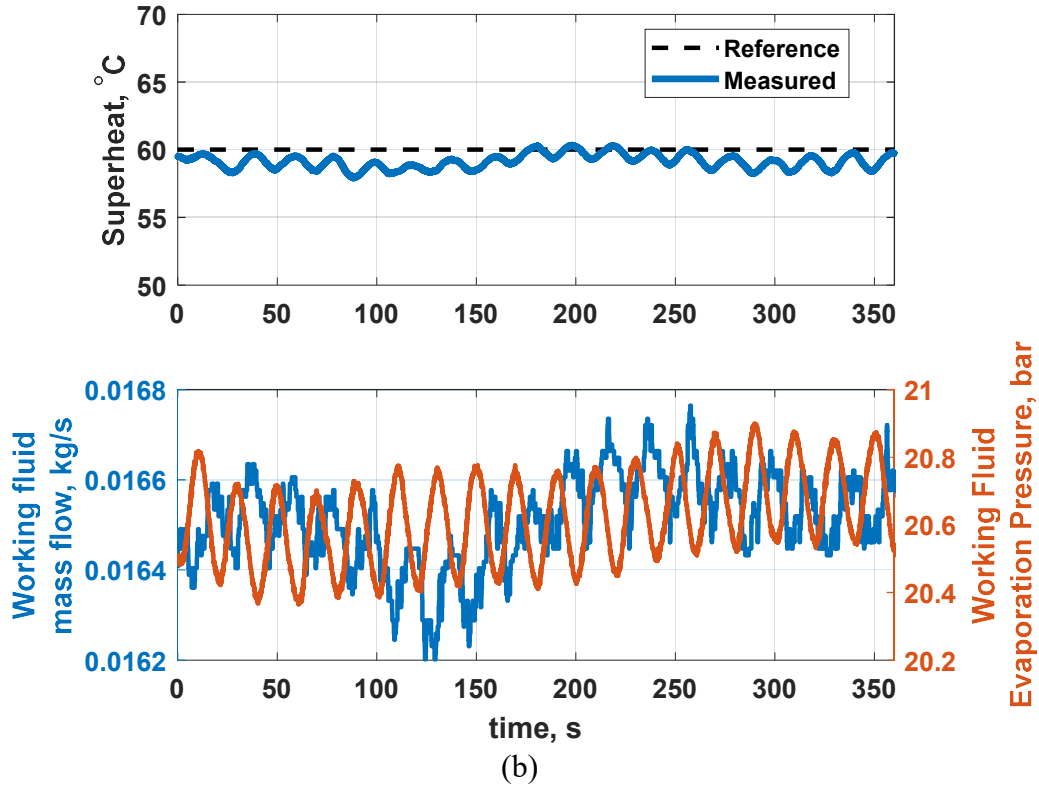


Figure 5. 10. (a) Engine conditions for the sinusoidal cycle with time period of 20s (b) Tuned NMPC superheat tracking performance and generated working fluid flow rate,  $W_{du}=10$

With very high frequency of heat source, there is no time for heat transfer and in this case the change in control effort needed to maintain superheat tracking is very low. This was expected as described in the open loop simulation in Chapter 3.3 and in Chapter 4.7.3 B. As a result, the required working fluid flow steadily increases over time with increase in exhaust temperature. The maximum absolute superheat tracking error was found to be 2.1 °C and mean error was 0.87 °C.

#### 5.7.2 Time period of 60 s

Engine conditions for a 60 s heat signal is shown in Figure 5.11 (a) and was run for a 600 sec. With the same weights,  $W_{du}=20$  as for the 20 s time period, slight oscillations can be seen in the superheat tracking performance.

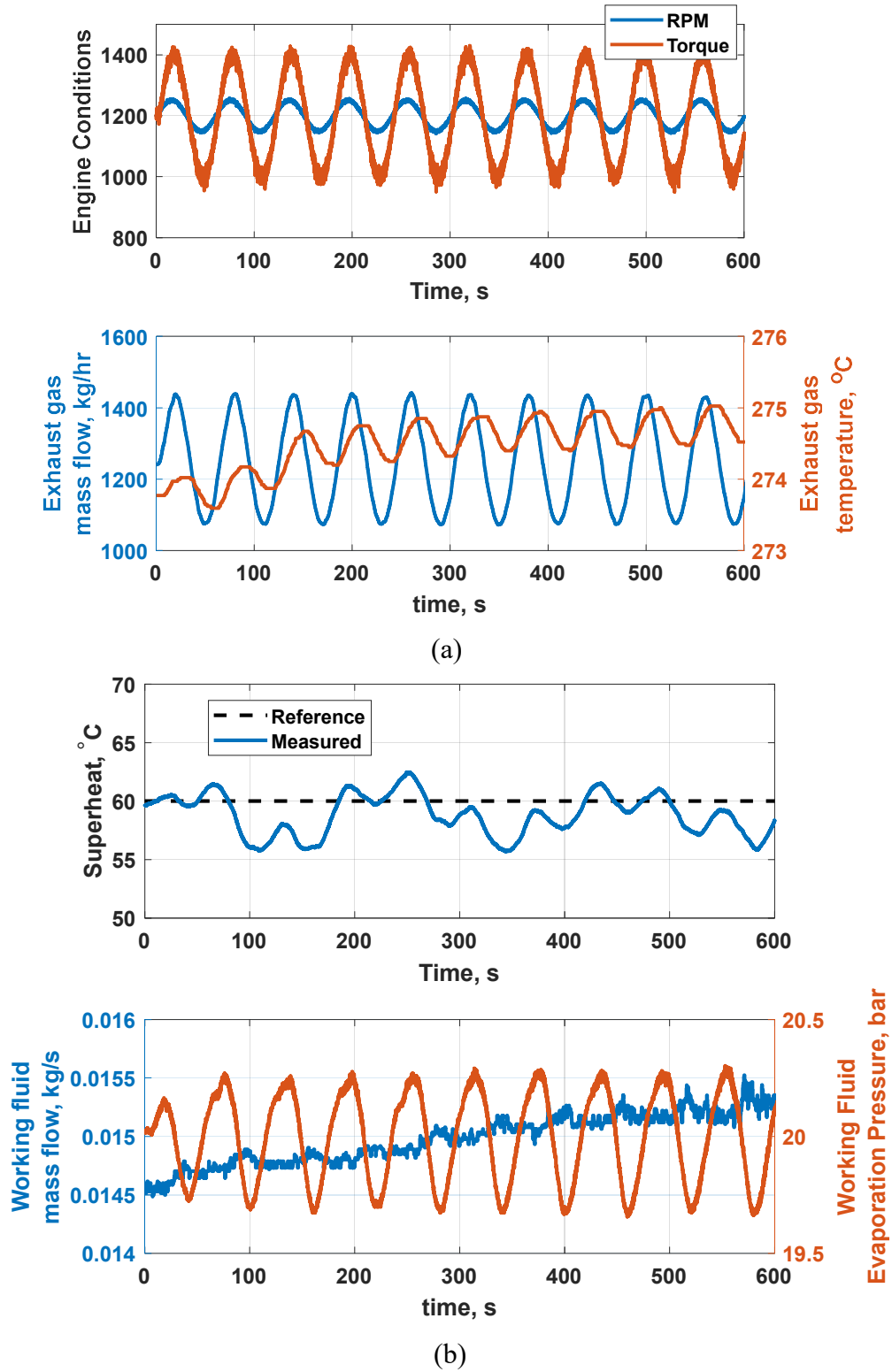
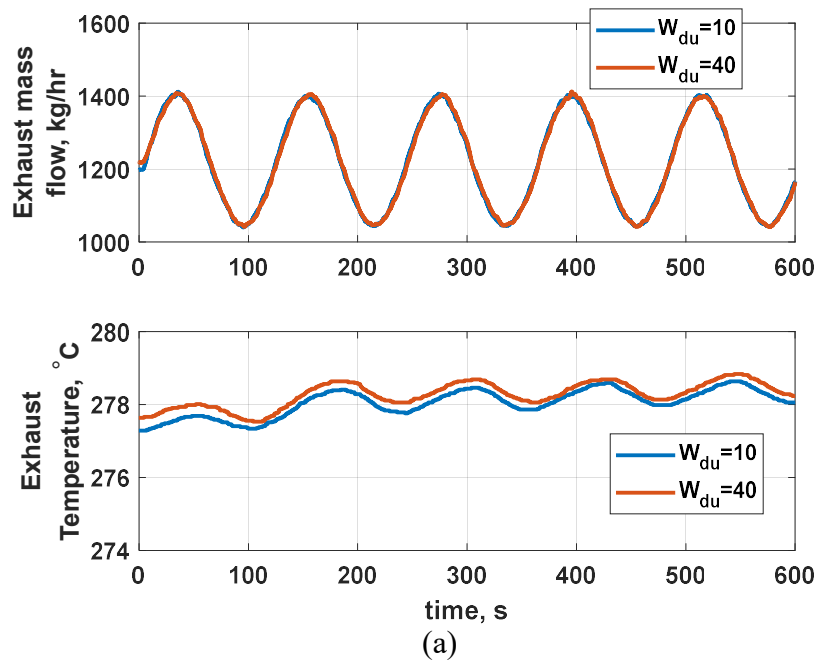


Figure 5. 11. (a) Engine conditions for the sinusoidal cycle with time period of 60s (b) Tuned NMPC superheat tracking performance and generated working fluid flow rate,  $W_{du}=10$

However, the overshoot and undershoot is still maintain within  $\pm 5^\circ\text{C}$  which is quite remarkable of the controller. The maximum absolute superheat tracking error was found to be  $4.3^\circ\text{C}$  and mean error was  $1.66^\circ\text{C}$ .

### 5.7.3 Time period of 120 s

Similar to 20s and 60s time period, 120s time period heat signal was also tested with same amplitude of 100 rpm and 400 Nm. As expected with increase in time period, oscillation increased. Note that same weights of  $W_{du}=10$  were used initially resulting in a maximum absolute superheat tracking error of  $5.23^\circ\text{C}$  and mean error of  $13.06^\circ\text{C}$ . It was only with a larger weight that the oscillations were brought back within the  $\pm 5^\circ\text{C}$  range as seen from the Figure 5.12 (b).



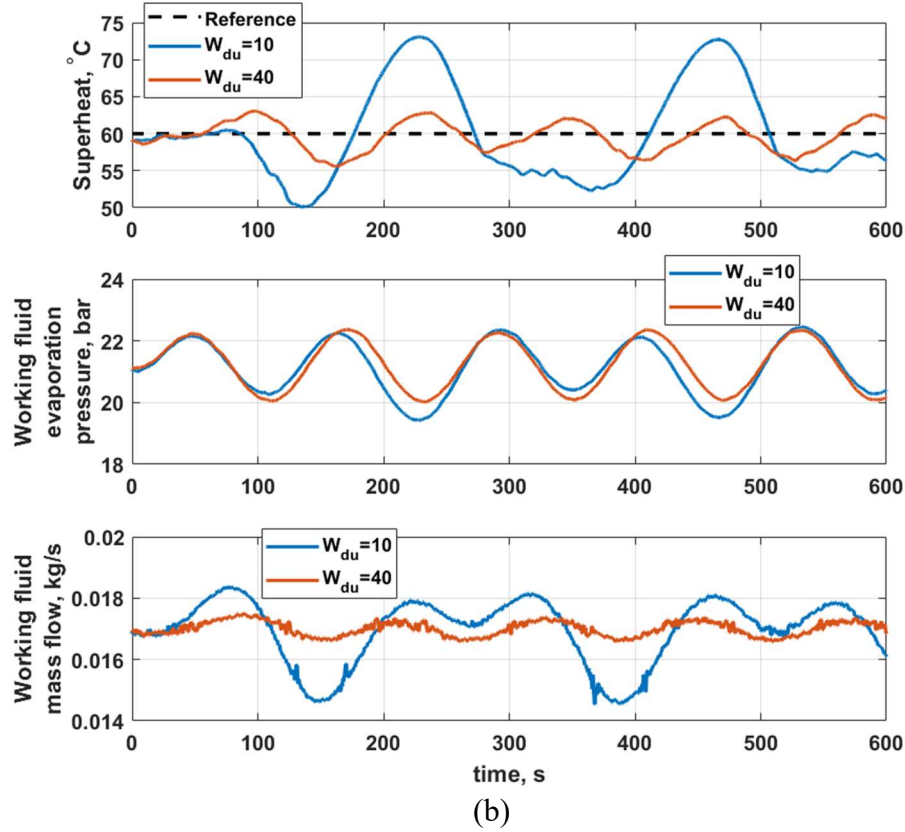


Figure 5. 12. (a) Engine conditions for the sinusoidal cycle with time period of 120s (b) Tuned NMPC superheat tracking performance comparison with weights,  $W_{du}=10$  and  $W_{du}=60$  with generated working fluid flow rate

At slower frequency of heat source, there is plenty of time available for heat transfer and the corresponding changes can be seen at the working fluid evaporator outlet temperature. Comparing the three time periods, it can be concluded that 120s is the worst case. In such situations a slower working fluid flow produces better tracking performance as shown in the Figure 5.12 (b). In Chapter 1, it was experimentally shown that the temperature dynamics is slower than the working fluid mass flow change. This is because the heat transfer process is slow as the exhaust gas first heats up the tube walls before transferring the energy to the working fluid. It is because of this process that the rate of change of working fluid had be slowed down to match the temperature

dynamics time constant. A direct realization of this approach can be seen in Figure 5.12 (b), where the slower working fluid flow generated less oscillations.

Table 5.1 summarizes the results of the sinusoidal study. Even in this study, the mean computation time was found to be 0.0871s. This boost confidence in real time NMPC implementation.

Time period, s	Weight, $W_{du}$	Mean Error, °C	Max Error, °C	NMPC Computation time, s
20	20	0.95	1.88	0.0871
60	20	1.75	3.74	0.0871
120	10	5.23	13.06	0.0871
	40	1.74	4.44	0.0871

*Table 5. 1. NMPC superheat tracking error for different time period sinusoidal heat signal.*

## 5.8 Conclusions

In this Chapter, an experimental investigation was conducted to evaluate the NMPC controller performance under different engine conditions. During the initial experimental implementation, there was a performance shift observed due to system aging. This caused the EKF to estimate faulty state values and therefore the control oriented model had to be tuned online to match the new heat transfer efficiency of the aged ORC system.

Once the state estimation outputs were stabilized, ramp inputs in heat source with rise times of 30s and 5s were introduced as disturbance. NMPC was then tuned to this ramp inputs to maintain the superheat tracking within  $\pm 5$  °C range. With the tuned NMPC weights, a heavy transient drive cycle with near constant engine speed and fast varying load was run. The mean superheat tracking error was found to be 2.9 °C for the drive cycle. Although the drive cycle was transient in nature, and the superheat tracking was exceptional, but the working fluid flow rate didn't fluctuated

according to the heat. In fact the working fluid flow steadily increased with the rise of exhaust gas temperature at the evaporator inlet.

To further investigate the dampened response of the evaporator a sinusoidal heat signals with varying time periods were generated. As expected high frequency (time period =20s) heat signals caused no changed to the control input and superheat tracking error. As the time period of the heat signal was increased, subsequently more time was available for heat transfer and hence more oscillatory behavior was observed, both for the working fluid temperature and for the working fluid flow. It was also showed that as the heat signal time period is increased, to reduce the corresponding oscillations in superheat, a higher penalty to the rate of change of working fluid flow is needed to maintain the tracking performance within  $\pm 5^{\circ}\text{C}$ .

## Chapter 6. Conclusion, Contributions and Future Work

This Chapter provides concise highlights of the outcome of preceding Chapters. This section also explains the limitations and future work of this study. Finally, the original contributions of the presented research work and its impact are accentuated.

### 6.1 Conclusions and Contributions

This thesis contributes towards development of an NMPC controller for WHR-ORC system in an HHDE application with enhanced capabilities under highly transient conditions. The main contribution is the development of the NMPC control strategy with preview capability, followed by characterization of its benefits. To this end, 1) an enhanced evaporator model is developed for accurate estimation of changing phase lengths inside the evaporator and 2) an augmented EKF with disturbance rejection is proposed.

**Enhanced evaporator modeling and proposed improvement of the mixed-phase heat transfer coefficients.** First, discretization of the FVM showed that increased discretization increases the model's phase length prediction capability. However, the working fluid temperature at the evaporator outlet doesn't necessarily benefit by increasing the discretization. It was found that while 10 cells are enough to accurately model the evaporator outlet temperatures, but a 500 cell discretization provided the best phase length prediction capability. Second, additional multipliers are introduced to the existing empirical equations to improve the phase length estimation accuracy. This additional multipliers were identified using Particle Swarm Optimization (PSO) technique against thermal imagery data. The newly identified multipliers for the empirical equations were validated against transient experimental data and showed 43% improvement in vapor phase length prediction in comparison to the baseline FVM.

The identification set was limited to the available thermal data, and is valid within the identification range. However, this study serves as a proof-of-concept methodology exhibiting that the phase length estimation can be improved by using thermal imaging data. The methodology developed herein can provide additional insight to the evaporator design process and serve as basis for improving moving boundary models for advanced ORC system control development.

**NMPC Controller design.** For a WHR-ORC system in an automotive application the highly dynamic nature of the heat sources provide a significant control challenge. Moreover, the non-linear behavior of the evaporator dynamics changes with the engine operating conditions and possess additional control challenges. In order to address these challenges a NMPC controller was designed. **First, an augmented disturbance rejection estimator** in an EKF framework was designed to reject modeling errors and measurement inaccuracies, thus improving steady state performance. Simulation study demonstrated the elimination of steady state error after the implementation of disturbance rejection in EKF. Further, it was shown that the augmented estimator also helps reject measurement inaccuracies.

**Second,** during the initial formulation of objective function for NMPC controller it was found that the best way to optimize for turbine power without violating any constraints was to track the superheat. Then, the superheat tracking performance was compared between *NMPC with preview capability* and NMPC without this feature for a drive cycle. It was found that knowing the future helps improve the control effort and therefore improved robustness. However, it doesn't provide any significant improvement to the superheat tracking performance for the drive cycle. Additionally, this comparison study was extended to sinusoidal heat signals with varying time periods of 4s to 240s. This case study showed that the minimum superheat that could be tracked without using the preview feature was 20 °C. NMPC with preview capability helped the controller



in maintaining a tight tolerance. It was found that the minimum superheat that could be tracked with preview feature was 15 °C. Thus providing higher turbine power in comparison to the NMPC without the preview feature.

**Third, *experimental validation*** of the designed NMPC controller without preview feature was conducted. During online implementation it was concluded that the control oriented model of the evaporator was susceptible to system aging and had to be re-calibrated online to compute stable state estimates for MPC.

Then the weights of the NMPC were tuned to the ramp inputs of heat source such that the superheat tracking was within  $\pm 5$  °C. The performance of the tuned NMPC was then evaluated for a drive cycle and the mean superheat tracking error was found to be 2.9 °C. The required working fluid for this heavy transient drive cycle didn't varied dynamically in cohesion with the heat source and therefore with preview capability of the NMPC was not tested online since the only advantage of with preview capability was reduction in control effort. Therefore, to further investigate the evaporator dynamics sinusoidal heat source was generated and validated experimentally. In this study, highly dynamic heat source with time period of 20s and 60s didn't affect the performance of the controller as the thermal inertia of the evaporator helped buffer out the high frequency components of the heat source. However, when the time period of the exhaust conditions was increased to 120s, the evaporator outlet temperature dynamically varied with the heat source and a maximum overshoot of 13.5 °C was observed. In this particular instance, it was found that a heavier penalty to the rate of change of control input aided to bring the superheat overshoot within  $\pm 5$  °C limit. Thus, it was recommended that a high penalty on working fluid change rate should be utilized to maintain superheat tracking performance within acceptable limits.

## 6.2 Future Work

The conclusion and developments presented in this thesis leads to further exploration in areas of both modeling and control improvement.

**Extending the enhanced evaporator model identification and validation.** A high fidelity FVM evaporator model was expanded to enhance the working fluid phase length predictions during transient operation in this thesis. However, due to limited availability of the thermal data the identification of the additional multipliers were valid within a given range of operation. In future studies a more systematic design of experiments will be conducted to cover the entire range of the ORC-WHR operation. Both identification and validation data sets will be expanded to represent the complete operating range of the engine and the author hopes to developed a correlation of the proposed multipliers that would be a function of the exhaust heat power.

**Control strategy improvement.** In this study, a disturbance augmented, look-ahead NMPC strategy is proposed for superheat control of a single evaporator WHR-ORC system. In future works, this study will be extended to ORC system with two evaporators and further investigate the effectiveness of both the disturbance rejection and the preview capability. Due to time constraint, the control strategy was only implemented on a TP evaporator. It would be interesting to exploit the benefits of the NMPC's preview capability on EGR evaporator which has less thermal inertia. It was shown in Chapter 3 that the dynamics of the EGR evaporator is faster compare to TP evaporator. Therefore, the reduce control effort with preview capability would be beneficial to EGR evaporator since it will fail to buffer the high frequency components of the exhaust.

Moreover, the current experimental validation showed that system aging affects the performance of the model based approach. For future testing, it is planned to characterize this

behavior at regular run time hours and generate deeper understanding required to accurately model this type of aging.

## APPENDIX

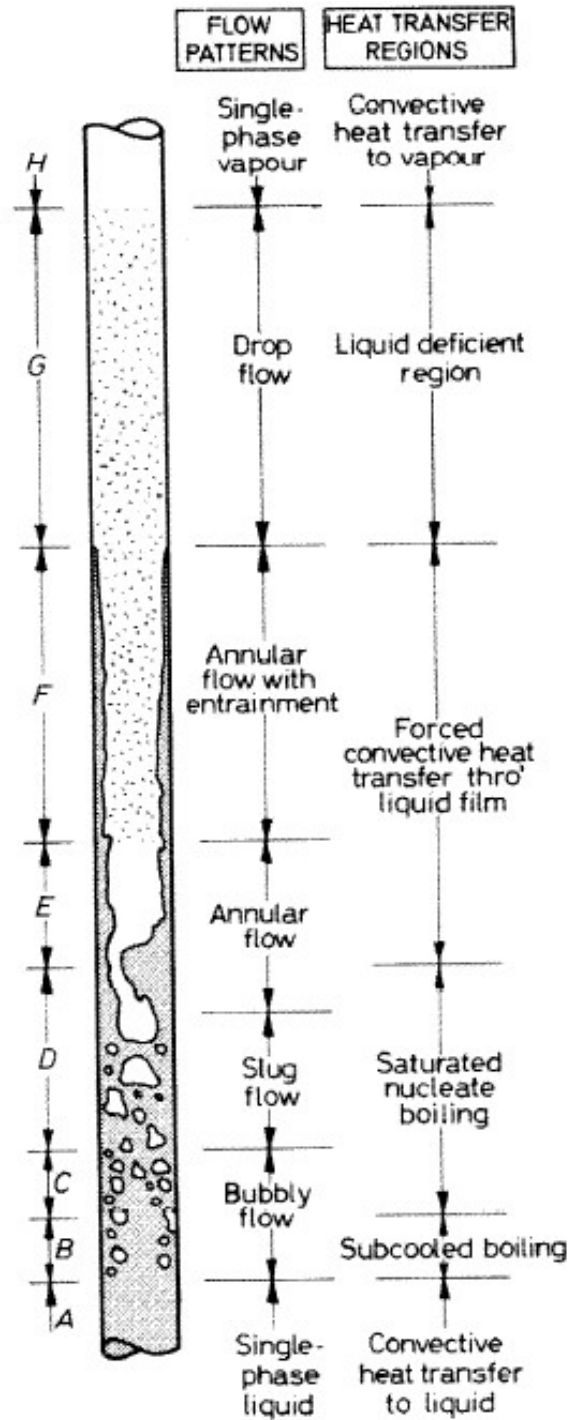


Figure a. Heat Transfer and Flow Regimes in a vertical tube [33].

## REFERENCES

1. Schoettle, Brandon, Michael Sivak, and Michael Tunnell. "A survey of fuel economy and fuel usage by heavyduty truck fleets." *No. SWT-2016-12, [http://atri-online.org/wpcontent/uploads/2016/10/2016\\_ATRI-UMTRI\\_FuelEconomyReport\\_Final\\_.pdf](http://atri-online.org/wpcontent/uploads/2016/10/2016_ATRI-UMTRI_FuelEconomyReport_Final_.pdf)* (2016).
2. UPDATE, POLICY. "UNITED STATES EFFICIENCY AND GREENHOUSE GAS EMISSION REGULATIONS FOR MODEL YEAR 2018-2027 HEAVY-DUTY VEHICLES, ENGINES, AND TRAILERS." *Policy* (2015).
3. D. Oeberlein, "Cummins SuperTruck Program Technology and System Level Demonstation of Highly Efficient and Clean, Diesel Powered Class 8 Trucks," *presenttition at US Department of Energy Merit Review*, 2013.
4. M. Allain, D. Atherton, I. Gruden, S. Singh, and K. Sisken, "Daimler's Super Truck Program; 50% Brake Thermal Efficiency," in *presentation at US DOE Directions in Engine-Efficiency and Emissions Research (DEER) Conference*, 2012.
5. V. Grelet, T. Reiche, L. Guillaume, and V. Lemort, "Optimal waste heat recovery Rankine based for heavy duty applications," 2014
6. Chen, Haoxiang, Weilin Zhuge, Yangjun Zhang, Tao Chen, and Lei Zhang. "Performance Simulation of an Integrated Organic Rankine Cycle and Air Inter-Cooling System for Heavy-Duty Diesel Truck Engines." In *ASME Turbo Expo 2017: Turbomachinery Technical Conference and Exposition*, pp. V003T28A004-V003T28A004. American Society of Mechanical Engineers, 2017.

7. Teng, Ho, Gerhard Regner, and Chris Cowland. *Achieving high engine efficiency for heavy-duty diesel engines by waste heat recovery using supercritical organic-fluid Rankine cycle*. No. 2006-01-3522. SAE Technical Paper, 2006.
8. Legros Arnaud, Guillaume Ludovic, Diny Mouad, Zaïdi Hamid and Lemort Vincent. *Comparison and Impact of Waste Heat Recovery Technologies on Passenger Car Fuel Consumption in a Normalized Driving Cycle*. *Energies* ISSN 1996-1073
9. F. Yang, X. Dong, H. Zhang, Z. Wang, K. Yang, J. Zhang, et al., "Performance analysis of waste heat recovery with a dual loop organic Rankine cycle (ORC) system for diesel engine under various operating conditions," *Energy Conversion and Management*, vol. 80, pp. 243-255, 2014.
10. G. Shu, G. Yu, H. Tian, H. Wei, X. Liang, and Z. Huang, "Multi-approach evaluations of a cascade-Organic Rankine Cycle (C-ORC) system driven by diesel engine waste heat: Part A—Thermodynamic evaluations," *Energy Conversion and Management*, vol. 108, pp. 579-595, 2016.
11. I. Arsie, A. Cricchio, C. Pianese, M. D. Cesare, and W. Nesci, "A Comprehensive Powertrain Model to Evaluate the Benefits of Electric Turbo Compound (ETC) in Reducing CO2 Emissions from Small Diesel Passenger Cars," SAE Technical Paper 2014-01-1650, 2014, DOI: 10.4271/ 2014-01-1650.
12. C. Zhang, G.-Q. Shu, H. Tian, H. Wei, G. Yu, and Y. Liang, "Theoretical Analysis of a Combined Thermoelectric Generator (TEG) and Dual-loop Organic Rankine Cycle (DORC) System Using for Engines' Exhaust Waste Heat Recovery," SAE Technical Paper 2014-01-0670, 2014, DOI: 10.4271/ 2014-01-0670.

13. Davidson, Thomas A. "Design and analysis of a 1 kw Rankine power cycle, employing a multi-vane expander, for use with a low temperature solar collector." PhD diss., Massachusetts Institute of Technology, 1977.
14. Monahan, J. and McKenna, R., 1976, September. Development of a 1-kW, organic Rankine cycle power plant for remote applications. In *Proceedings of the Intersociety Energy Conversion Engineering Conference, New York, NY, USA*(Vol. 1217).
15. Probert, S. D., Mohey Hussein, P. W. O'Callaghan, and Eli Bala. "Design optimisation of a solar-energy harnessing system for stimulating an irrigation pump." *Applied Energy* 15, no. 4 (1983): 299-321.
16. Arias, Diego A., Timothy A. Shedd, and Ryan K. Jester. *Theoretical analysis of waste heat recovery from an internal combustion engine in a hybrid vehicle*. No. 2006-01-1605. SAE Technical Paper, 2006.
17. Hernandez, Andres, Adriano Desideri, Clara Ionescu, Sylvain Quoilin, Vincent Lemort, and Robin De Keyser. "Experimental study of Predictive Control strategies for optimal operation of Organic Rankine Cycle systems." In *2015 European Control Conference (ECC)*, pp. 2254-2259. IEEE, 2015.
18. Grelet, Vincent, Pascal Dufour, Madiha Nadri, Thomas Reiche, and Vincent Lemort. "Modeling and control of Rankine based waste heat recovery systems for heavy duty trucks." *IFAC-PapersOnLine* 48, no. 8 (2015): 568-573.
19. Feru, Emanuel, Frank Willems, Bram de Jager, and Maarten Steinbuch. "Model predictive control of a waste heat recovery system for automotive diesel engines." In *System Theory, Control and Computing (ICSTCC), 2014 18th International Conference*, pp. 658-663. IEEE, 2014.

20. Esposito, Marco Crialesi, Nicola Pompini, Agostino Gambarotta, Vetrivel Chandrasekaran, Junqiang Zhou, and Marcello Canova. "Nonlinear model predictive control of an organic rankine cycle for exhaust waste heat recovery in automotive engines." *IFAC-PapersOnLine* 48, no. 15 (2015): 411-418.
21. Hou, Guolian, Rui Sun, Guoqiang Hu, and Jianhua Zhang. "Supervisory predictive control of evaporator in Organic Rankine Cycle (ORC) system for waste heat recovery." In *Advanced Mechatronic Systems (ICAMechS), 2011 International Conference on*, pp. 306-311. IEEE, 2011.
22. Hernandez Naranjo, Jairo Andres, Adriano Desideri, Clara-Mihaela Ionescu, Sylvain Quoilin, Vincent Lemort, and Robain De Keyser. "Increasing the efficiency of organic rankine cycle technology by means of multivariable predictive control." In *19th World Congress of the International-Federation-of-Automatic-Control (IFAC)*, vol. 47, no. 3, pp. 2195-2200. 2014.
23. Liu, Xiaobing, Adamu Yebi, Paul Anschel, John Shutty, Bin Xu, Mark Hoffman, and Simona Onori. "Model predictive control of an organic Rankine cycle system." *Energy Procedia* 129 (2017): 184-191.
24. Feru, Emanuel, Bram de Jager, Frank Willems, and Maarten Steinbuch. "Two-phase plate-fin heat exchanger modeling for waste heat recovery systems in diesel engines." *Applied energy* 133 (2014): 183-196.
25. Quoilin, Sylvain, Richard Aumann, Andreas Grill, Andreas Schuster, Vincent Lemort, and Hartmut Spliethoff. "Dynamic modeling and optimal control strategy of waste heat recovery Organic Rankine Cycles." *Applied energy* 88, no. 6 (2011): 2183-2190.



26. J. M. Jensen, "Dynamic Modeling of Thermo-Fluid Systems with Focus on Evaporators for Refrigeration," PhD, Department of Mechanical Engineering, Technical University of Denmark, 2003.
27. Benato, A., Martin Ryhl Kærn, Leonardo Pierobon, A. Stoppato, and Fredrik Haglind. "Analysis of hot spots in boilers of organic Rankine cycle units during transient operation." *Applied Energy* 151 (2015): 119-131.
28. Yebi, Adamu, Bin Xu, Xiaobing Liu, John Shutty, Paul Anschel, Simona Onori, Zoran Filipi, and Mark Hoffman. "Nonlinear model predictive control strategies for a parallel evaporator diesel engine waste heat recovery system." In *ASME 2016 Dynamic Systems and Control Conference*, pp. V002T19A003-V002T19A003. American Society of Mechanical Engineers, 2016.
29. Peralez, Johan, Paolino Tona, Antonio Sciarretta, Pascal Dufour, and Madiha Nadri. "Towards model-based control of a steam rankine process for engine waste heat recovery." In *Vehicle Power and Propulsion Conference (VPPC), 2012 IEEE*, pp. 289-294. IEEE, 2012.
30. Zhang, Jianhua, Song Gao, Yannan Chen, and Guolian Hou. "Multivariable robust control for organic rankine cycle based waste heat recovery systems." In *Industrial Electronics and Applications (ICIEA), 2013 8th IEEE Conference on*, pp. 85-89. IEEE, 2013.
31. Zhang, H. G., E. H. Wang, and B. Y. Fan. "Heat transfer analysis of a finned-tube evaporator for engine exhaust heat recovery." *Energy Conversion and Management* 65 (2013): 438-447.
32. Xu, Bin, Dhruvang Rathod, Shreyas Kulkarni, Adamu Yebi, Zoran Filipi, Simona Onori, and Mark Hoffman. "Transient dynamic modeling and validation of an organic Rankine cycle waste heat recovery system for heavy duty diesel engine applications." *Applied Energy* 205 (2017): 260-279

33. VDI Heat Atlas, DOI 10.1007/978-3-540-77877-6\_23, © Springer-Verlag Berlin Heidelberg 2010
34. Xu, Bin, Xiaobing Liu, John Shuttty, Paul Anschel, Simona Onori, Zoran Filipi, and Mark Hoffman. *Physics-based modeling and transient validation of an organic Rankine cycle waste heat recovery system for a heavy-duty diesel engine*. No. 2016-01-0199. SAE Technical Paper, 2016.
35. Collier, John G., and John R. Thome. *Convective boiling and condensation*. Clarendon Press, 1994.
36. Jiménez-Arreola, Manuel, Roberto Pili, Christoph Wieland, and Alessandro Romagnoli. "Analysis and comparison of dynamic behavior of heat exchangers for direct evaporation in ORC waste heat recovery applications from fluctuating sources." *Applied Energy* 216 (2018): 724-740.
37. Bemporad, Alberto. "Model predictive control design: New trends and tools." In *Decision and Control, 2006 45th IEEE Conference on*, pp. 6678-6683. IEEE, 2006.
38. Ganji, Behnam, and Abbas Z. Kouzani. "A study on look-ahead control and energy management strategies in hybrid electric vehicles." In *Control and Automation (ICCA), 2010 8th IEEE International Conference on*, pp. 388-392. IEEE, 2010.
39. Gong, Qiuming, Yaoyu Li, and Zhong-Ren Peng. "Trip-based optimal power management of plug-in hybrid electric vehicles." *IEEE Transactions on vehicular technology* 57, no. 6 (2008): 3393-3401.
40. Rajagopalan, Arun, and Gregory Washington. *Intelligent control of hybrid electric vehicles using GPS information*. No. 2002-01-1936. SAE Technical Paper, 2002.

41. Boehme, Thomas Juergen, Florian Held, Christoph Rollinger, Heiko Rabba, Matthias Schultalbers, and Bernhard Lampe. "Application of an optimal control problem to a trip-based energy management for electric vehicles." *SAE International Journal of Alternative Powertrains* 2, no. 1 (2013): 115-126.
42. Smith, R., M. Morison, D. Capelle, C. Christie, and D. Blair. "GPS-based optimization of plug-in hybrid electric vehicles' power demands in a cold weather city." *Transportation Research Part D: Transport and Environment* 16, no. 8 (2011): 614-618.
43. Huang, Wei, and David M. Bevly. "Set terrain-based optimal speed limits for heavy trucks energy saving." *International Journal of Powertrains* 1, no. 4 (2012): 335-350.
44. Turri, Valerio, Bart Besselink, Jonas Mårtensson, and Karl H. Johansson. "Fuel-efficient heavy-duty vehicle platooning by look-ahead control." In *Decision and Control (CDC), 2014 IEEE 53rd Annual Conference on*, pp. 654-660. IEEE, 2014.
45. Gáspár, Péter, and Balázs Németh. "Design of look-ahead control for road vehicles using traffic information." In *Control and Automation (MED), 2014 22nd Mediterranean Conference of*, pp. 201-206. IEEE, 2014.
46. Jazwinski, A. H. "Stochastic Process and Filtering Theory, Academic Press." *A subsidiary of Harcourt Brace Jovanovich Publishers* (1970).
47. Maeder, Urban, and Manfred Morari. "Offset-free reference tracking for predictive controllers." In *Decision and Control, 2007 46th IEEE Conference on*, pp. 5252-5257. IEEE, 2007.
48. Borrelli, Francesco, and Manfred Morari. "Offset free model predictive control." In *Decision and Control, 2007 46th IEEE Conference on*, pp. 1245-1250. IEEE, 2007.

49. J. M. Jensen. "Dynamic Modeling of Thermo-Fluid Systems with Focus on Evaporators for Refrigeration," *Energy Engineering, Department of Mechanical Engineering*, Technical University of Denmark, 2003.
50. Houska, Boris, Hans Joachim Ferreau, and Moritz Diehl. "ACADO toolkit—An open-source framework for automatic control and dynamic optimization." *Optimal Control Applications and Methods* 32, no. 3 (2011): 298-312.
51. Quirynen, Rien, Sébastien Gros, and Moritz Diehl. "Efficient NMPC for nonlinear models with linear subsystems." In *52nd IEEE Conference on Decision and Control*, pp. 5101-5106. IEEE, 2013.
52. Gros, Sébastien, Mario Zanon, Rien Quirynen, Alberto Bemporad, and Moritz Diehl. "From linear to nonlinear MPC: bridging the gap via the real-time iteration." *International Journal of Control* (2016): 1-19.
53. Maeder, Urban, and Manfred Morari. "Offset-free reference tracking for predictive controllers." In *Decision and Control, 2007 46th IEEE Conference on*, pp. 5252-5257. IEEE, 2007.
54. Borrelli, Francesco, and Manfred Morari. "Offset free model predictive control." In *Decision and Control, 2007 46th IEEE Conference on*, pp. 1245-1250. IEEE, 2007.
55. Bemporad, Alberto. "Model predictive control design: New trends and tools." In *Decision and Control, 2006 45th IEEE Conference on*, pp. 6678-6683. IEEE, 2006.
56. Zedan, H. "An AN-stable Rosenbrock-type method for solving stiff differential equations." *Computers & Mathematics with Applications* 13, no. 7 (1987): 611-615.

57. Peralez, Johan, Madiha Nadri, Pascal Dufour, Paolino Tona, and Antonio Sciarretta. "Organic Rankine cycle for vehicles: Control design and experimental results." *IEEE Transactions on Control Systems Technology* 25, no. 3 (2017): 952-965.
58. Hernandez, Andres, Adriano Desideri, Sergei Gusev, Clara M. Ionescu, Martijn Van Den Broek, Sylvain Quoilin, Vincent Lemort, and Robin De Keyser. "Design and experimental validation of an adaptive control law to maximize the power generation of a small-scale waste heat recovery system." *Applied energy* 203 (2017): 549-559.
59. Seitz, D., O. Gehring, C. Bunz, M. Brunschier, and O. Sawodny. "Model-based control of exhaust heat recovery in a heavy-duty vehicle." *Control Engineering Practice* 70 (2018): 15-28.

## PUBLICATIONS

60. Rathod, Dhruvang, Ujjwal Belwariar, Bin Xu, and Mark Hoffman. "An enhanced evaporator model for working fluid phase length prediction, validated with experimental thermal imaging data." *International Journal of Heat and Mass Transfer* 132 (2019): 194-208.
61. Rathod, Dhruvang, Bin Xu, Adamu Yebi, Ardalan Vahidi, Zoran Filipi, and Mark Hoffman. *A Look-ahead Model Predictive Control Strategy for an Organic Rankine Cycle-Waste Heat Recovery System in a Heavy Duty Diesel Engine Application*. No. 2019-01-1130. SAE Technical Paper, 2019.
62. Xu, Bin, Dhruvang Rathod, Adamu Yebi, Zoran Filipi, Simona Onori, and Mark Hoffman. "A comprehensive review of organic rankine cycle waste heat recovery systems in heavy-duty diesel engine applications." *Renewable and Sustainable Energy Reviews* 107 (2019): 145-170.

63. Xu, Bin, Dhruvang Rathod, Shreyas Kulkarni, Adamu Yebi, Zoran Filipi, Simona Onori, and Mark Hoffman. "Transient dynamic modeling and validation of an organic Rankine cycle waste heat recovery system for heavy duty diesel engine applications." *Applied Energy* 205 (2017): 260-279.
64. Xu, Bin, Dhruvang Rathod, Adamu Yebi, Zoran Filipi, Simona Onori, and Mark Hoffman. "A comprehensive review of organic rankine cycle waste heat recovery systems in heavy-duty diesel engine applications." *Renewable and Sustainable Energy Reviews* 107 (2019): 145-170.
65. Rathod, Dhruvang, Simona Onori, Zoran Filipi, and Mark Hoffman. "Experimental Investigation of Soot Accumulation and Regeneration in a Catalyzed Gasoline Particulate Filter Utilizing Particulate Quantification and Gas Speciation Measurements." In *ASME 2018 Internal Combustion Engine Division Fall Technical Conference*, pp. V002T04A002-V002T04A002. American Society of Mechanical Engineers, 2018.
66. Rathod, Dhruvang, Mark A. Hoffman, and Simona Onori. "Determining three-way catalyst age using differential lambda signal response." *SAE International Journal of Engines* 10, no. 3 (2017): 1305-1312.